Search for Low Energetic Neutrino Signals from Galactic Supernovae and Collisionally Heated Gamma-Ray Bursts with the IceCube Neutrino Observatory



Dissertation zur Erlangung des Grades "Doktor der Naturwissenschaften"

am Fachbereich für Physik, Mathematik und Informatik der Johannes Gutenberg-Universität Mainz

> von Volker Baum geboren am 14.12.1986 in Bonn

> > Mainz, den 31. Mai 2017

Search for Low Energetic Neutrino Signals from Galactic Supernovae and Collisionally Heated Gamma-Ray Bursts with the IceCube Neutrino Observatory

1. Gutachter: - aus datenschutzrechtlichen Gründen entfernt -

2. Gutachter: - aus datenschutzrechtlichen Gründen entfernt -

Datum der mündlichen Prüfung: 23. November 2017

Volker Baum ETAP/IceCube Institut für Physik Staudingerweg 7 Johannes Gutenberg-Universität D-55099 Mainz

Abstract

The IceCube Neutrino Observatory, located in the glacial ice beneath the geographic South Pole, surveys a one cubic kilometer volume in the Antarctic ice for particle interactions. This detector volume is monitored by 5160 digital optical modules, each equipped with a photo-multiplier tube as sensor. Within the last years, most studies with the IceCube detector were focused on searches for high-energy neutrinos that do not arise from cosmic ray interactions in the atmosphere. These efforts eventually lead to the detection of an astrophysical neutrino flux manifesting in events with energies at the 1 - 10 PeV energy range. This work, in contrast, focuses on the low-energy regime below 1 TeV. Therefore, not only events recorded by the IceCube detector are investigated, but also those detected by its low-energy extension DeepCore that has a minimal energy threshold of 10 GeV.

The sources in this low-energy regime that will be investigated within this work are *Supernovae* (*SNe*) and *Gamma-Ray Bursts* (*GRBs*). Supernovae emit neutrinos with energies of O(MeV) and are detectable with IceCube by statistical methods within our Galaxy and the Magellanic Clouds. With the improvements presented in this work, the detection probability of SNe in the Magellanic Clouds was increased by a factor of six. Major aspect of the introduced improvements is an efficient realtime correction for the dominating background of atmospheric muons. GRBs are predicted to produce neutrinos of 10 - 100 GeV via the newly proposed inelastic collision mechanism. Of particular interest for this work is a source class that may constitute a possible connection between supernovae and GRBs, the so-called GRB-SN class. In this context, new upper limits were set on the neutrino flux from galactic supernovae with the particular progenitor type required for GRB-SNe as well as on the neutrino flux expected from GRBs described by the inelastic collision model. Finally, a search for coincidences between high-significant SN candidates and events that are on-time with GRBs will be presented.

CONTENTS

1	Intro	oductio	'n	1		
2	Neu	trinos,	Cosmic Ray Backgrounds and the Cherenkov Effect	3		
	2.1	The St	andard Model of Particle Physics	. 3		
	2.2	Neutri	no Interactions	. 5		
		2.2.1	The MeV-Regime	. 5		
		2.2.2	The GeV-Regime	. 6		
	2.3	Neutri	no Oscillations and the Neutrino Mass Hierarchy	. 7		
	2.4	Cosmi	c Rays and Atmospheric Backgrounds	. 11		
	2.5	The C	herenkov Effect	. 13		
3	Astı	ophysi	ical Sources of Low Energetic Neutrinos	15		
	3.1	Gamm	na-Ray Bursts	. 15		
		3.1.1	Classification and Central Engines	. 16		
		3.1.2	Particle Acceleration: Standard Paradigm vs. Photospheric Models	. 17		
		3.1.3	Current Satellite Measurements and GRBWeb	. 21		
	3.2	Superi	novae	. 23		
		3.2.1	Thermonuclear Supernovae	. 24		
		3.2.2	Core Collapse Supernovae	. 25		
4	Neu	trino D	etection with the IceCube Neutrino Telescope	33		
	4.1	IceCul	be/DeepCore	. 34		
	4.2	Digita	l Optical Modules	. 35		
		4.2.1	Photomultiplier Tubes	. 36		
		4.2.2	Digitization	. 37		
	4.3	Data A	Acquisition and Processing	. 38		
		4.3.1	Trigger System	. 39		
		4.3.2	Filter and Hit Cleaning	. 40		
		4.3.3	Transfer to the North	. 42		
	4.4	The A	ntarctic Ice	. 42		
	4.5					
		4.5.1	Event-like Signatures: Tracks and Cascades	. 43		
		4.5.2	Supernova Signatures: Collective Increase in the Dark Noise Rate	. 45		
		4.5.3	Noise Signatures	. 45		
	4.6	PING	U - A Possible Low-Energy Future of IceCube	. 46		

5	Sim	ulation and Reconstruction	49
	5.1	Simulation	49
		5.1.1 Event-based Simulation	49
		5.1.2 SN Simulation	51
	5.2	Reconstruction	54
		5.2.1 LineFit/ImprovedLineFit	54
		5.2.2 SPE/ImprovedSPE/MPE	55
		5.2.3 FiniteReco	56
		5.2.4 Monopod/Millipede	56
		5.2.5 The Resca Resolution Estimator	57
6	Sea	rch for Galactic GRB-SNe with the Supernova Data Acquisition System	59
	6.1	The South Pole System	59
	6.2	System Stability, Testing and Maintenance	60
	6.3	Significance Calculation	62
	6.4	Alert Handling	64
	6.5	Implementation of an Efficient, Robust and Realtime Atmospheric Muon	
		Subtraction	67
		6.5.1 The Subtraction Method	68
		6.5.2 Muon Corrected Significance Thresholds	69
		6.5.3 Performance of the Atmospheric Muon Subtraction	71
	6.6	Upper Limits for Black Hole Forming SNe Detection	73
		6.6.1 Systematic Effects	74
			/4
7	Sea		/4
7		rch for Low-Energetic Neutrinos from Collisionally Heated Gamma	74 77
7		rch for Low-Energetic Neutrinos from Collisionally Heated Gamma Bursts	
7	Ray	rch for Low-Energetic Neutrinos from Collisionally Heated Gamma Bursts Experimental and Simulated Datasets	77
7	Ray 7.1	rch for Low-Energetic Neutrinos from Collisionally Heated Gamma Bursts Experimental and Simulated Datasets	77 78
7	Ray 7.1	rch for Low-Energetic Neutrinos from Collisionally Heated Gamma Bursts Experimental and Simulated Datasets Initial Event Selection 7.2.1	77 78 81
7	Ray 7.1	rch for Low-Energetic Neutrinos from Collisionally Heated Gamma Bursts Experimental and Simulated Datasets Initial Event Selection 7.2.1 LowE-Level3 7.2.2 Level4	77 78 81 82
7	Ray 7.1	rch for Low-Energetic Neutrinos from Collisionally Heated Gamma Bursts Experimental and Simulated Datasets Initial Event Selection 7.2.1 LowE-Level3 7.2.2 Level4 7.2.3 Level5	77 78 81 82 84
7	Ray 7.1	rch for Low-Energetic Neutrinos from Collisionally Heated Gamma Bursts Experimental and Simulated Datasets Initial Event Selection 7.2.1 LowE-Level3 7.2.2 Level4 7.2.3 Level5 7.2.4 Level6 - Boosted Decision Trees	77 78 81 82 84 85
7	Ray 7.1	rch for Low-Energetic Neutrinos from Collisionally Heated Gamma BurstsExperimental and Simulated DatasetsInitial Event Selection7.2.1LowE-Level37.2.2Level47.2.3Level57.2.4Level6 - Boosted Decision Trees7.2.5Rate Summary	77 78 81 82 84 85 88
7	Ray 7.1 7.2	rch for Low-Energetic Neutrinos from Collisionally Heated Gamma BurstsExperimental and Simulated DatasetsInitial Event Selection7.2.1LowE-Level37.2.2Level47.2.3Level57.2.4Level6 - Boosted Decision Trees7.2.5Rate SummaryLikelihood Analysis and Final Event Selection	77 78 81 82 84 85 88 96
7	Ray 7.1 7.2	rch for Low-Energetic Neutrinos from Collisionally Heated Gamma BurstsExperimental and Simulated DatasetsInitial Event Selection7.2.1LowE-Level37.2.2Level47.2.3Level57.2.4Level6 - Boosted Decision Trees7.2.5Rate SummaryLikelihood Analysis and Final Event Selection7.3.1Likelihood Method and Test Statistics	77 78 81 82 84 85 88 96 97
7	Ray 7.1 7.2	rch for Low-Energetic Neutrinos from Collisionally Heated Gamma BurstsExperimental and Simulated DatasetsInitial Event Selection7.2.1LowE-Level37.2.2Level47.2.3Level57.2.4Level6 - Boosted Decision Trees7.2.5Rate SummaryLikelihood Analysis and Final Event Selection7.3.1Likelihood Method and Test Statistics7.3.2Probability Distribution Functions	77 78 81 82 84 85 88 96 97 97
7	Ray 7.1 7.2	rch for Low-Energetic Neutrinos from Collisionally Heated Gamma BurstsExperimental and Simulated DatasetsInitial Event Selection7.2.1LowE-Level37.2.2Level47.2.3Level57.2.4Level6 - Boosted Decision Trees7.2.5Rate SummaryLikelihood Analysis and Final Event Selection7.3.1Likelihood Method and Test Statistics7.3.2Probability Distribution Functions	77 78 81 82 84 85 88 96 97 97 98 02
7	Ray 7.1 7.2	rch for Low-Energetic Neutrinos from Collisionally Heated Gamma Bursts Experimental and Simulated Datasets Initial Event Selection 7.2.1 LowE-Level3 7.2.2 Level4 7.2.3 Level5 7.2.4 Level6 - Boosted Decision Trees 7.2.5 Rate Summary Likelihood Analysis and Final Event Selection 7.3.1 Likelihood Method and Test Statistics 7.3.3 Frequentist Evaluation 7.3.4 Level7 - Final Event Selection and Sensitivities	77 78 81 82 84 85 88 96 97 97 98 02 05
7	Ray 7.1 7.2	rch for Low-Energetic Neutrinos from Collisionally Heated Gamma BurstsExperimental and Simulated DatasetsInitial Event Selection7.2.1LowE-Level37.2.2Level47.2.3Level57.2.4Level6 - Boosted Decision Trees7.2.5Rate SummaryLikelihood Analysis and Final Event Selection7.3.1Likelihood Method and Test Statistics7.3.3Frequentist Evaluation17.3.4Level7 - Final Event Selection and Sensitivities1	77 78 81 82 84 85 88 96 97 97 97 98 02 05
7	Ray 7.1 7.2 7.3	rch for Low-Energetic Neutrinos from Collisionally Heated Gamma Bursts Experimental and Simulated Datasets Initial Event Selection 7.2.1 LowE-Level3 7.2.2 Level4 7.2.3 Level5 7.2.4 Level6 - Boosted Decision Trees 7.2.5 Rate Summary Likelihood Analysis and Final Event Selection 7.3.1 Likelihood Method and Test Statistics 7.3.2 Probability Distribution Functions 7.3.3 Frequentist Evaluation 7.3.4 Level7 - Final Event Selection and Sensitivities 7.3.5 Systematic Uncertainties	77 78 81 82 84 85 88 96 97 97 98 02 05 08 10
7	Ray 7.1 7.2 7.3	rch for Low-Energetic Neutrinos from Collisionally Heated Gamma Bursts Experimental and Simulated Datasets Initial Event Selection 7.2.1 LowE-Level3 7.2.2 Level4 7.2.3 Level5 7.2.4 Level6 - Boosted Decision Trees 7.2.5 Rate Summary 1.1 Likelihood Analysis and Final Event Selection 7.3.1 Likelihood Method and Test Statistics 7.3.2 Probability Distribution Functions 7.3.3 Frequentist Evaluation 7.3.4 Level7 - Final Event Selection and Sensitivities 7.3.5 Systematic Uncertainties 7.3.4 On-Time Events	77 78 81 82 84 85 88 96 97 97 98 02 05 08 10
7	Ray 7.1 7.2 7.3	rch for Low-Energetic Neutrinos from Collisionally Heated Gamma Bursts Experimental and Simulated Datasets Initial Event Selection 7.2.1 LowE-Level3 7.2.2 Level4 7.2.3 Level5 7.2.4 Level6 - Boosted Decision Trees 7.2.5 Rate Summary 1.1 Likelihood Analysis and Final Event Selection 7.3.1 Likelihood Method and Test Statistics 7.3.2 Probability Distribution Functions 7.3.3 Frequentist Evaluation 7.3.4 Level7 - Final Event Selection and Sensitivities 7.3.5 Systematic Uncertainties 7.3.4 On-Time Events	77 78 81 82 84 85 88 96 97 97 98 02 05 08 10 10

117

8 Conclusion and Outlook

Appendix A SnDaq Releases	119
Appendix B Valgrind output first testrun	121
Appendix C GRB catalog	123
Appendix DInitial Event Selection - Additional Plots and TablesD.1BDT Discrimination Variable Distribution PlotsD.2BDT Performance ChecksD.3Event Selection Rates on Levels 3-6	129
Appendix ELikelihood Method - Additional Plots and TablesE.1BDT Optimization Plots	137 137
Appendix F List of all On-Time Events	140
List of Figures	145
List of Tables	149
Bibliography	151

INTRODUCTION

The mysterious and multi-faceted nature of the *neutrino* singles it out as one of the most interesting objects in contemporary research. In recent decades more and more has become known about these particles, e.g. that they have non-vanishing mass, whose underlying mechanism is not clear yet. This discovery lead to an extension of the successful description of particle physics – the Standard Model of Particle Physics. For astroparticle physics, the neutrino provides an extremely well suited messenger particle as it is neither tremendously obscured by the interstellar medium nor deflected by magnetic fields. It is therefore in principle able to carry directional information about the original source across large astronomic distances.

One of several experiments aiming to exploit neutrino properties in order to find new or confirm proposed astrophysical neutrino sources is the *IceCube Neutrino Telescope*. Located in the Antarctic Ice sheet at depths of 1400 - 2400 m, it surveys a detector volume of one cubic kilometer with 5160 digital optical modules. Their active component – a 10" photomultiplier tube – thereby measures Cherenkov light that is generated by charged relativistic particles crossing the detector medium. The lower energy threshold for meaningful event reconstruction is hereby roughly 10 GeV which was achieved by the inclusion of the densely instrumented in-fill array *DeepCore*.

This thesis is dedicated to the detection of low-energy neutrinos, especially those originating from *Gamma-Ray Bursts* (*GRBs*) and *Supernovae* (*SNe*). While GRBs have already been investigated by multiple high-energy focused analyses within the IceCube collaboration, a newly proposed emission mechanism – the so-called inelastic collision model – turned GRBs into an interesting candidate class for a low-energy search. Not only that the model predicts a flux of neutrinos with energies of 10 - 100 GeV, the model can also naturally explain the observed gamma-ray spectrum. Eventually, as the neutrino energy is correlated to the jet's Lorentz factor, the analysis provides a handle on one of the most important quantities that characterize a GRB.

For the detection of neutrinos emitted by supernovae with a mean neutrino energy of about 10 MeV, a dedicated data acquisition system including a realtime statistical analysis method is used. With these tools, a search for Black Hole forming supernovae has been conducted. This particular type of supernovae may be a possible candidate for GRB-SNe, a supernovae subclass that represents a connection between GRBs and SNe. Therefore, both individual searches for GRBs and SNe as well as a search for coincidences between supernovae candidates and events assigned to GRB gamma emission will be performed.

In the second chapter, the neutrino as the main messenger particle from astrophysical sources will be introduced in the framework of the *Standard Model of Particle Physics*. Thereby, two neutrino properties will come in focus: their interaction with matter (especially with ice, which is used as detector material by the IceCube neutrino telescope) in various energy

regimes and the oscillation properties on their way through the vacuum and the Earth. A simulation to determine the neutrino flux at Earth given known oscillation properties has been developed in the course of this work. In addition, a major background for neutrino detection in IceCube – atmospheric muons from cosmic rays – will be discussed. As both neutrinos and muons will be detected with IceCube by exploiting the Cherenkov effect, a theoretical description of this effect will conclude the chapter.

In the third chapter, the astrophysical sources investigated in this work, Gamma-Ray Bursts and Supernovae, will be presented. For both, a gamma flux is predicted to be accompanied with a flux of low-energetic neutrinos. In the case of GRBs, the so-called *inelastic collision model* provides this prediction; for SNe a variety of models have been worked out. The expected neutrino spectra will be given and discussed for both source classes. At the end of the chapter, a possible connection between GRBs and SN will be outlined, introducing the so-called GRB-SNe.

The fourth chapter will present the *IceCube Neutrino Telescope* and its low-energy extension *DeepCore* covering the technical details as well as the underlying detection principle via the observation of Cherenkov emission. With regard of the analyses pursued in this work, the initial steps for producing suitable datasets will be presented. The chapter is concluded by an outlook on a possible further low-energy extension of IceCube – the planned PINGU detector.

The simulations that are used in this work to model the expected neutrino signals as well as the tools used for reconstructing the respective event signatures are presented in the fifth chapter.

The Supernova Data Acquisition System is introduced in the sixth chapter. Improvements in the stability of the system, yielding a higher uptime, will be presented. The main technical aspect of this work, however, is the implementation of a stable, efficient and realtime online muon subtraction within the data acquisition. This improvement significantly contributes to a correct interpretation of high-significance events detected by the data acquisition system. It also extends the detection efficiency for SNe in the Magellanic Clouds from 12 % to 77 %. The chapter concludes with the presentation of a search for Black Hole forming SNe that are possible candidates for GRB-SNe.

The seventh chapter presents an explorative analysis searching for low-energy neutrinos from collisonally heated Gamma-Ray Bursts. The event selection partly relies on well tested methods, including e.g. machine-learning algorithms. The main component of the analysis is a likelihood algorithm that provides a classification of events into signal-like and background-like events. Based on this classification, candidate events are searched for that occur in co-incidence with the GRBs' gamma emission using space, time and energy information. The most interesting on-time candidates will be presented in more details. The results of the like-lihood algorithm will be discussed in the context of four distinct stacked searches assuming different emission models. Also a single source investigation of the most gamma-luminous GRB in the dataset, GRB130427A, will be conducted.

A conclusion and an outlook towards the possible development and refinement of the analyses will be provided in the eighth chapter.

NEUTRINOS, COSMIC RAY BACKGROUNDS AND THE CHERENKOV EFFECT

Neutrinos are among the most mysterious particles known to modern physics. On the one hand, this makes them very interesting for current research, especially as some of their properties, e.g. their masses, are not determined yet. On the other hand, their elusive natures makes them excellent messenger particles for astrophysical events as neutrinos will neither be obscured by dust nor bent by magnetic fields.

The known properties of neutrinos are described by the *Standard Model of Particle Physics* (shorter: *Standard Model* or *SM*). This theoretical framework includes the interactions and properties of all elementary particles known as of today, except for the gravitation, whose interaction strength, however, is weak on elementary particle scales. Its success became particularly obvious with the detection of the *Higgs-Boson* that it predicted. Meanwhile, the original prediction of massless neutrinos had to be revised due to the phenomenological observation of neutrino flavor transformations (in the following referred to as neutrino oscillations), requiring non-vanishing and differing neutrino masses.

An overview of the Standard Model and its particle content is given in section 2.1, details about neutrino interactions – with emphasis on those in ice – are presented in section 2.2. A discussion on neutrino oscillations is provided in section 2.3. Afterwards, a major background for earth-bound neutrino detectors – atmospheric muons caused by interactions of cosmic rays in the earth's atmosphere – are presented in section 2.4. The chapter will conclude with a description of the Cherenkov effect which is exploited by neutrino telescopes such as IceCube for the detection of secondary particles produced in neutrino interactions.

2.1 The Standard Model of Particle Physics

The Standard Model is a quantum field theory describing the fundamental elementary particles and three of the four fundamental interactions known to date. While the SM includes the strong, weak and the electromagnetic force, it was not yet possible to consistently incorporate gravitation. The symmetry group of the SM is $SU(3) \times SU(2) \times U(1)$, in which the subgroup SU(3) is related to the strong force mediated by eight gluons coupling to the color *C*. The weak and electromagnetic interaction is represented by the electroweak group $SU(2) \times U(1)$ that couples to the weak isospin *I* and the weak hypercharge $Y = 2(Q - I_3)$ with the electric charge *Q* and the z-component I_3 of the weak isospin. The electroweak group symmetry is spontaneously broken via the *Higgs-Mechanism*¹ that eventually gives mass to

2

¹Actually, Anderson-Brout-Englert-Guralnik-Hagen-Higgs-Kibble-Mechanism. Named after the American physicists Philip Warren Anderson, Carl Richard Hagen and Gerald Stanford Guralnik, the Belgian physicists

the W^{\pm}/Z^{0} bosons carrying the weak force while the photon γ , mediating the electromagnetic interactions, remains massless. The mechanism postulates an additional massive particle, the *Higgs-particle*, whose existence was confirmed experimentally in 2012 [1, 2].

Besides the Higgs boson and the gauge bosons, the Standard Model also contains *fermions*: six *quarks* and six *leptons* organized in three generations each. Leptonic generations combine an electrically charged lepton (electron e, muon μ and tauon τ) with an uncharged neutrino named accordingly ν_e , ν_{μ} and ν_{τ} . Quark families consist of "up-like" quarks (up-quark u, charm-quark c and top-quark t) carrying electric charges $Q_{up} = 2/3$ and "down-like" quarks (down-quark d, strange-quark s and bottom-quark b) with $Q_{down} = -1/3$. The particle content of the SM and the classification into 1st, 2nd and 3rd generation is depicted in figure 2.1.

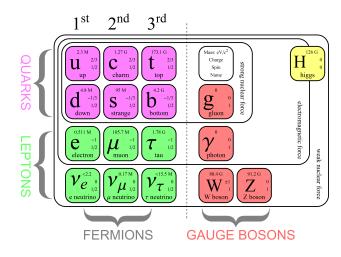


Figure 2.1: Elementary particles and interactions in the Standard Model (picture from [3]).

Matter in the SM is described as either purely leptonic or hadronic, the latter being a combination of quarks as either 3-quark states called baryons, e.g. protons (uud) and neutrons (udd) or as quark-antiquark pairs called mesons, e.g. pions $\pi^+(u\bar{d})$ or kaons K⁺(u \bar{s}). As for the quarks, also for most leptons a respective antiparticle is known with an opposite charge but the same mass, except for neutrinos for whom the question whether they are their own antiparticles (such particles are also called *Majorana particles*²) or not is subject to current research. One possible way to answer this question is the (non-)observation of the neutrino-less double beta decay $0\nu\beta\beta$: $(A,Z) \rightarrow (A,Z+2) + 2e^-$ that only takes place if neutrinos are of the Majorana type. This process is investigated e.g. by the GERDA³ experiment [4]. In the following, however, neutrinos and antineutrinos will be treated as different particles.

²Named after the Italian physicist Ettore Majorana.

Robert Brout and François Englert and the British physicists Peter Ware Higgs and Sir Thomas Walter Bannerman Kibble. Englert and Higgs earned the Nobel Prize 2013 "for the theoretical discovery of a mechanism that contributes to our understanding of the origin of mass of subatomic particles, and which recently was confirmed through the discovery of the predicted fundamental particle, by the ATLAS and CMS experiments at CERN's Large Hadron Collider".

³The Germanium Detector Array (GERDA) at the Laboratori Nazionali del Gran Sasso (Italy) consists of several germanium detectors measuring the neutrinoless double beta decay by searching for a peak in the energy transfer Q. Phase I of the detector did not find any evidence of its existence but set the most stringent limit of $T_{1/2}^{0\nu} > 2.1 \cdot 10^{25}$ yr (at 90 % C.L.).

2.2 Neutrino Interactions

Neutrinos are special compared to their lepton family partners as they do not carry electric charge and therefore are only subject to the weak interaction and gravitation. This makes them uniquely suited for transmitting information from astrophysical events, even at cosmological distances, as they are neither obscured by the interstellar medium (ISM) nor bent by magnetic fields. This characteristic makes it necessary to deploy large-volume detectors in which they can eventually react weakly with the detector material. As IceCube is a Cherenkov detector, the measured particle is not the neutrino itself, but secondary particles originating from neutrino reactions within the Antarctic ice (for more details on the detector and the ice see chapter 4). The kind of interactions and the secondaries produced depend on the energy of the incoming neutrino.

For the purpose of this work it is relevant to consider neutrino interactions in two different energy regimes: Supernova events are expected to produce large amounts of O(10 MeV) neutrinos (see section 3.2), whereas the investigated Gamma-Ray Burst models supposedly emit neutrinos of O(10 - 100 GeV) (see section 3.1).

2.2.1 The MeV-Regime

The main detection channel for neutrinos on this energy scale is the inverse β -decay contributing with about 93%, whereas electron scattering and reactions with oxygen each contribute with about 3% [5].

Inverse Beta Decay: The inverse β decay

$$\overline{\nu}_e + p \rightarrow n + e^+$$
 (2.1)

only contributes in the electron channel as the neutrino energies are not sufficient to generate muons or tauons. The minimal energy required for inverse beta decay is 1.8 MeV^4 for electron antineutrinos and therefore lower than the usual mean supernova neutrino energy of about 10 - 20 MeV. However, for the muon and tau channel, the required minimum energies are 113 MeV and 3.4 GeV, respectively, and thus almost impossible to reach for most supernova neutrinos. For neutrino energies E_{ν} in the range of 5 - 100 MeV, the mean positron energy can be parametrized as

$$\langle E_{e^+} \rangle = a \cdot E_{\gamma} - b, \qquad (2.2)$$

with parameters $a = 0.96 \pm 0.01$ and $b = 0.99 \pm 0.46$ MeV [6].

Electron Scattering: Furthermore neutrinos can scatter on electrons orbiting the ice nuclei in either charged current interactions (*CC*) by exchange of W^{\pm} bosons or via neutral current (*NC*) by the exchange of a Z⁰ boson:

$$\stackrel{(-)}{\nu_{e}} + e^{-} \rightarrow \stackrel{(-)}{\nu_{e}} + e^{-} (CC/NC)$$
 (2.3)

$$\langle \tilde{\nu}_l + e^- \rightarrow \tilde{\nu}_l + e^- (NC) \quad ,$$
 (2.4)

⁴ The minimum required energy calculates to $E_{\overline{v}_l} \ge \frac{(m_n + m_l +)^2 - m_p^2}{2m_p}$ for leptons $l = (e, \mu, \tau)$. Note that the speed of light *c* was set to c = 1 in the formula.

with $l = (e, \mu, \tau)$. As for the inverse beta decay, the production of muons and tauons is negligible, which effectively excludes CC interactions for the non-electron flavors.

Reactions with Oxygen: The oxygen in the ice is almost purely 16 O with a natural isotope abundance of 99.8 %. The most dominant neutrino captures on 16 O are the CC interactions

$$v_e + {}^{16}O \to {}^{16}F + e^-$$
 and (2.5)

$$\nu_{e} + {}^{16}\text{O} \to {}^{16}\text{N} + e^{+}$$
 (2.6)

NC reactions producing photons and protons emit significantly less light than the abovementioned reactions and are therefore neglected.

2.2.2 The GeV-Regime

In the GeV-regime, a variety of reactions becomes possible at different energies: NC elastic and CC quasi-elastic scattering (*QES*) of the neutrino on the whole nucleus, the inelastic resonance production (*RES*) possible in both CC and NC and eventually deep inelastic scattering (*DIS*). QES is hereby dominant below energies of 1 GeV, above it becomes subdominant to the RES. However, in the most interesting region for the investigated GRB neutrinos (10 – 100 GeV), the DIS is the main contribution to both ν and $\overline{\nu}$ CC cross-sections (see figure 2.2). It contributes in both the NC and CC channels

$$\stackrel{(-)}{\nu_l} + N \to l^{\pm} + X (CC) \tag{2.7}$$

$$\stackrel{(-)}{\nu}_{l} + N \to \stackrel{(-)}{\nu}_{l} + X (NC) , \qquad (2.8)$$

where, after neutrino scattering on the nucleus N, a hadronic cascade X is produced.

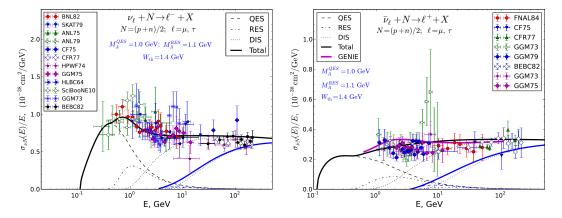


Figure 2.2: Neutrino (left) and antineutrino (right) CC cross-sections per energy for the neutrino scattering on isoscalar nuclei as function of neutrino energy E_{ν} . Shown are individually modeled QES, RES, DIS contributions to the muon cross-sections, inclusive ν_{μ} and ν_{τ} cross-sections and the antineutrino cross-sections used within the GENIE [7] simulation. The data points originate from ν_{μ} cross-section measurements. The factor three lower antineutrino cross-sections result from helicity suppression. Plot taken from [8] which uses data from [9].

2.3 Neutrino Oscillations and the Neutrino Mass Hierarchy

Of particular interest in the last decades of neutrino measurements was the question whether neutrinos carry mass. So far, no direct measurement has succeeded in answering this. However, the observation of neutrino oscillations requires a non-vanishing mass as it is a direct prerequisite for this phenomenon. A second requirement is that the neutrino flavor eigenstates $|v_a\rangle$ ($a = e, \mu, \tau$) are a superposition of the mass eigenstates $|v_i\rangle$ (i = 1,2,3). In that case, the flavor eigenstates variation with time t is given by

$$|\mathbf{v}_a(t)\rangle = \sum_{j=1,2,3} U_{aj}^* \mathrm{e}^{-\mathrm{i}E_j \cdot t} |\mathbf{v}_j\rangle \qquad , \tag{2.9}$$

with mass eigenstate energies E_j and the lepton mixing matrix U, also referred to as the *Pontecorvo-Maki-Nakagawa-Sakata* (*PMNS*)⁵ matrix [10]. A commonly chosen parametrization of this matrix is

$$U = \begin{pmatrix} 1 & 0 & 0 \\ 0 & c_{23} & s_{23} \\ 0 & -s_{23} & c_{23} \end{pmatrix} \cdot \begin{pmatrix} c_{13} & 0 & e^{-i\delta}s_{13} \\ 0 & 1 & 0 \\ -e^{i\delta}s_{13} & 0 & c_{13} \end{pmatrix} \cdot \begin{pmatrix} c_{12} & s_{12} & 0 \\ -s_{12} & c_{12} & 0 \\ 0 & 0 & 1 \end{pmatrix} \cdot \begin{pmatrix} 1 & 0 & 0 \\ 0 & e^{i\alpha} & 0 \\ 0 & 0 & e^{i\beta} \end{pmatrix}$$
$$= \begin{pmatrix} c_{12}c_{13} & s_{12}c_{13} & e^{-i\delta}s_{13} \\ -s_{12}c_{23} - e^{i\delta}c_{12}s_{23}s_{13} & c_{12}c_{23} - e^{i\delta}s_{12}s_{23}s_{13} & s_{23}c_{13} \\ s_{12}s_{23} - e^{i\delta}c_{12}c_{23}s_{13} & -c_{12}s_{23} - e^{i\delta}s_{12}c_{23}s_{13} & c_{23}c_{13} \end{pmatrix} \cdot \begin{pmatrix} 1 & 0 & 0 \\ 0 & e^{i\alpha} & 0 \\ 0 & 0 & e^{i\beta} \end{pmatrix}$$
(2.10)

with $s_{ij} = \sin \theta_{ij}$, $c_{ij} = \cos \theta_{ij}$, the mixing angles θ_{ij} , $i = (1,2,3) \neq j$, a CP-violating phase δ and two phases α and β that are different from zero if neutrinos were Majorana particles. For the sake of simplicity, α and β are assumed to be zero in the following discussion.

The probability for a neutrino, created in a pure v_a state at time $t_0 = 0$, to oscillate to a flavor *b* after a time *t*, is given by

$$P_{a \to b}(t) = \langle \mathbf{v}_b | \mathbf{v}_a(t) \rangle^2 \qquad , \tag{2.11}$$

which, using equation 2.9, yields a probability

$$P_{a \to b}(t) = \sum_{i,j=1}^{3} U_{ai} U_{bi}^{*} U_{aj} U_{bj}^{*} \cdot \sin^{2} \left(\Delta m_{ij}^{2} \cdot \frac{t}{4E_{\nu}} \right)$$
(2.12)

in vacuum with $\Delta m_{ij}^2 = m_i^2 - m_j^2$. Instead of equation 2.12, the equivalent form

$$P_{a\to b}(L) = \sum_{i,j=1}^{3} U_{ai} U_{bi}^* U_{aj} U_{bj}^* \cdot \sin^2 \left(\Delta m_{ij}^2 \cdot \frac{L}{4E_{\nu}} \right) \quad , \tag{2.13}$$

is often used, as the distance L between source and detector is measurable, while t is usually not [10]. As equation 2.13 is insensitive to the sign of Δm_{ij} , one can not gain any information about the individual neutrino masses.

However, it is possible to investigate this aspect by regarding matter effects within dense environments as the sun or other stellar objects. In such environments electron neutrinos

⁵Named after the Italian physicist Bruno Pontecorvo and the Japanese physicists Ziro Maki, Masami Nakagawa and Shoichi Sakata.

and electron antineutrinos experience charged current interactions with electrons in matter (ordinary matter mostly contains electrons besides the baryonic content). Those interactions can by described by an additional potential $V = \sqrt{2}G_F N_e$ with the Fermi⁶ constant G_F and the electron density N_e in matter. In a first approximation allowing only two flavor oscillations and slowly varying matter densities, the electron survival probability is calculated to be

$$P(\nu_{\rm e} \to \nu_{\rm e}) = \frac{1}{2} \cdot (1 + \cos 2\theta \cos 2\theta_{\rm m}) \quad , \tag{2.14}$$

where $\sin 2\theta_m = \Delta \sin 2\theta / \sqrt{(V - \Delta \cos 2\theta)^2 + (\Delta \sin 2\theta)^2}$ and $\Delta = m_2^2 - m_1^2$ in a two-flavor scenario $\theta_{ij} \rightarrow \theta$. As equation 2.14 depends on Δ instead of Δ^2 only, it allows one to obtain information about the sequence of the masses. Already in this approximative scenario, the *Mikheyev-Smirnov-Wolfenstein effect* (*MSW*)⁷ effect can take place which describes the change of the dominant neutrino flavor as it travels through matter of decreasing density. In this case, the neutrino eventually fulfills the resonance condition $V = \Delta \cos 2\theta$ which then yields a maximal neutrino mixing. If the process is not adiabatic, i.e. the matter density is highly varying, a flip of the mass eigenstates becomes possible which effectively changes the neutrino flavor. For a more detailed description of the effect (also in three flavor scenarios) see [11].

Taking the MSW effect into account, measurements of neutrino matter oscillations in the sun have lead to the determination of the sign and value of $\Delta m_{21}^2 = +(75.4 \pm 2.6) \,\mu\text{eV}$ [12]. For Δm_{31}^2 only the absolute value $|\Delta m_{31}^2| = 2.47 \,\text{meV}$ is known to date, but not the sign, leaving two possibilities for the neutrino mass ordering, the *normal hierarchy* (*NH*) where $\Delta m_{31}^2 > 0$ and the *inverted hierarchy* (*IH*) where $\Delta m_{31}^2 < 0$. Experiments with potential to determine the hierarchy are e.g. long-baseline experiments⁸ like Nova⁹ [13], the proposed PINGU experiment¹⁰ [8] or the investigation of core collapse supernovae as shown for IceCube in [5]. Besides neutrino oscillations, it is also possible to determine the hierarchy by using cosmological data [14] or the neutrinoless beta decay [15]. A combined analysis taking data from various experiments into account, including e.g. Nova, slightly favor a normal hierarchy at a significance level of 1.6 σ [16].

For the analysis presented in chapter 7, the measured flux at Earth is of particular importance. To determine the flavor distribution, it is helpful to consider neutrinos as wave packages with different mass eigenstates and as such with different group velocities. If the width of one wave package σ_x is smaller than the group velocity difference $\Delta v_{\text{group}} \cdot L/c$, the wave packet is no longer overlapping with those of other mass eigenstates. The coherence length can be determined to $L_{\text{coh}} = 4 \sqrt{2} \sigma_x \cdot E^2 / \Delta m^2 c^4$ [10]. As L_{coh} is smaller than the usually cosmological distances, the wave packets can be regarded as decoherent after traveling and therefore as

⁶Named after the Italian physicist Enrico Fermi.

⁷Named after the Soviet physicists Stanislav Mikheyev, Alexei Yuryevich Smirnov and the American physicist Lincoln Wolfenstein.

⁸Long baseline indicates the passing through Earth's crust, i.e. the influence of matter on the neutrino beam.

⁹The NOvA experiment (NuMI Off-Axis v_e Appearance at Fermilab's NuMI (Neutrinos at the Main Injector)) will produce a neutrino beam directed to the *Totally Active Scintillator Detector (TASD)* located at a distance of 810 km, that is used as the far detector. Its near detector is located at Fermilab.

¹⁰The *Precision IceCube Next Generation Upgrade (PINGU)* is a planned upgrade of the IceCube detector that will be able to answer the question of the mass ordering at a confidence level of 3σ after 3.5 yrs of data taking.

not oscillating any more. Consequently, one can average over equation 2.13 which simplifies eventually to the symmetric matrix

$$P_{a\to b} = \sum_{i=1}^{3} |U_{ai}|^2 |U_{bi}|^2$$
(2.15)

with entries

$$\begin{split} P_{e \to e} &= s_{12}^4 c_{13}^4 + c_{12}^4 c_{13}^4 + s_{13}^4 \quad, \\ P_{e \to \mu} &= (-e^{i\delta} s_{12} s_{13} s_{23} + c_{12} c_{23}) \cdot (-e^{-i\delta} s_{12} s_{13} s_{23} + c_{12} c_{23}) \cdot s_{12}^2 c_{13}^2 + \\ &\quad (-e^{i\delta} s_{13} s_{23} c_{12} - s_{12} c_{23}) \cdot (-e^{-i\delta} s_{13} s_{23} c_{12} - s_{12} c_{23}) \cdot c_{12}^2 c_{13}^2 + s_{13}^2 s_{23}^2 c_{13}^2 \\ &= P_{\mu \to e} \quad, \\ P_{e \to \tau} &= (-e^{i\delta} s_{12} s_{13} c_{23} - c_{12} s_{23}) \cdot (-e^{-i\delta} s_{13} s_{23} c_{12} + s_{12} s_{23}) \cdot s_{12}^2 c_{13}^2 + \\ &\quad (-e^{i\delta} s_{13} c_{23} c_{12} + s_{12} s_{23}) \cdot (-e^{-i\delta} s_{13} c_{23} c_{12} + s_{12} s_{23}) \cdot c_{12}^2 c_{13}^2 + s_{13}^2 c_{23}^2 c_{13}^2 \\ &= P_{\tau \to e} \quad, \\ P_{\mu \to \mu} &= (-e^{i\delta} s_{12} s_{13} s_{23} + c_{12} c_{23})^2 (-e^{-i\delta} s_{13} s_{23} + c_{12} c_{23})^2 + \\ &\quad (-e^{i\delta} s_{12} s_{13} s_{23} + c_{12} c_{23})^2 (-e^{-i\delta} s_{13} s_{23} c_{12} - s_{12} c_{23})^2 + s_{23}^4 c_{13}^4 \quad, \\ P_{\mu \to \tau} &= (-e^{i\delta} s_{12} s_{13} s_{23} + c_{12} c_{23})^2 (-e^{-i\delta} s_{13} s_{23} c_{12} - s_{12} c_{23})^2 + s_{23}^4 c_{13}^4 \quad, \\ P_{\mu \to \tau} &= (-e^{i\delta} s_{12} s_{13} s_{23} + c_{12} c_{23}) (-e^{-i\delta} s_{13} s_{23} c_{12} - s_{12} c_{23})^2 + \\ &\quad (-e^{i\delta} s_{12} s_{13} c_{23} - s_{23} c_{12}) + (-e^{i\delta} s_{13} s_{23} c_{12} - s_{12} c_{23}) (-e^{-i\delta} s_{13} s_{23} c_{12} - s_{12} c_{23}) + s_{23}^2 c_{13}^4 c_{23}^2 \\ &= P_{\tau \to \mu} \quad, \\ P_{\tau \to \tau} &= (-e^{i\delta} s_{12} s_{13} c_{23} - s_{23} c_{12})^2 (-e^{-i\delta} s_{13} s_{12} c_{23} - s_{23} c_{12})^2 + \\ &\quad (-e^{i\delta} s_{13} c_{12} c_{23} + s_{12} s_{23})^2 (-e^{-i\delta} s_{13} s_{12} c_{23} + s_{12} s_{23})^2 + c_{13}^4 c_{23}^2 \quad. \end{aligned}$$

Global fits yield the following best-fit $(\pm 1 \sigma)$ values for the angles and the CP-violating phase

$$\begin{split} s^2_{12,\,\mathrm{NH}} &= 0.297^{+0.017}_{-0.016} & s^2_{12,\,\mathrm{IH}} &= 0.297^{+0.017}_{-0.016} \\ s^2_{23,\,\mathrm{NH}} &= 0.437^{+0.033}_{-0.020} & s^2_{12,\,\mathrm{IH}} &= 0.569^{+0.028}_{-0.051} \\ s^2_{13,\,\mathrm{NH}} &= 0.0214^{-0.0009}_{+0.0011} & s^2_{12,\,\mathrm{IH}} &= 0.0218^{+0.0009}_{-0.0012} \\ \delta_{\mathrm{NH}}/\pi &= 1.35^{+0.29}_{-0.22} & \delta_{\mathrm{IH}}/\pi &= 1.32^{+0.35}_{-0.25} , \end{split}$$

for the assumption of a normal and an inverted hierarchy¹¹.

Using the values in equation 2.15 yields a neutrino flux composition at the earth's surface of

$$\begin{pmatrix} \nu_{e} \\ \nu_{\mu} \\ \nu_{\tau} \end{pmatrix}_{\rm NH}^{\rm Earth \ surface} = \begin{pmatrix} 0.56 & 0.23 & 0.21 \\ 0.23 & 0.39 & 0.38 \\ 0.21 & 0.38 & 0.41 \end{pmatrix} \cdot \begin{pmatrix} \nu_{e} \\ \nu_{\mu} \\ \nu_{\tau} \end{pmatrix}^{\rm production \ site}$$
(2.16)

¹¹Values taken from table 1 in [16]. Please note that this paper reports two minima for s_{23}^2 , where the used value in this work corresponds to the higher minimum. The evidence for the lower minimum at ~ 0.44 is reduced for a different dataset in the same paper. Also note that the best-fit range is about 10 % for the mixing angles while it is almost 50 % for δ .

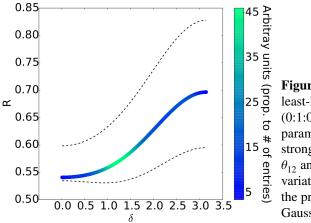
for the normal hierarchy and - for the inverted hierarchy - a composition according to

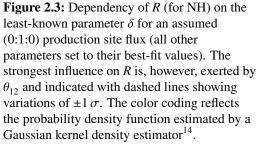
$$\begin{pmatrix} \nu_{e} \\ \nu_{\mu} \\ \nu_{\tau} \end{pmatrix}_{IH}^{\text{Earth surface}} = \begin{pmatrix} 0.56 & 0.18 & 0.26 \\ 0.18 & 0.44 & 0.38 \\ 0.26 & 0.38 & 0.36 \end{pmatrix} \cdot \begin{pmatrix} \nu_{e} \\ \nu_{\mu} \\ \nu_{\tau} \end{pmatrix}^{\text{production site}} .$$
 (2.17)

For the analysis presented in chapter 7, a flux at production site of composition ($\nu_e:\nu_\mu:\nu_\tau$) = (1:2:0) is assumed which transforms to a flux of composition (1.02:1.01:0.97) for NH and to a flux of (0.92:1.06:0.93) for IH, which – in good approximation – is an equally distributed flux at the surface of the Earth¹².

In principle, it is possible to distinguish production site fluxes by measuring the oscillated flux, as e.g. in NH a (0:3:0) flux oscillates to (0.69:1.17:1.14), which deviates more than 10% in all flavors from the (1.02:1.01:0.97), that a (1:2:0) production site flux oscillates to. One parameter, in which the distinction is clearly observable, is the ratio *R* between muon neutrinos and non-muon neutrinos given as $R = N_{\mu}/N_e + N_{\tau}$. The parameter has been investigated in a Monte Carlo (*MC*) simulation¹³ using 10,000 random realizations of *R*.

The influence of the parameter δ with the highest relative uncertainty is shown in figure 2.3 (while leaving the others parameters fixed). The variations are relatively small with maximal ~ 4 % for δ thrown within its 1 σ errors.





The distributions of R for the two exemplary production site flux ratios (1:2:0) and (0:1:0) are shown in figure 2.4 for the normal and the inverted hierarchy. The different flux ratios are obviously separable in both cases.

¹²Earth matter effect have to be included in the flux calculations afterwards.

¹³MC simulations are usually based on large samples of randomized experiments, for this purpose, however, a smaller sample is sufficient.

¹⁴This algorithm uses Gaussian kernels to estimate the probability density function of random variables. A description of the algorithm in general and Gaussian kernels in particular can be found in [17, 18].

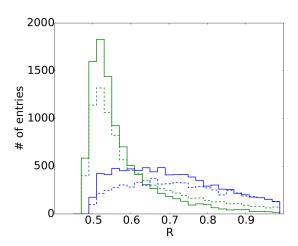


Figure 2.4: Histogram of the parameter R for (1:2:0) and (0:1:0) production fluxes in green and blue, respectively (NH in solid, IH in dashed).

2.4 Cosmic Rays and Atmospheric Backgrounds

As the neutrinos interacting in the ice produce leptons that can be observed with the IceCube detector, a major background for neutrino detection is caused by atmospheric leptons. The main contribution is caused by muons generated by *Cosmic Rays* interacting with particles in the Earth's atmosphere leading to large particle showers. Cosmic rays - in general terms meaning charged particles of cosmological, i.e. non-terrestrial, origin - mainly consist of free protons (79%) and helium nuclei (15%). The energy spectrum for those two and other contributing nuclei is shown in figure 2.5.

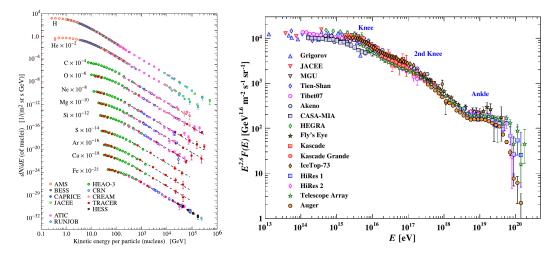


Figure 2.5: Cosmic ray fluxes per nuclei (left) and for all particles combined (right). Especially in the right plot, spectral features such as the knees and the ankle are visible (pictures from [19]).

Deviations from the general spectral index become apparent as the spectrum steepens at the *knees* at $10^{15} - 10^{16}$ eV and around 10^{17} eV and flattens at the *ankle* at about $10^{18.5}$ eV. The knees are usually explained by galactic accelerators reaching their maximum energies at those regions, e.g. *Supernova Remnants (SNRs)* at 10^{15} eV. Possible explanations for the ankle include a high-energetic extragalactic flux starting to dominate the low-energetic

galactic flux, or the energy loss caused by extragalactic protons interacting with the cosmic microwave background $p\gamma \rightarrow p + e^+ + e^-$ [19].

Cosmic ray particles interacting with air molecules in the atmosphere mainly produce pions and kaons. As a consequence, atmospheric muons and neutrinos are produced by the decays

$$\begin{aligned} \pi^{\pm} &\to \mu^{\pm} + \stackrel{(-)}{\nu_{\mu}} & (99.99 \% \text{ BR}) \\ K^{\pm} &\to \mu^{\pm} + \stackrel{(-)}{\nu_{\mu}} & (63.56 \% \text{ BR}) \\ K^{\pm} &\to \pi^{\pm} + \pi^{0} & (20.67 \% \text{ BR}) \\ & & \downarrow \mu^{\pm} + \stackrel{(-)}{\nu_{\mu}} & , \end{aligned}$$
(2.18)

with branching ratios taken from [19]. Additionally, electromagnetic cascades are produced by decays of neutral pions and kaons. Atmospheric muons mainly (~ 100%) decay with a lifetime of $2.2 \cdot 10^{-6}$ s via

$$\mu^{+} \rightarrow e^{+} + \nu_{e} + \overline{\nu}_{\mu}$$

$$\mu^{-} \rightarrow e^{-} + \overline{\nu}_{e} + \nu_{\mu} \qquad (2.19)$$

However, as the muons are highly relativistic, their lifetime is dilated, so that a significant fraction of them reaches the ground. Contrary to electrons and positrons created in air showers, muons and neutrinos can penetrate underground detectors, forming a major background. A measure for this is the vertical intensity I(h) defined as function of height h and density ρ :

$$I(h) = \int_{h}^{\infty} \rho h' dh' \quad . \tag{2.20}$$

The vertical intensities and fluxes in the atmosphere and underground are shown in figure 2.6.

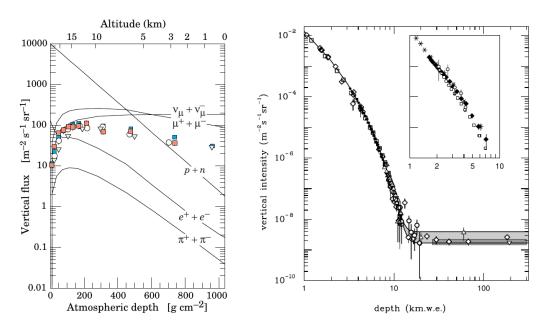


Figure 2.6: Vertical flux/intensity for various particles in the atmosphere (left) and underground for muons in rock (right, main picture) and ice/water (right, inset). The atmospheric depth on the right plot is given in kilometer water equivalent (picture from [19]).

The rate of atmospheric muons and neutrinos is subject to temperature variations in the atmosphere, leading to seasonal variations. An increasing temperature results in a decreasing atmospheric density, going along with an increased mean free pion/kaon path. The decay into muons is therefore possible on a longer path so that the muon rate increases with temperature and is thus higher in the Antarctic summer.

2.5 The Cherenkov Effect

The Cherenkov effect¹⁵ describes the emissions of photons when a charged particle passes through a dielectric medium. The short timed polarization of the atoms in this media evokes electromagnetic waves which interfere constructively at velocities larger than the phase speed of light c/n in this medium. The refraction index for ice n is ≈ 1.32 , with errors of 0.2 %/km caused by density variations in the Antarctic ice and 0.06 %/km due to temperature deviations [20]. The Cherenkov condition sets a minimum energy threshold E_{min} for electrons and positrons to generate Cherenkov light. In the ice, this threshold is given as $E_{min}^{ice} < 783 \text{ keV}^{16}$ which is well below the mean energy of neutrinos from supernova events. The emission as shown in figure 2.7 is radiated in forward direction under the characteristic Cherenkov angle $\vartheta_C = \arccos (c/vn)$.

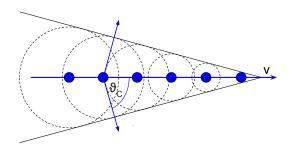


Figure 2.7: Schematic of the Cherenkov emission of a charged particle at velocity $v \approx c$. The constructive interference of the spherical waves leads to the formation of a wavefront extending under ϑ_C in forward direction (schematic modified from [21]).

The number of emitted Cherenkov photons per energy and distance intervals dE and dx is given by the Frank-Tamm formula¹⁷

$$\frac{dN_{\gamma}^2}{dEdx} = \frac{2\pi\alpha z^2}{hc}\sin^2(\vartheta_C)$$
(2.21)

$$\approx 370 z^2 \sin^2(\vartheta_C) \,\mathrm{eV}^{-1} \mathrm{cm}^{-1} \quad , \tag{2.22}$$

¹⁵Named after the Soviet physicist Pavel Alekseyevich Cherenkov, who was awarded the Nobel Prize 1958 "for the discovery and the interpretation of the Cherenkov effect".

¹⁶With $\nu/c = 1/n$ the Lorentz factor (named after the Dutch mathematician and physicist Hendrik Antoon Lorentz) is $\gamma = 1/\sqrt{1-1/n^2}$. The threshold energy $E_{\text{thresh}}^{\text{ice}} = \gamma m_0 c^2$ is consequently determined to 783 keV with an electron rest mass $m_0 c^2 = 511$ keV.

¹⁷Named after Ilya Mikhailovich Frank and Igor Yevgenyevich Tamm, Soviet physicists co-awarded the Nobel Prize 1958 "for [...] the interpretation of the Cherenkov effect".

with the Planck constant¹⁸ h = $6.63 \cdot 10^{-34}$ Js and the fine-structure constant $\alpha \approx 1/137$. For highly relativistic charged leptons (z = 1) traversing the ice, the above formula yields

$$\frac{\mathrm{d}N_{\gamma}^2}{\mathrm{d}E\mathrm{d}x} \approx 157\,\mathrm{eV}^{-1}\mathrm{cm}^{-1} \quad . \tag{2.23}$$

¹⁸Named after the German physicist Max Karl Ernst Ludwig Planck, who discovered the constant.

Astrophysical Sources of Low Energetic Neutrinos

In this chapter, the astrophysical sources, that are expected to provide a low-energy neutrino flux, are described. First, Gamma-Ray Bursts will be discussed, then Supernovae.

3.1 Gamma-Ray Bursts

Gamma-Ray Bursts are sudden outbursts of gamma radiation representing a class of astrophysical events with highest luminosities $L_{\gamma} \gtrsim 10^{53} \text{ erg s}^{-1}$. Detected in 1967 by the Vela satellites [22], they have critically been mistaken for nuclear weapon tests in the Earth's atmosphere, however, by now, it is known that they have non-terrestrial origins. A skymap of GRBs monitored by detectors on the Swift and Fermi satellites is shown in figure 3.1.

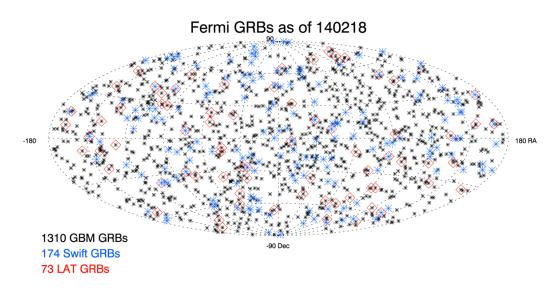


Figure 3.1: Skymap in declination and right ascension for Swift, Fermi-LAT and Fermi-GBM as of 18th February 2014 (graph from [23]). For a more detailed description of the satellite missions see section 3.1.3.

The Beppo-Sax experiment¹⁹ found X-ray emission setting in hours after the initial prompt γ ray detection – the so-called GRB *afterglow* [24].

¹⁹An Italian-Dutch X-ray satellite launched in 1996.

With more and more observations the theoretical models also improved. Two possible origins of GRBs are described in section 3.1.1. The mechanism of how particles in the collimated jets leaving the central engine are accelerated and which particles they interact with is, however, still under discussion. In section 3.1.2, the standard paradigm of jets and particle acceleration is compared to a more recently developed model of inelastic collisions in the jet. The latter predicts a low energetic neutrino emission that is investigated in this work. The section concludes with a list of the current satellite missions, which provide the GRB information for the analysis presented in chapter. 7.

3.1.1 Classification and Central Engines

A first distinction can be made by the durations of GRBs, dividing them into a *short* and a *long* GRB subclass (*sGRB* and *lGRB*, respectively). The duration defined to separate the classes is $T_{90} = 2 \text{ s} [25]$, where T_{90} refers to the time window in which the cumulative counts increase from 5% to 95%, and is thus an intensity-independent measure. This phenomenological distinction is connected to a different underlying GRB forming mechanism as sGRBs are expected to be produced in binary neutron star mergers [26, 27], while lGRBs are supposed to originate from *failed supernovae* – so-called *Collapsars* [28] (please find a more detailed description of the collapsar model in section 3.2.2.3).

In both cases, the central engine is considered to be a *Black Hole (BH)* surrounded by an accretion disk. For sGRBs, also *Neutron Stars (NSs)* with strong magnetic surface fields of $B \ge 10^{11}$ T (so-called *Magnetars* which – as simulation showed – can be formed by NS mergers [29]) have been proposed. Another candidate for the central engine of both GRB types is a *quark star* – a, not yet observationally confirmed, model of a star composed of quarks and gluons, forming in overdense neutron stars [30]. IGRBs in this model are related to the formation phase of the quark star in a supernova, while sGRBs are assumed to be caused by quakes in solid quark stars [31]. The X-ray component in the afterglow is explained in the quark star model by stochastic quark matter quakes.

However, in both cases, the enormous amount of thermal energy is described as a *fireball* consisting of photons, e^+/e^- , heavier nuclei, thermal neutrinos with O(10-20 MeV) energies and gravitational waves. The two latter can basically escape instantaneously as the progenitor star is transparent to neutrinos and gravitational waves while other particles are trapped as long as the optical depth²⁰ is larger than 1 [32].

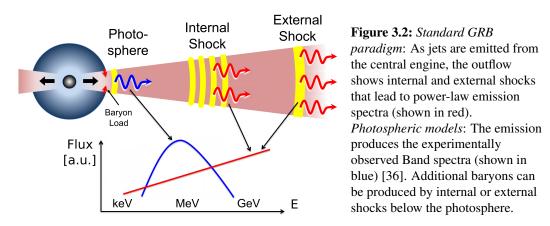
The emission from the central engines was proposed to be collimated in two opposite jets as otherwise GRBs would release isotropic equivalent energies of $E_{\gamma,iso} = O(10^{54} \text{ erg})$, which exceeds known mass limits. A collimated jet model, however, decreases the energy budget by ~ $\theta^2/2$ [33], with the jet's opening angle θ , and thus respects above mentioned mass limits. Further evidence for the collimated jet model was obtained by the observation of a break in the power law from a shallow to a steep stage in the afterglow of some GRBs by the Beppo-Sax experiment [34]. Such a spectral break is predicted by collimated jet models. Basis for this prediction is that for a jet with Lorentz factor Γ only an angular extent of $1/\Gamma$ is observable due to relativistic beaming. As long as that fraction is smaller than the jet opening angle, it is not possible to distinguish a relativistic jet from a sphere. This changes as Γ is decreasing

²⁰A measure of transparency. A medium is called *optically thin*, if its transparent for γ s and *optically thick*, if it is opaque for them

with time. When eventually $1/\Gamma > \theta$ is reached and the emission is collimated, one will see less radiation and consequently a break in the spectrum [33]. Although not all GRBs show such a spectral break, the collimated jet model is commonly used. In the following section, different models for particle acceleration in such jets will be presented.

3.1.2 Particle Acceleration: Standard Paradigm vs. Photospheric Models

GRB central engines in the standard paradigm emit jets that show shock structures due to internal collisions between particles in the outflow itself (*internal shocks*) and collisions of the emitted particles with the surrounding medium (*external shocks*), e.g. with the interstellar medium or remaining particle winds of the progenitor (see figure 3.2 which also shows the later described emission in photospheric models). The emission from external shocks is basically synchrotron emission from electrons accelerated in magnetic fields, however, as they can be trapped in a forward-reverse shock structure, they will eventually get slowed down [35]. The result is a shift to lower wavelengths and explains the afterglow emission in X-ray as well as in optical and radio bands. In the classic internal shock scenario, the γ s originate from the optically thin synchrotron emission of accelerated electrons in the jet. The resulting spectra for the internal and external shock emission follow power-laws. A schematic of them – also showing the spectra of the later described *photospheric model* – is displayed in figure 3.2.

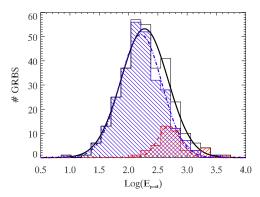


However, this description suffers from various problems explaining the observed peak energies of the bursts which cluster at $E_{\text{peak}} \approx 1 \text{ MeV}$ [37]. It also does not show a low-energy spectral index of $\alpha > -1$ observed for various GRBs but a softer $\alpha = -3/2$. Eventually the observed peak is usually sharp and can be fitted with a Band function²¹ consisting of two smoothly connected power laws with a low-energy power law index α and a high-energy index β . The function is given by

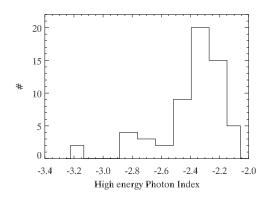
$$N_{E}(E) = \begin{cases} A \left(\frac{E}{100 \,\mathrm{keV}}\right)^{\alpha} \cdot e^{-E/E_{0}} & \text{if } (\alpha - \beta) \cdot E_{0} \le E, \\ A \left(\frac{(\alpha - \beta)E_{0}}{100 \,\mathrm{keV}}\right)^{(\alpha - \beta)} \cdot \left(\frac{E}{100 \,\mathrm{keV}}\right)^{\beta} \cdot e^{(\beta - \alpha)} & \text{else} \end{cases},$$
(3.1)

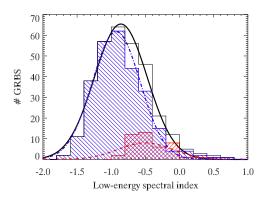
with normalization A and a reference energy E_0 [38]. Exemplary α , β and E_{peak} observed by Fermi are shown in figure 3.3.

²¹Named after the American astronomer David Louis Band.



(a) $Log(E_{peak})/keV$ for 318 Fermi-GBM GRB candidates. Black, blue and red histograms and accordingly colored Gaussian fits are shown for the full set and subsets of 274 long and 44 short GRBs, respectively.





(b) Low-energy spectral index α for 318 Fermi-GBM GRB candidates. Black, blue and red histograms and accordingly colored Gaussian fits are shown for the full set and subsets of 274 long and 44 short GRBs, respectively.

(c) High-energy photon index β for 60 Fermi-GBM GRB candidates that could be fitted with a Band Model. However, parameters shown in (a) and (b) could also be taken from GBRs that were fitted with a simple power-law or a power law model with an additional high-energy exponential cut-off.

Figure 3.3: Observed parameters E_{peak} , α and β in *a*, *b*, *c* (taken from [39]).

It should be noted that the problems within the synchrotron model also occur for other optical thin models. A possible solution for the above mentioned short-comings are so-called *photospheric* models, where the emission occurs close to the photosphere. Emission in such a case is a freely expanding radiation-dominated outflow which shows a Planck emission spectrum. However, as GRB spectra are typically non-thermal with extended tails, another component has to contribute which are either additional baryons in the jet or magnetic fields. The latter model also requires baryons in the jet with dissipation of the magnetic field leading to a conversion of magnetic into kinetic energy.

In the analysis presented in chapter 7, jets with additional baryons are investigated experimentally. In such jets, inelastic collisions between the emitted protons and neutrons produce pions that decay into positrons, electrons and neutrinos. This model will be referred to as *inelastic collision model* from now on. In contrast to the process that is favored in classical models:

$$\gamma p \to \Delta^+ \to n\pi^+ \to n\mu^+ \nu_\mu \to ne^+ \nu_e \nu_\mu \overline{\nu}_\mu \quad ,$$
 (3.2)

the possible reactions in the inelastic collision model are:

$$pp \rightarrow pn\pi^{+} \rightarrow pn\mu^{+}\nu_{\mu} \rightarrow pne^{+}\nu_{e}\overline{\nu}_{\mu}\nu_{\mu}$$

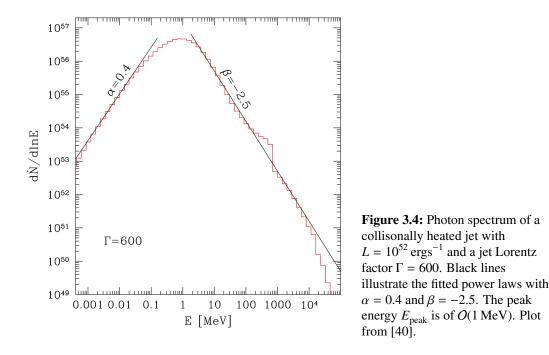
$$pn \rightarrow nn\pi^{+} \rightarrow nn\mu^{+}\nu_{\mu} \rightarrow nne^{+}\nu_{e}\overline{\nu}_{\mu}\nu_{\mu}$$

$$pn \rightarrow pp\pi^{-} \rightarrow pp\mu^{-}\overline{\nu}_{\mu} \rightarrow ppe^{-}\overline{\nu}_{e}\nu_{\mu}\overline{\nu}_{\mu}$$

$$nn \rightarrow pn\pi^{-} \rightarrow pn\mu^{-}\overline{\nu}_{\mu} \rightarrow pne^{-}\overline{\nu}_{e}\nu_{\mu}\overline{\nu}_{\mu}$$
(3.3)

In both models the pion decay leads to a neutrino flavor ratio of $(\nu_e:\nu_\mu:\nu_\tau) = (1:2:0)$.

Simulations of the inelastic collision model, taking an example from [40], yield GRB parameters $\alpha = 0.4$, $\beta = -2.5$ and O(MeV) peak energies (see figure 3.4) which are in good agreement with GRB measurements by the *BATSE* experiment²² [41] and Fermi-GBM [39]. In comparison to the simulation, the parameters measured by Fermi-GBM are slightly shifted (see figure 3.3 and [39]). However, all three values are of the same order of magnitude.



Neutrinos and Expected Neutrino Spectra: In total, there are three different sources for neutrino emission. While IceCube has set limits on the neutrino flux from Fermi accelerated ions in internal shocks that are responsible for the highest neutrino emergies (e.g. studied in an all-sky, three-flavor search [42]), inelastic collisions lead to neutrino emission in the GeV range. The energy of the emitted neutrinos is hereby correlated with the Lorentz factor Γ of the jet by $(1 + z) \cdot E_{\nu} \approx 0.1 \Gamma$ GeV, where z denotes the GRB redshift. Therefore, a measure of the neutrino energy provides a direct handle on one of the important GRB parameters [43]. A third way how to produce neutrinos – independently of collisions or interactions in the jet above – is the quasi-thermal emission from the central engine of the GRB itself, resulting in energies of O(10 MeV).

²²The Burst and Transient Source Experiment was a sodium iodide detector mounted on the Compton Gamma Ray Observatory (CGRO) operating until 2010.

The neutrino spectrum corresponding to the inelastic collision model was estimated in [44] and is shown by red lines in figure 3.5. In addition to the quasithermal neutrino flux (QT), coming from the bare inelastic collision model, two further components that may enhance the expected neutrino flux are shown as well.

The first one is the *Neutron-Proton-Converter* acceleration mechanism (*NPC*) [45]. The model was introduced to overcome the inefficiency of conventional Fermi acceleration at radiation-mediated shocks. It assumes that protons in a relativistic flow are converted into neutrons by hadronuclear collisions such as e.g. $p + p \rightarrow n + p + \pi^+$. As neutrons are not influenced by magnetic fields, they can propagate out of the flow, where a second transition back into a proton is possible, e.g. by spontaneous neutron decay. An energy gain is achieved by isotropization from the charged proton bending towards the flow and reentering it subsequently. The energy gain factor is given by $g = (\Gamma \cdot \theta)^2/2$ which reaches its maximal value $g \sim \Gamma^2$ for full isotropization $\theta \sim 1$ [46]. The acceleration is thereby much more efficient than the regular Fermi acceleration²³. As can be seen in figure 3.5, the energy spectrum is basically unchanged below the peak energy but broader above leading to a higher maximum energy. An additional power law component (*PL*), as assumed in classical models, was also considered.

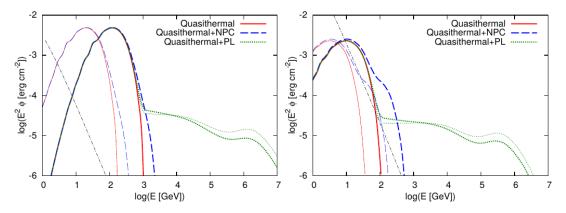


Figure 3.5: Combined $\nu_{\mu}/\overline{\nu}_{\mu}$ flux spectra for high- (left) and low-luminosity (right) GRBs (assuming $\varepsilon_{\gamma}^{iso} = 10^{53.5}$ erg at z = 0.1 and $\varepsilon_{\gamma}^{iso} = 10^{50}$ erg at D = 10 Mpc respectively). Models shown are QT emission only (in red), QT plus NPC emission (in blue) and QT plus PL (in green). PL indices of 2.1 (thick dots) and 2.0 (thin dots) are distinguished. The atmospheric neutrino background in 30 s (left) and in 1000 s (right) is displayed with a dot-dashed curve. *Left*: Shown are the predictions for $\Gamma = 100$ (thin lines) and $\Gamma = 600$ (thick lines). *Right*: Shown are the predictions for $\Gamma = 10$ (thin lines) and $\Gamma = 30$ (thick lines). The plots are taken from [44].

Most relevant in the scope of a GRB search with IceCube is the number of expected events in the detector which was calculated by [43] to n = 0.13 for GRBs taken from a 2 yrs Fermi-GBM + Swift-BAT sample in the northern hemisphere. Figure 3.6 shows a 20 yr expectation for the number of expected events with IceCube/DeepCore. The NPC, and particularly the PL component, contribute at higher energies.

²³Fermi acceleration in ultrarelativistic media $\beta = \nu/c \rightarrow 1$ indeed yields an energy gain of Γ^2 in the first cycle only, while afterwards the energy gain is ~ 2 as the jet is collimated within $\theta \sim 2/\Gamma$ [47].

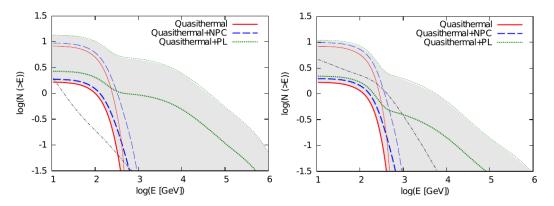


Figure 3.6: Expected event counts after coincident 20 yr observations with IceCube/DeepCore for combined $\nu_{\mu} + \overline{\nu}_{\mu}$ (left) and $\nu_{e} + \overline{\nu}_{e}$ (right) samples. The parameters and the color scheme match the models shown in figure 3.5. The plots are taken from [44].

3.1.3 Current Satellite Measurements and GRBWeb

For the analysis in chapter 7, different catalogs from various current satellite missions are taken into account.

The *Fermi Gamma Ray space telescope*²⁴, launched June 11, 2008, carries two GRB detectors, the primary *Large Area Telescope (Fermi-LAT)* and the complementary *GLAST Burst Monitor (GBM)*. Fermi-LAT is a pair conversion telescope with a self-triggering precision converter tracker and a calorimeter. The tracker converts γ rays passing its tungsten layers – chosen for their high charge number Z – to e⁺/e⁻ pairs whose energy deposition in the CsI calorimeter is measured. Fermi-GBM consists of twelve low-energy sodium iodide detectors orientated in different celestial directions and two high energy bismuth germanium oxide detectors orientated in opposite directions to provide almost full sky coverage [48]. The Fermi mission was extended to 2018.

The Swift spacecraft was launched November 20th 2004 carrying three instruments: the *Burst Alert Telescope (Swift-BAT)*, mainly responsible for the GRB detection, and the afterglow detectors *X-ray Telescope (Swift-XRT)* and *Ultraviolet/Optical Telescope (Swift-UVOT)*. BAT is constructed as a coded-mask imager with a lead tile mask and ~ 32 k CdZnTe detectors. Within 20 – 75 ns a BAT alert can trigger the spacecraft to rotate the UVOT and the XRT for further imaging of the GRB afterglow at different wavelengths [49, 50].

Other contributing missions are

- the *Konus* experiment on the *Wind* spacecraft (*Konus-Wind*), a two NaI crystal detector [51],
- the *Monitor of All Sky X-ray Image (MAXI)* on the International Space Station, carrying two types of X-ray slit cameras and two gas proportional counters working as X-ray detectors [52],
- the *Wide-Band All-Sky Monitor* on the *Suzaku* satellite (*Suzaku-WAM*), whose hard X-ray detector is made of 20 BGO crystal sensors [53],

²⁴The satellite previously known as *Gamma-ray Large Area Space Telescope (GLAST)*.

- the *SuperAGILE* experiment, a hard X-ray monitor on the *AGILE* satellite [54] that also carries the *Gamma Ray Imaging Detector* (*GRID*), composed of several silicon microstrip detectors as well as of a cesium iodide calorimeter, and
- the *International Gamma-Ray Astrophysics Laboratory (INTEGRAL)* containing an imager and a spectrometer as well as several soft-and hard X-ray and optical monitors [55].

In addition, some of these satellites as Fermi, AGILE, Suzuka, Swift, INTEGRAL and Wind are co-organized with the MESSENGER²⁵ [56] and the Mars Odyssey²⁶ [57] missions in the *Third Interplanary Network (IPN3)* that uses the timing information for one GRB detected by multiple satellites for a triangulation of the GRB location [58, 59]. An overview of the most important detector/mission parameters, including the angular resolution, the field of view and the respective energy range, is given in table 3.1.

Table 3.1: Composition of the most important parameters (angular resolution, field of view (FOV) and the energy range) for the missions considered in this work (taken from [42]).

Satellite/ Subdetector	Angular Resolution	FOV $[\pi \operatorname{sr}]$	Energy Range
Fermi-LAT	$1^{\circ} - 15^{\circ}$	3	$8 \mathrm{keV} - 40 \mathrm{MeV}$
Fermi-GBM	$0.1^{\circ} - 1^{\circ}$	0.8	$20 \mathrm{MeV} - 300 \mathrm{GeV}$
Swift-BAT	1' - 4'	0.5	15 – 150 keV
Swift-XRT	~ 3.5"	none	0.2 - 10 keV
Swift-UVOT	$\sim 0.5^{\prime\prime}$	none	170 - 650 nm (opt.)
Konus/Wind	none	4	10 keV - 10 MeV
INTEGRAL	1' - 2'	0.5	$8 \mathrm{keV} - 40 \mathrm{MeV}$
MAXI	1' - 2'	0.5	$8 \mathrm{keV} - 40 \mathrm{MeV}$
SuzukaWAM	none	2	$50 \mathrm{keV} - 5 \mathrm{MeV}$
SuperAGILE	1' - 2'	0.5	15 – 45 keV
IPN3	$0.1^{\circ} - 5^{\circ}$	4	1 keV – 1 MeV

GRBWeb: All missions presented in section 3.1.3 contribute to the *Gamma-ray Coordinates Network* $(GCN)^{27}$, by providing relevant information via emails²⁸. Fermi-GBM also holds data from additional detected GRBs in their own database that is accessed separately. The information is gathered on the IceCube-maintained archive *GRBWeb* [60, 42] and displayed on the associated website²⁹.

²⁵A satellite mission towards Mercury carrying the Gamma-Ray and neutron spectrometer (GNRS)

²⁶The Mars Odyssey mission provides two GRB detectors: the *Gamma Sensor Head(GSH)*, a germanium detector and the *High Energy Neutron Detector (HEND)* consisting of two Scintillation detectors.

²⁷Accessible via http://gcn.gsfc.nasa.gov/.

²⁸With an increasing level of processing needed for the distributed information within the email those are called "notice", "circular" and "report".

²⁹Accessible at http://icecube.wisc.edu/~grbweb/ (as of 26.2.2016) in a public version.

The parameters most relevant for this work are the GRB UTC time, the burst start and stop times T_1 and T_2 relative to the GRB time and the burst duration either given as T_{90} or T_{100}^{30} .

The gamma-ray localization in right-ascension and declination is also given with a corresponding angular 1 σ error. As the angular resolution is quite different for the participating missions (see table 3.1) the most precise measurement is taken first, defining an ordering of the satellites as: Swift-UVOT, Swift-XRT, Swift-BAT, SuperAGILE, Fermi-LAT, IPN3, Fermi-GBM, Maxi and INTEGRAL. Additionally, several gamma spectrum parameters are provided, describing the burst with broken power-laws (for details on those parameters please see [60]).

Finally, GRBWeb lists the IceCube run number for each GRB and marks, whether the run was found to be a good run, taking the good run-list criterions described in section 7.1 into account.

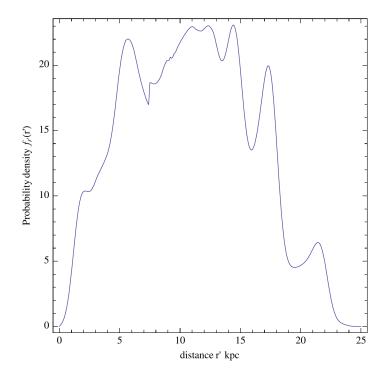
3.2 Supernovae

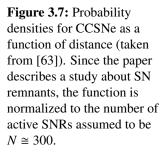
A second class of highly gamma-luminous events are the massive explosions at the end of the lifetime of high-mass stars – so called *Supernovae* (*SNe*). SNe are divided into subclasses according to their line spectra in the optical emission. Very coarsely, one may separate in Type I SNe that do not show hydrogen lines in the emission spectra and Type II SNe that do. Type I SNe are subsequently more finely classified into Type Ia, Ib and Ic SNe: Ia shows a single ionized Si line, Type Ib a neutral helium line at 587.6 nm and Type Ic has none of the mentioned absorption features. Type II is further classified according to characteristics of their respective lightcurve: Type IIP shows a plateau in the lightcurve, Type IIL a linear decrease. Type IIb shows spectra similar to Type II at early times but similar to Type Ib/c at later times. A more physics motivated method of distinction for neutrino detectors is the division into *thermonuclear SNe* that are SNe of type Ia and all others in the class of *Core Collapse SNe* (*CCSNe*). While the first one is of high importance as a standard candle in cosmological measurements, core collapse SNe are supposed to emit their energy in roughly 99 % as neutrinos resulting in emitted energies of ~ 10^{53} erg [61].

The SN data acquisition system in IceCube is most sensitive to Galactic SNe which limits the number of expected events to about a few SNe per century (see table X in [62]). The probability density as function of the supernova distance from the sun, taking the spiral structure of the Galaxy into account [63], is shown in figure 3.7. The inclusion of the *Magellanic Clouds*³¹ gives an additional contribution to the total SN rate of 2.5 - 4.6 per millennium assuming a SN Ia-to-CCSN ratio of 9:1 [64].

³⁰The GRBs duration is given as T_x , the time in which the observing satellite experiments report x % of a GRB's gamma emission.

³¹The Small and the Large Magellanic Clouds (*SMC* and *LMC*) are nearby dwarf galaxies at a distance of 61 kpc and 50 kpc, respectively.





3.2.1 Thermonuclear Supernovae

A Type Ia SN is the thermonuclear explosion of a carbon-oxygen *White Dwarf (WD)* in a close binary system. The original WD needs a binary companion for mass accretion close to the Chandrasekhar mass³². If the mass of the WD exceeds this limit, electron degeneracy can no longer sustain the gravitational pressure. However, carbon fusion starts for most of the WD before they reach this limit by the accretion of mass. This fusion process gets ignited throughout the star almost simultaneously, eventually triggering a thermonuclear carbon explosion – the Supernova. While the need for a companion is accepted, the nature of the binary system is still under discussion, favoring models with one WD and a main-sequence/subgiant or red-giant companion and models describing the merger of two WDs [65]. Thermonuclear SNe show similar variations and features in their γ -luminosity which makes them suitable as standard candles on cosmological distances.

The neutrino flux from a type Ia SN is estimated to be about four orders of magnitude lower than a core collapse SN neutrino flux [66]. An example Type Ia simulation results in the neutrino luminosities depicted in figure 3.8. The neutrino production processes taken into account are electron capture on protons and heavier nuclei, positron capture on neutrons and heavier nuclei and pair neutrino production by e^+/e^- -annihilations.

³²Named after the Indian astrophysicist Subrahmanyan Chandrasekhar. The Chandrasekhar mass is the maximum mass of a stable white dwarf given as $M_{\rm crit} = 5.76 \mu_{\rm e}^{-2} M_{\odot}$ with the mean molecular weight $\mu_{\rm e}$ per electron. $\mu_{\rm e}$ depends on the star's composition but is typically around two, e.g. for carbon or oxygen WD, yielding $M_{\rm crit} = 1.44 M_{\odot}$.

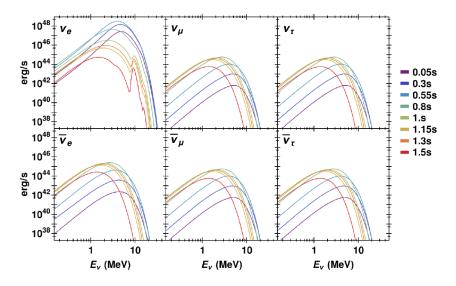


Figure 3.8: Total (anti-)neutrino luminosities at different times after explosion (picture from [66]).

The discovery potential with IceCube was calculated for this model, as shown in figure 3.9. It turns out to only reach beyond a 5σ level for very close SN Ia ($d \leq 50$ for NH, $d \sim 50$ for IH).

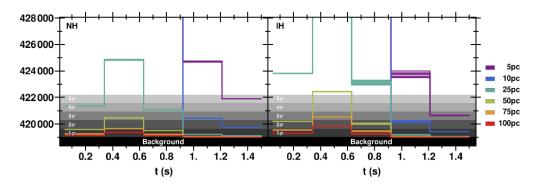


Figure 3.9: IceCube SN Ia event counts binned in 290 ms for NH (*left*) and IH (*right*) for different very close distances. In order to study neutrino oscillation effects, eight different azimuth and zenith combinations were simulated which, however, mostly overlap (plot from [66]).

In a study yielding similar results [5], the number of SNe Ia within 50 pc was estimated to about 5000 only, which makes a detection rather unlikely.

3.2.2 Core Collapse Supernovae

The neutrino emission looks more promising in the case of core collapse supernovae as the expected neutrino flux is orders of magnitudes higher than for SNe of type Ia. Core collapse SNe do not require a companion star, however, their initial mass has to be larger than about eight solar masses otherwise the star will end as a WD. The different evolution paths a star can take, depending on its mass, are shown in figure 3.10.

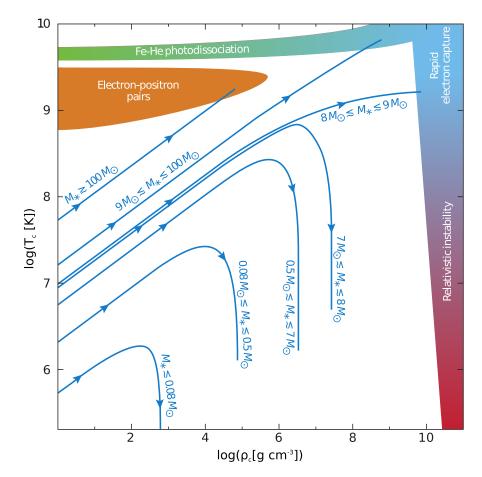


Figure 3.10: Star evolution paths for various progenitor masses. Low mass stars end up as WDs while heavier stars explode in SNe as they will reach one of the death regions named after the corresponding instability process which causes the collapse (picture modified from [67].

With the exhaustion of hydrogen fuel by the net burning reaction

$$4p \rightarrow {}^{4}He + 2e^{+} + 2\nu_{e} + 2\gamma$$

in the central region of the star, the core contracts gravitationally due to the accompanying decrease of outwards directed temperature pressure. However, the contraction increases the core's density and thereby the star's central temperature which then allows for the ignition of Helium burning in the triple-alpha process

$$^{4}\text{He} + ^{4}\text{He} + ^{4}\text{He} \rightarrow ^{12}\text{C} + \gamma$$

For massive stars, cycles of fuel depletion subsequently lead to a further contraction and to the ignition of the next burning stage, following the path shown in table 3.2. The final silicon burning leaves an iron core that can no longer produce energy by fusion. Almost each new stage takes less time, which is due to the underlying reaction itself and the acceleration of the process through neutrinos from thermal e^+/e^- annihilations: as those neutrinos can leave the core, the energy loss increases, leading to faster ignition of the next burning stage.

stage	time scale	main reaction	main products	<i>T</i> [10 ⁹ K]	ρ [g/cm ³]	$\frac{\frac{L_{\gamma}}{1000}}{[L_{\gamma, \bigodot}]}$	$\begin{array}{c} L_{\nu} \\ [L_{\nu, \bigcirc}] \end{array}$
Н	11 Myr	pp CNO	He He, N, Na	0.04	5.8	28	1800
Не	2 Myr	$\frac{3\alpha}{^{12}C(\alpha,\gamma)^{16}O}$	C O	0.2	1390	44	1900
С	2 kyr	$^{12}C+^{12}C$	Ne, Na, Mg, Al	0.8	$2.8 \cdot 10^5$	72	3.7·10 ⁵
Ne	0.7 yr	${}^{20}\text{Ne}(\gamma,\alpha){}^{16}\text{O}$ ${}^{20}\text{Ne}(\alpha,\gamma){}^{24}\text{Mg}$	O Mg	1.6	$1.2 \cdot 10^{7}$	75	$1.4 \cdot 10^8$
0	2.6 yr	¹⁶ O+ ¹⁶ O	Si, S, Ar, Ca	1.9	8.8·10 ⁶	75	9.1·10 ⁸
Si	18 d	$^{28}\mathrm{Si}(\gamma,\alpha)$	Fe, Ni, Cr,	3.3	$4.8 \cdot 10^7$	75	1.3·10 ¹¹
Fe	1 s	neutronization	n	>7.1	>7.3.109	75	>3.6.10 ¹⁵

Table 3.2: Burning stages of a 15 M_{\odot} star. Shown are typical time scales of the stages, the basic burning reaction, the resulting nuclei as well as important state variables as the temperature *T*, the density ρ and the luminosities of the star in photon and neutrino emission L_{γ} and L_{ν} . Table from [68], [69] and [70].

In the mass ranges of $M_* \leq 0.08 M_{\odot}$, $0.08 M_{\odot} \leq M_* \leq 0.5 M_{\odot}$, $0.5 M_{\odot} \leq M_* \leq 7 M_{\odot}$, $7M_{\odot} \leq M_* \leq 8M_{\odot}$ the star will develop into hydrogen brown dwarfs³³, helium WDs, carbon-oxygen WDs and neon-oxygen WDs, respectively. For heavier stars, the electron degeneracy limit will be reached eventually so that a gravitational collapse will be triggered. Depending on their mass, various types of core collapse SNe evolve.

3.2.2.1 Pair-Instability Supernovae

High mass stars with $M_* \sim 100 M_{\odot}$ will reach a region dominated by pair instability. After carbon burning, the temperature of such stars is about $T_* \sim 10^9$ K yielding high-energetic photons. Collisions of γ s with nuclei of the star will generate free electrons and positrons. This process drives a conversion of thermal energy to rest-mass energy, reducing the thermal pressure stabilizing the star. In a region of $140M_{\odot} \leq M_* \leq 260M_{\odot}$, the loss of thermal pressure is sufficiently large to allow for a fast gravitational collapse. The consequent ignition takes place if the next burning stage is strong enough to trigger a thermonuclear explosion and to disrupt the star completely, leaving no remnant at all. Lower mass stars will eventually go back to an equilibrium state before the complete disruption as the energy is sufficient for

³³Brown dwarfs are stars that gain energy by processes starting at lower temperatures than hydrogen fusion, e.g. lithium burning or deuterium fusion.

electron/positron creation, but not sufficient to trigger a supernova. Heavier stars will encounter photodisintegration which will be described in more details in section 3.2.2.2 which practically allows the star to collapse into a *Black Hole (BH)* instead of triggering a thermonuclear explosion. In the case of a BH formation, the expected neutrino emission is huge with a total energy of ~ $O(10^{55} \text{ erg})$. However, their estimated formation ratio compared with other core collapse SNe is only $\approx 0.1 - 1$ %.

3.2.2.2 Iron Core and Electron Capture Supernovae

The most common types of core collapse SNe are *Electron Capture SNe* and *Iron Core SNe*. For electron capture SNe the evolution ends with the formation of a NeOMg core as the Ne burning can not be ignited, for iron core SNe no further nuclear fusion can be started beyond the iron core, leaving it without temperature pressure against the infalling matter. In both cases the electron capture $e^- + p \rightarrow n + \nu_e$ becomes possible, for the iron core SNe the photodisintegration $\gamma + {}^{56}Fe \rightarrow 4n + 13\alpha$ as well. Both processes reduce the outward directed electron degeneracy pressure. In addition, the electron reduction processes also drive the neutronization of the core, eventually leading to a proto-neutron star. However, this collapse abruptly stops as the central region's density reaches nuclear density values. This makes the core opaque for neutrinos. Additionally, short-ranged nuclear forces become dominant and stall the infalling matter. The rebound results in an outwards traveling shock wave which is stopped by energy losses and infalling matter [69]. The final mechanism which eventually leads to reacceleration of the shock wave is subject to current research of thermonuclear, magnetohydrodynamic and acoustic models. Mostly, however, the energy deposited by neutrinos is assumed to be the main cause of the explosion retriggering. The revival of the stalled shock is hereby granted by the absorption of neutrinos generated in outer layers near the stalled shock front, providing an outward direct pressure gradient which eventually leads to the SN explosion [71]. Using this mechanism yields successful explosions of several 2D and 3D³⁴ SN models [67].

As the shock front leaves the core, the density decreases significantly on short time scales, making it possible for neutrinos (mostly electron neutrinos from the above mentioned electron capture) to leave the proto-neutronstar instantly, forming the so-called deleptonization peak. From the outer shells of the star, further matter is still accreted which induces additional neutrino generating processes as positron or electron captures on free neutrons and protons respectively, annihilation of e^+/e^- -pairs into $\nu/\overline{\nu}$ pairs and nucleon-nucleon bremsstrahlung $N + N' \rightarrow N + N' + \nu + \overline{\nu}^{35}$. With the accretion ending after O(1 s), a longer lasting cooling phase becomes observable in which neutrinos are mainly produced via the two latter pair production processes. Exemplary lightcurves with the mentioned phases for a low-mass core collapse SN are depicted in figure 3.11.

Depending on the progenitor mass, the remnant of the supernova is either, for low mass stars, the neutron star, or, for masses $\geq 40 \,\mathrm{M}_{\odot}$, a Black Hole. In an intermediate region of $25 \,\mathrm{M}_{\odot} \leq M \leq 40 \,\mathrm{M}_{\odot}$ Black Hole formation can be triggered after the shock front emission by accumulation of more infalling matter on the neutron star ("Black Hole by fallback") [73].

³⁴Dimensionality here refers to the assumed symmetry of the progenitor: in 1D, spherical symmetry is assumed, in 2D, axial symmetry and no symmetry is assumed in 3D.

³⁵In current simulations, the nucleon-nucleon bremsstrahlung potential is based on one-light-meson exchanges – usually considering pions but also ρ-mesons as in [72].

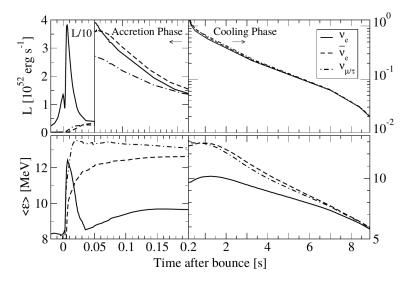


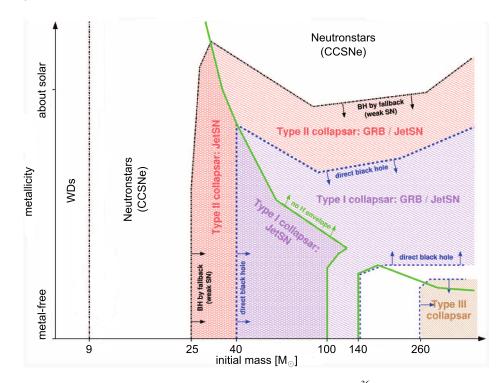
Figure 3.11: Neutrino luminosities and averaged energies in the Huedepohl model [74] (discussed in section 3.2.2.4). In the plot, the values for v_e , \overline{v}_e and the combined other flavors $v_{\mu/\tau}$ are shown.

3.2.2.3 Gamma-Ray Burst Supernovae

Aside from the parallel of low energetic neutrino production in CCSNe and GRBs, there is also evidence that some of their subclasses are connected: IGRBs and Ic-Type supernovae were sometimes found to occur simultaneously. Starting with the observation of the only 40 Mpc distant GRB980425 with the high energetic Type Ib/c SN1998bw $(2 - 5 \cdot 10^{52} \text{ erg/s},$ often referred to as a *Hypernova*) a connection seemed possible, but was doubted at first because of the extraordinary nature of the GRB's low luminosity of $5 \cdot 10^{46} \text{ erg/s}$. However, the association found more approval after observation of the high energetic GRB030329 and Type Ib/c hypernova 2003dh. The measured time delay between the SN and the GRB was less than two days [75, 76]. Further studies in the Swift-BAT era delivered even more evidence and gave more insight about the classification of a *GRB-SN*. In the *Collapsar* model [28], the following criteria need to be fulfilled in addition to those of common core collapse SNe:

- GRB-SNe are *more massive* than regular CCSNe and *rotating rapidly*: The star must be sufficiently massive to allow the star to form a Black Hole whose gravitational and rotational energy are assumed to power the GRB.
- The progenitor star has to be *compact* which means that it must not have an extended hydrogen envelope so that the GRB jets would not be blocked upon emerging from the central engine [67].
- The outflow has to be *relativistic* for a GRB. Otherwise, if a highly asymmetric outflow escapes, a so-called *JetSN* occurs.

Depending on when and how Black Hole formation happens, different Collapsar types are distinguished. *Type I Collapsars* occur at progenitor masses exceeding $40 \,M_{\odot}$ before the star undergoes core collapse, *Type II Collapsars* through Black Hole formation by fallback. In both cases, the proto-neutron star is formed which is not the case for supermassive progenitors



collapsing directly into Black Holes. The latter build the class of *Type III Collapsars* [73] (see figure 3.12).

Figure 3.12: Collapsar/SNR types in the progenitor mass - metallicity³⁶plane. In the low-mass and high-metallicity regions (white regions on top and left side) either WDs or NSs form. With increasing mass, BH formation becomes possible first by fallback of matter onto the NS (red colored regions) formed by Type II Collapsars then by direct formation (purple colored regions) of BHs by Type I Collapsars. Separated from them by the region of pair instability (white region on bottom right) are supermassive Type III Collapsars. GRBs can form in the regime of stars without H-envelope only (above green line), as otherwise the burst can not escape the star, a case in which JetSNe are observed. Plot modified from [73].

The fraction of SNe producing GRBs is nowadays quite small with a ratio of 1/1000, but as GRB-SNe have been found more often in low-metallicity environments favoring rapidly rotating helium stars, they might have been more common in the early universe.

Collapsar are candidates for gamma-ray bursts if their angular momentum is in the range of $3 \leq j/(10^{16} \text{ cm}^2 \text{s}^{-1}) \leq 20$ (found for a 35 M_{\odot} model in [28]). The angular momentum determines where the accretion disk of the Black Hole forms. If *j* is too small, the disk would form at a distance smaller than the radius of the last stable orbit for a Schwarzschild Black Hole³⁷ which means that no outflow could escape. If it forms too far outside – meaning *j* is

³⁶Metallicity is the fraction of a star that is "metal", which for simplicity means everything but hydrogen and helium. Solar metallicity is about 0.013 as the sun contains about 0.74 % hydrogen and 0.25 % helium [77].

³⁷A Schwarzschild Black Hole is an uncharged non-rotating Black Hole described by the Schwarzschild metric. Named after German physicist Karl Schwarzschild, a Schwarzschild metric is a solution of the vacuum Einstein equations, named after the German-born/Swiss/American physicist Albert Einstein who described gravitation as a result of curved space-time.

too large – energy loss due to neutrinos become less relevant. Without this additional energy dissipation stable disk formation becomes less probable and the accretion rate is lower. In the preferred angular momentum interval, however, neutrino energy deposition in the polar regions was shown to be able to induce two outward directed jets. The shock front breaking through the star will be detected first and takes place around 10s after the initial core collapse [28]. The actual GRB happens later, if the Lorentz factor becomes large enough. If this does not happen and the outflow remains non-relativistic a JetSN takes place instead.

3.2.2.4 Expected Neutrino Energies

Of particular importance for a supernova analysis is the mean neutrino energy which eventually determines the main detection channel of the IceCube telescope, properties of neutrino transmission in the ice and important measures as angular and energy resolution. As there is a variety of models for the explosion mechanism, there is also a range of neutrino energies. For the low-mass extreme case of an electron capture SNe the *Huedepohl model* describing a SN with 8.8 M_☉ predicts anti-electron neutrinos of ~ 10 MeV energy, see figure 3.11, whereas the high-mass extrema of a Black Hole-forming SN with 40 M_☉ yields ~ 15 – 25 MeV energies and only slightly higher mean antielectron neutrino energies, see figure 3.13. Note that the progenitor of the latter model is non-rotating so it does not completely model the situation of a GRB-SN. For an intermediate case, a numerical 1D simulation of a 20 M_☉ progenitor, modeling the supernova 1987A³⁸, is used: the *Lawrence-Livermore* model, also shown in figure 3.13.

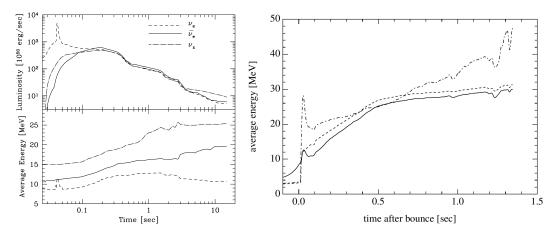


Figure 3.13: *Left*: Neutrino luminosities and average neutrino energies in the Lawrence-Livermore model [79]. *Right*: Averaged neutrino energies for a Black Hole-forming SN model [80]. In both plots, the values for v_e , \overline{v}_e and the combined other flavors v_x are shown. The Black Hole model plot uses the same line style encoding as in the Huedepohl model shown in figure 3.11.

³⁸For SN 1987A, neutrinos have been detected by several neutrino telescopes over a time of 12 s. By the observation new limits could be placed on the neutrino masses, charges and lifetimes [78].

NEUTRINO DETECTION WITH THE ICECUBE NEUTRINO TELESCOPE

The *IceCube Neutrino Telescope* (short: *IceCube*) is a Cherenkov detector located at the geographic South Pole, measuring the Cherenkov light emitted from secondary particles caused by neutrino interactions in the Antarctic Ice. In this chapter, the layout of the detector and its low-energy extension DeepCore as well as the main detector components and the properties of the surrounding ice will be described. As the amount of data measured with IceCube is tremendous, first data selection steps are outlined. Afterwards, a presentation of the expected signal and background event signatures in the low-energy regimes relevant to this work will be given. The chapter will conclude with a short outlook towards the planned low-energy PINGU extension.

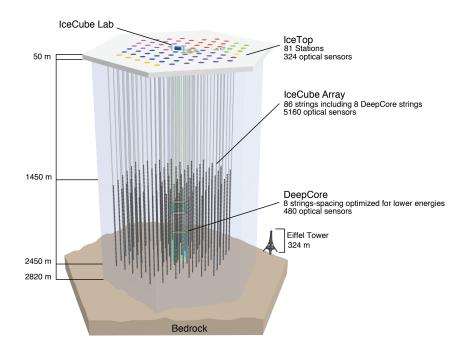
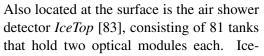


Figure 4.1: The IceCube detector with its 86 strings including the DeepCore subdetector (in green). The color coding on the surface represents various configurations: IC1 in yellow, IC9 in green, IC22 in red, IC59 in purple, IC79 in blue and IC86 in orange. Scheme from [81]

4.1 IceCube/DeepCore

IceCube, as shown in figure 4.1, consists of 86 steel strings - with optical sensors and cables attached - that were deployed between 1450 m and 2450 m depth with a horizontal inter-string distance of 125 m. The strings were drilled into the Antarctic Ice shelf using hot water. In this process, the refrozen water in the 60 cm boreholes formed the so-called *hole-ice*, which, due to the drilling process, contains impurities such The construction of the detector as air. started 2005 and was finished by the end of 2010. The detector was augmented in stages while the data taken during this time was named after the deployed number of strings - namely IC1, IC9, IC22, IC40, IC59, IC79, and finally IC86. The naming scheme was modified after completion and uses the respective data taking season, starting with IC86-I, ranging from 1st of April 2011 to 15th of May 2012. Usually, changes in hardor software are introduced with such a new, roughly 1 yr long season.

Sixty *Digital Optical Modules* (see section 4.2) are mounted on a string with a vertical 15 m spacing. The data recorded by such an optical module is transferred along the strings to the surface *IceCube Laboratory* (*ICL*) for a first processing.



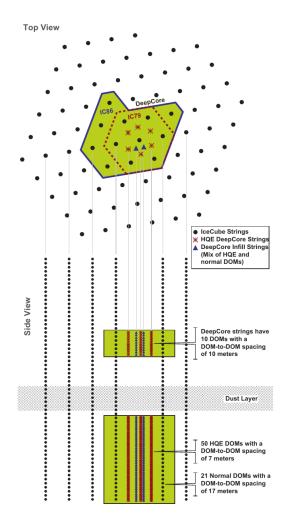


Figure 4.2: The DeepCore subdetector and its fiducial volume in green, including eight DC strings highlighted in red, and two DC infill strings in blue. Picture from [82].

Top's scientific possibilities include the search for astrophysical events such as PeV gamma rays or solar flares, but it also works as a down-going³⁹ muon veto for the in-ice detectors.

Of particular interest for a search for low-energetic neutrinos is the *DeepCore* subdetector (DC), shown in figure 4.2. DeepCore is located around the central IceCube string and is separated into an upper and a lower part. By this intentional division, DeepCore is only located in the clearest ice as the region between the two parts of the subdetector – the so-called *dust layer*, which shows higher photon absorption and scattering (see section 4.4) – is not instrumented. The upper part of DeepCore as well as the whole IceCube detector can be used as a veto for the bottom part of DeepCore. DeepCore's deployment started in 2009

³⁹A particle is called "down-going", if it enters the detector in the direction from above the horizon.

with one string and was finished by 2011 with 20 strings belonging to the DeepCore fiducial volume. In this volume, as can be seen in figure 4.2, DeepCore is symmetrically surrounded by a three layer veto.

The extension of the energy range to lower values was achieved by a reduction of the interstring horizontal distances to 42 - 72 m and the reduction of the DOM-to-DOM distance, which is 10 m in the top part and 7 m in the bottom part. This lowers the energy threshold of a few hundred GeV for IceCube to ~ 10 GeV with the DeepCore subdetector [84]. Additionally, for some strings in the DeepCore fiducial volume, optical modules with a higher quantum efficiency – so-called *HighQE DOMs* – are used (see section 4.2), which also contribute to the lower energy threshold.

4.2 Digital Optical Modules

As each string carries 60 Digital Optical Modules (*DOMs*), IceCube consists of 5160 DOMs in the final IC86 configuration, of which only 87 are not working properly and therefore are excluded from the data-taking as well as 171 DOMs that are only working in a non-standard mode [85]. The relative number of DOMs working without problems accounts to 95 %.

The DOMs (see schematic in figure 4.3) consist of photomultiplier tubes described below and are enclosed by a 13 inch diameter sphere made of 0.5 inch thick borosilicate glass.

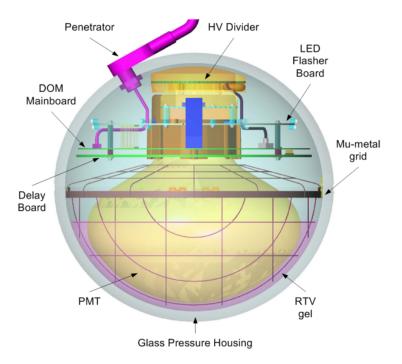


Figure 4.3: The DOM and its main components: PMT and electronics embedded in a glass pressure housing.

The glass shows good photon transmission in the spectral response region of the photomultiplier as well as a low dark noise rate, which was achieved by a reduction of the, usually strong, influence of ⁴⁰K decays to less than 100 Bq. The remaining radioactivity in the glass is mainly caused by trace elements from uranium and thorium decay chains [86]. The glass sphere is coupled to the PMT by an optical gel made of room temperature vulcanizing (RTV) silicone. The usage of the gel combined with the glass properties leads to a lower cutoff of the spectral response of the PMT around 350 nm. The PMT is orientated downwards, which maximizes sensitivity for up-going particles. The DOM is completed with a mainboard for reading and digitization of the data (see section 4.2.2), a high-voltage divider, a flasher board carrying twelve LEDs e.g. used for calibration, and a 75 ns-delay board providing the signal to the DOM mainboard. To shield the PMT against the terrestrial magnetic field, they are surrounded by a μ -metal grid.

4.2.1 Photomultiplier Tubes

IceCube/DeepCore uses photomultiplier tubes (*PMTs*) made by Hamamatsu in two different versions. Mostly deployed in IceCube are 10 inch PMTs of Type R7081-02 (for characteristics see table 4.1); for most of DeepCore, PMTs of Type R7081-MOD are used instead. The DeepCore PMTs show the same characteristics as the standard ones, except for the quantum efficiency, which is roughly 1.35 higher relative to the standard PMT [84]. Therefore PMTs of Type R7081-MOD are named *highQE*-PMTs in the following.

spectral response coverage	300 – 650 nm
spectral peak wavelength	420 nm
quantum efficiency (at 390 nm)	25 %
number of dynode stages	10
nominal gain	10^{7}
single photoelectron pulse (at gain of 10^7)	$\sim 8mV$

 Table 4.1: Characteristics of the photomultiplier tube R7081-02 used in IceCube [87].

The higher quantum efficiency implies a higher dark noise rates for highQE PMTs of about 720 Hz compared to roughly 540 Hz for the standard DOMs [86]. Both values are valid in temperature ranges from -40 °C to -20 °C [87]. A listing of the highQE DOMs in Ice-Cube/DeepCore is given in table 4.2. Of the total 20 strings in the DeepCore fiducial volume, six are fully equipped with HighQE DOMs, three partly, and eleven with standard DOMs.

String type	String number	DOM number	count
DC strings	81-86	1-60	360
DC infill string	79	30, 31, 33-40, 42, 44	12
DC infill string	80	30-43	14
central string	36	44, 46, 48-59	14
string outside DC fiducial volume	43	55	1

401

Table 4.2: List of highQE DOMs in IceCube.

4.2.2 Digitization

Digitization of the PMT signal takes place on the DOM's mainboard (see schematic in figure 4.4) which holds several digitizers and a scaler as well as a field-programmable gate array (*FPGA*).

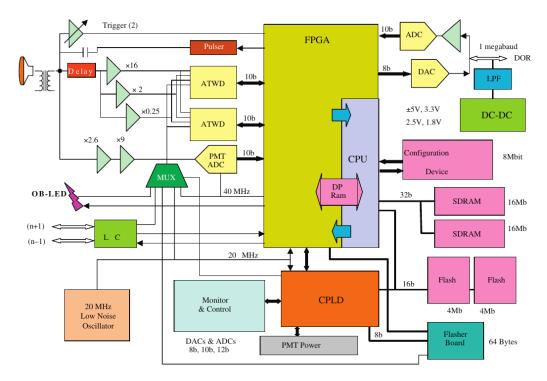


Figure 4.4: Schematic of the DOM's Mainboard (taken from [88]). The not-included SN scaler is located on the FPGA and gets its input directly from the discriminator.

If a PMT signal exceeds a discriminator threshold of 0.25 SPE^{40} , it will be counted as a *hit* (also referred to as *launch*) and forwarded to the various kinds of digitizers.

The method of digitization depends on the subsystem that further processes the data. For the standard analyses, investigating a hit-based stream, two ATWDs⁴¹ and one fADC⁴² are used for digitization. For supernova searches the hits are digitized by a scaler instead.

ATWD and fADC: The ATWD is a waveform digitizer taking the PMT's signal in three different amplifications (with amplification factors of 0.25, 2 and 16) after a delay of 75 ns purposely introduced by the delay board to account for the ATWD launch time of \sim 70 ns. It stores 128 analogue samples in each channel that get digitized by 128 internal ADCs. The ATWD sampling rate of 300 mega samples per second enables it to capture waveforms up to 426.6 ns in 3.3 ns resolution. The actual timestamp is provided in even better resolution (\sim 20% of the minimal resolution) by a determination of the waveform's leading edge. Full

⁴⁰One *single-photoelectron pulse* (SPE) corresponds to roughly 2 mV.

⁴¹Analogue Transient Waveform Digitizers

⁴²fast Analogue Digital Converter

digitization by one ATWD takes up to 29 μ s per amplification channel⁴³. To minimize the arising deadtime, the DOM holds two ATWDs with one being able to work in the other's processing time. For longer signals, an fADC is used that continuously samples with a working frequency of 40 mega samples per second, giving a minimum resolution of 25 ns. Leading edge digitization of the waveform can improve this as well to an actual resolution of roughly 4.7 ns. The length of the fADC record was set to 6.4 μ s [88].

For both digitizers, the question whether the full waveform is recorded or only summarizing information about the peak position is stored, depends on the *local coincidence condition* that is fulfilled by the respective hit. Local Coincidences (*LCs*) on a DOM-to-DOM basis, serve as a first step to reduce the amount of data for further processing and to suppress uncorrelated noise. A DOM hit is flagged as a *Hard-Local Coincidence* (*HLC*) hit, if a neighboring DOM triggers within 1 μ s. "Neighboring" is hereby defined as lying at most two DOMs distant to the initial hit-recording DOM in either direction on the same string. The full waveform information is recorded for hits fulfilling the HLC condition. For non-HLC hits – also called *Soft-Local Coincidence* (*SLC*) hits – only a minimal set of information, including the timestamp, is stored. The HLC rate is 2 – 25 Hz per DOM [89], depending on the depth.

Scaler: For Supernova searches, the discriminator pulses are collected in a hit counter. As this 16 bit scaler records at a rate of 40 MHz, the binning interval calculates to $2^{16}/40 \text{ MHz} = 1.6384 \text{ ms}$. In order to suppress dark noise, an artificial deadtime of 250 µs is applied by the FPGA [5]. This reduces the initial dark noise rate to ~ 290 Hz for the standard PMTs and to ~ 360 Hz for highQE DOMs.

After digitization the data is transferred to the surface ICL via single twisted copper wire-pairs which also serve as power supply cables for the DOMs.

4.3 Data Acquisition and Processing

Arriving in the ICL, the data will be further processed in the infrastructure of the *production Data acquisition* (*pDaq*). First, the data is read in by the *StringHub* software running on the *DOMHub* servers, each carrying eight *DOM readout* cards (*DOR* cards) that steer eight DOMs. The waveform information is buffered on the DOMHubs until the software trigger makes a decision to either request the full hit information or to discard it as noise. In contrast to the waveform information, the supernova scaler data is provided with a header containing timing information and is then directly forwarded to the dedicated *Supernova Data acquisition system* (*SnDaq*) (see chapter 6). Besides those two streams, also an untriggered dataset called *HitSpooling* [90] is available which buffers all hits for a period of 150 hrs [91]. Those data can be saved and send to the North⁴⁴ by either manual or automatic requests that are e.g. issued by the SnDaq. A schematic of those data streams is shown in figure 4.5.

⁴³First the channel with highest amplification is used, then consequently lower amplification channels if their precursors overflow.

⁴⁴ "The North" refers to the disk servers at Madison, Wisconsin, called *data warehouse*. In general, it may also mean the parts of the world that are not Antarctica.

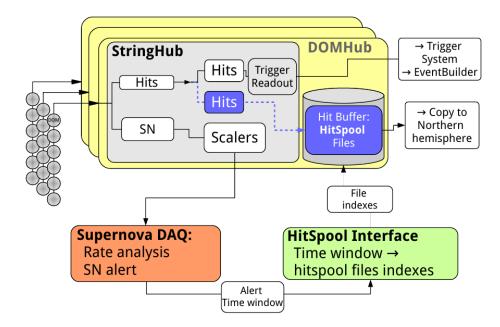


Figure 4.5: Overview of the different data streams and daq systems, including the supernova stream via scalers to the SnDaq, the HitSpooling buffer, where untriggered data can be request by e.g. SnDaq and the event-based hit stream forwarded to the trigger system (taken from [90]).

4.3.1 Trigger System

In order to reduce the enormous amount of data and to provide datasets that contain only the needed information for various analyses, Triggers are introduced. For this work, the most interesting triggers are the Simple Multiplicity Triggers (SMTs). The multiplicity used depends on the part of the detector the respective analysis focuses on. For IceCube analyses, an SMT8 condition is used, for searches, e.g. looking into low-energy events, an SMT3 is defined in the DeepCore fiducial volume. For both SMT conditions, a trigger window is defined, in which a certain number of hits has to occur to fulfill the trigger condition. This window is 5 μ s for the SMT8 and 2.5 μ s for the SMT3 condition. These windows are extended as long as hits are found fulfilling the trigger condition. The readout window is later extended again to cover early and late hits (e.g. for the SMT8 to 4 µs before the first hit and 6 µs after the latest hit. In the SMT3 case, the trigger windows gets extended by $6 \,\mu s$ on both sides [91]). In addition to the simple multiplicity triggers, other conditions take hit topologies into account. Examples are the string trigger, that is passed if seven adjacent DOMs on a string register five hits in 1.5 μ s or the *volume trigger*, which triggers if four HLC hits within 1 μ s occur in a cylindrical volume of radius r = 175 m and height h = 75 m. Rates as of May 2013 on the respective trigger-level (also level1) are 2.1 kHz for the in-ice SMT8, 250 Hz for the DC SMT3 and 3.7 kHz and 2.2 kHz for the in-ice volume and string trigger, respectively [89]. In order to avoid a hit appearing in different events, several triggers may be merged by the Event Builder to a Global Trigger as shown in figure 4.6. All events are then forwarded to the *Processing and Filtering* system (*PnF*).

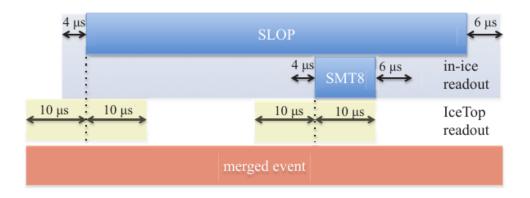


Figure 4.6: Merging of IceTop trigger windows with an in-ice SMT8 trigger and a long *Slow Particle* (*SLOP*) trigger event (taken from [89]).

4.3.2 Filter and Hit Cleaning

Consisting of 20 servers, the *Processing and Filtering* system (*PnF*) is able to perform initial reconstructions and event selections in order to provide datasets that are specialized for various purposes, e.g. for extracting events from a certain source direction as the moon filter or events from a certain secondary particle as the muon filter. PnF also runs the so-called *Feature Extractor* (*FE*) on the hits which unfolds the waveform of each hit in order to find hits that are build up from more than one photon. Thereby the FE searches for one or more peaks in the charge spectrum and assigns them to individual *pulses* that are mostly used for event reconstruction instead of launches.

In the analysis described in chapter 7, the focus is on low-energy events detected by the DeepCore subdetector, so data passing the *DeepCore filter* is used. In this filter, the algorithm is only run on a subset of cleaned hits.

Hit cleaning aims at removing noise hits while preserving signal hits. In IceCube, two kinds of hit cleaning are used, the classicRT (cRT) and the seededRT (sRT) cleaning. The first one applies a local and temporal window of radius R and duration T around an SLC hit rejecting the hit if no second one is found in that window. For the DeepCore filter, parameters R = 150 m and $T = 1 \mu$ s are used. In contrast, the seededRT cleaning takes a seed, most commonly the HLC hits fulfilling the RT criterion as above, and adds hits fulfilling the RT criterion around the seed. This method is iterated with the hit series becoming the next seed as long as more hits can be found by the algorithm. A schematic depiction of both algorithms can be seen in figure 4.7. As the cRT cleaning is softer compared to the sRT, it is used for veto purposes as it is able to identify background events better. The sRT cleaning is mostly used for reconstruction algorithms that rely on a dataset that is as pure as possible, as the algorithm allows fewer background events. The increased loss of signal events for the sRT cleaning is mostly acceptable because less significant hits are cut away first.

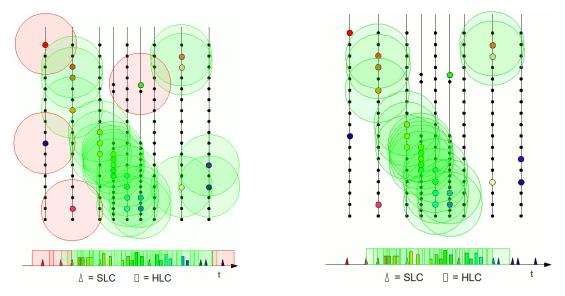


Figure 4.7: Classic (left) and seeded RT cleaning (right) concepts (taken from [92]). Kept hits are centered in green colored circles of radius *R*, explicitly discarded hits in red ones. Color coding is the same in the time axis. The higher strictness of the sRT cleaning becomes obvious regarding the hits in the bottom right corner of the scheme as they are discarded while the are kept by the cRT algorithm.

The *DeepCore filter* runs on SMT3 triggered HLC and sRT-cleaned SLC hits in the same fiducial volume as the SMT3 itself. The filter uses a three layer deep veto around this volume to reject down-going atmospheric muons. Therefore, the filter algorithm calculates a time corrected center of gravity (COG) of hits in the fiducial volume. By assuming that hits in the veto region are caused by direct photons of the passing particle, the speed of that particle can be determined relative to the center of gravity. If the particles speed is at 0.25 - 0.4 m/ns, which is close to the speed of a down-going muon passing the detector, then the hit is tagged VetoWindowHit. Events with more than one VetoWindowHit are excluded. The event rate after application of the DC filter is $\sim 15.5 \,\text{Hz}$ for 2012 [94]; a schematic description for a sample event can be seen in figure 4.8.

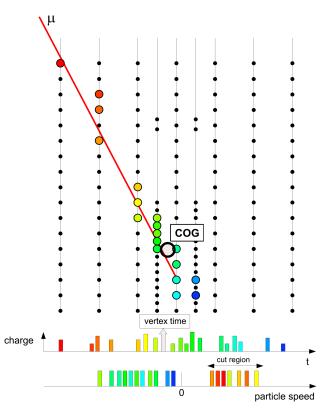


Figure 4.8: Schematic description of the DeepCore filter (taken from [93]) for the example of an incoming muon.

4.3.3 Transfer to the North

After filter application, the amount of data is sufficiently small to be transferred to the North via the *South Pole Archival and Data Exchange system (SPADE)* or its newly implemented successor *Java Archival and Data Exchange (JADE)*⁴⁵, where the data is stored on disks for further processing. If the amount of data is too large for the bandwidth available for satellite transfer, data can be stored on disks or tapes at the South Pole and shipped out in the Antarctic summer. The next step in the North is to add further reconstruction algorithms – building the so-called *offline level2* – that are more sophisticated and therefore need more than the available computation resources at ICL.

4.4 The Antarctic Ice

In order to determine the properties of the ice surrounding the strings in IceCube, so-called flasher runs are used. In those runs, photons are emitted by the LEDs on several DOMs and are received by others after propagation through the ice. The data used to determine the ice-models has been taken in the IC40 configuration by LEDs emitting light of 400 nm wavelength. In a complex Likelihood approach (for more details see [95]), a global fit to the recorded number of registered photons and their respective arrival times eventually leads to the most important parameters for modeling the ice: the scattering coefficient *b* and the absorption coefficient *a*. Commonly, for scattering the effective value $b_e = b \cdot (1 - \langle \cos(\theta) \rangle)$ is used. The inverse $\lambda_e = 1/b_e$ hereby determines the average distance between successive scatters weighted with the deflection angle θ , whereas $\lambda_a = 1/a$ determines the average distance before absorption in the ice.

The most current ice model *SPICE-Lea* (also *SPICE-\lambda_e a*), explicitly takes the effect of the ice anisotropy into account. This effect was observed as more light was measured in the direction of certain strings than on average from all other directions. As this effect has been seen for all DOMs on the emitting string and for all receiving strings, hole ice effects or cable shadowing were excluded as a reason, leaving the surrounding ice as the culprit. As the microscopic reason for the effects remain unknown, the effect has been taken into account in the fitting procedure by modifying the scattering function. The model is found to be in good agreement with the data [96]. The resulting coefficients for this ice model can be seen in figure 4.9 in comparison to the predecessor ice-model *SPICE-Mie*, named after the underlying theory of Mie scattering⁴⁶ that is implemented in the ice models. While the description is more accurate in the newer model, both models show prominent features of the Antarctic ice like the dust layers at ≈ 2050 m depth and the most clearest ice (low scattering, low absorption) in the regions from 2100 – 2450 m, where the lower part of the DeepCore subdetector has been deployed.

⁴⁵SPADE/JADE is also used for transferring supernova and HitSpooling data to the North.

⁴⁶The theory, named after the German physicist Gustav Adolf Feodor Wilhelm Ludwig Mie, describes the scattering of electromagnetic waves on a homogeneous sphere, whose diameter is of the same order as the radiation's wavelength.

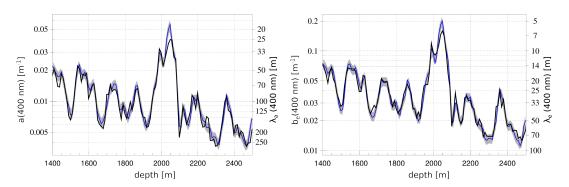


Figure 4.9: SpiceLea absorption (left) and effective scattering coefficients (right) against depth in comparison with the preceding ice-model SpiceMie (shown in purple) with gray SPICEMie error bands from [95]. The corresponding absorption and effective scattering length are shown on the right y-axes. Plots taken from [96] were slightly modified for better readability.

4.5 Signatures Recorded by IceCube

As shown in section 2.2, neutrino interactions depend on the respective neutrino energies. Therefore, also the observable event signatures depend on the respective energy regime. In the MeV-regime, only a collective increase in the dark noise rate can be observed if large numbers of neutrinos arrive at the detector, e.g. caused by a neutrino shock front from a SN. In the GeV regime, single neutrinos may be resolved, with different signatures depending on the neutrino flavor. In addition to signal-induced events, uncorrelated and correlated noise caused by various reasons is also observed in IceCube.

4.5.1 Event-like Signatures: Tracks and Cascades

Neutrino interactions in the GeV-regime and beyond, as listed in section 2.2, induce two main topologies in the IceCube detector: (*Muon-*) Tracks and Cascades. Tracks are thereby caused by ν_{μ} CC interactions, cascades in ν_{e} and ν_{τ} CC as well as in all NC interactions (see schematic events topologies in figure 4.10). For taus generated in ν_{τ} CC interactions, one faint track is observed as well as two cascades, one caused in the initial interaction and one by the decay of the tau. Because of this structure, such an event is called a *Double Bang*. Due to the τ decay length of 50 m/PeV, such events become distinguishable at energies > 1 PeV. At lower energies single DOMs are investigated in order to find double-peaked structures in the recorded waveform – so-called *Double Pulses* – that hint at tau neutrinos [97].

The typical muon track lengths are of O(km) which might exceed the detector's dimensions. The energy is either estimated by the length of the track, or – if it is not a fully contained track – by the deposited energy per distance $\langle dE/dx \rangle$. The median angular resolution for tracks is about 10° at 10 GeV and lower than 1° for energies > 100 GeV [98] (see section 5.2.2 for details on the algorithm). For cascades an estimation is much more difficult to achieve, as their signatures are almost spherical and contain little information about the lepton's original direction. However, using that bit of information, a median angular resolution of about 30° at energies of about 100 GeV was achieved by the estimator presented in section 5.2.5 [99].

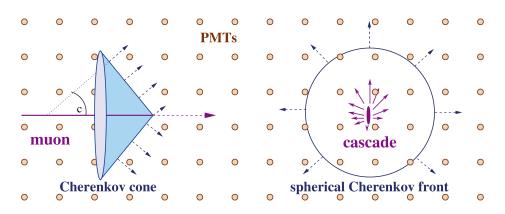


Figure 4.10: Simplified event schemes for tracks (left) and cascades (right). Yellow dots mark the position of the PMTs (taken from [100]).

The cascade's energy resolutions in IceCube are about 40% at 10 GeV and improve to roughly 10% at energies > 10 TeV [101] (see section 5.2.4 for the method used in this work). For tracks, however, the energy estimation is more complicated because of the possible energy losses outside the detector. The achieved resolution is about $0.4 - 0.2 \sigma_{\log_{10}(E_{\mu})}$ for energies of 1 TeV to 1 PeV [101].

Exemplary event displays for both topologies are shown in figure 4.11. The signatures in a rather high energy region can be recognized easily. However, the situation changes a lot in a low-energy event as cascade and track signatures become more and more similar and a clear identification gets difficult to impossible. A low-energy example is given at figure 4.12 with only limited distinction potential left.

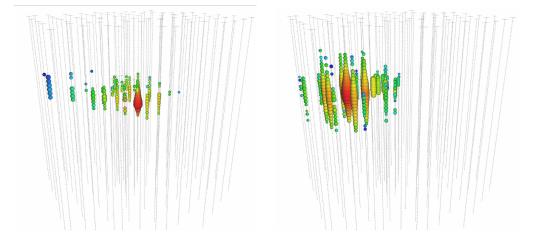


Figure 4.11: High energy track (left) and cascade (right) event display. The cascades deposited energy is 385^{+46}_{-49} TeV, the median angular resolution is ~ 13.5°. The track deposited $30.8^{+3.3}_{-3.5}$ TeV energy and it's median angular resolution is $\leq 1.2°$ [102]. Color coding ranges from early hits in red to late hits in blue.

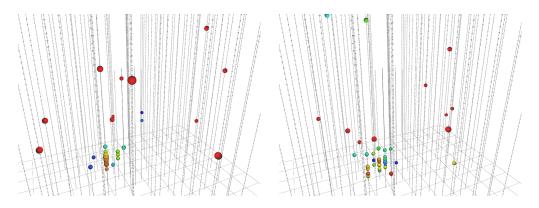


Figure 4.12: Low-energy track (left) and cascade (right) event displays. Both taken from simulation datasets used in this thesis (please refer to section 5.1 for further details). The primary electron neutrino energy is $E_{\nu_e} = 79.4 \text{ GeV}$ with 70.8 GeV carried by the cascade. The primary muon neutrino energy is $E_{\nu_{\mu}} = 75.7 \text{ GeV}$ and the track energy is $E_{\mu} = 42.7 \text{ GeV}$. Color coding ranges from early hits in red to late hits in blue.

4.5.2 Supernova Signatures: Collective Increase in the Dark Noise Rate

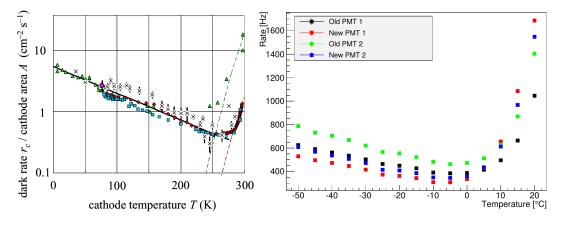
At mean neutrino energies of O(10 MeV), usually no more than one photon reaches one optical module preventing the observation of typical high-energy event signatures. However, as neutrinos from a supernova are expected to reach the detector in larger numbers due to the emitted shock front, also a large number of photons (depending on the model $10^5 - 10^6 \gamma \text{s}$ at 10 kpc distance [86]) is expected. The number of Cherenkov photons per positron is given by $N_{\gamma}(E_e) \approx 180 \text{ MeV}^{-1}$. This allows for a detection via the observation of a collective increase of the dark noise rate in the whole detector [103]. As simple events can not be reconstructed, the analysis has to rely on a statistical method for supernova detection, which is presented in chapter 6. Up to now, there is no energy resolution available yet, however, efforts are underway to gain energy information from HitSpooling datasets corresponding to a supernova candidate [104].

4.5.3 Noise Signatures

Both neutrino event and supernova signatures may be obscured by noise. In the first case, noise hits can lead to misreconstructions of the events or pure noise cay be misidentified as an event. Recent studies have shown that the noise measured in the ice can be divided into two parts: correlated and uncorrelated (thermal) noise (see figure 4.13).

Correlations in a standard analysis context only refers to correlations within one DOM caused mainly, but not exclusively, by radioactive decay induced luminescence in the PMT glass (e.g. investigated in [105], which also found that other not yet identified origins for correlated noise must exist). For standard IceCube PMTs, a minimum in the dark noise is reached at about -5° with correlated noise getting dominant for temperatures below that minimum.

In the case of investigating dark noise increases e.g. for supernova analyses, additional noise can change the significance of a possible signal candidate. In contradiction to the standard analysis context this is, however, caused by inter-DOM correlations due to atmospheric



muons. Their influence on the signal and a method to reduce that will be described in more detail in chapter 6.

Figure 4.13: *Left*: Dark noise rates for various PMTs (Hamamatsu R7725 (cathode area $A = 17 \text{ cm}^2$ in triangles for cooling and in squares/diamonds for cooling and subsequent reheating), Hamamatsu R5912 (crosses, $A = 335 \text{ cm}^2$) and an ETL 9357FLA (circle, $A = 430 \text{ cm}^2$)). Dashed green lines in left plot indicated the thermionic emission (plot taken from [106]).

Right: Dark noise rates for four Hamamatsu R5912 where "old" PMTs have standard IceCube DOM glass and "new" ones have a low-radioactivity PMT glass reducing contributions of ⁴⁰K and U/Th decay series by roughly 28 %. Plot taken from [105].

4.6 PINGU - A Possible Low-Energy Future of IceCube

A next step to further decrease the detection threshold for neutrinos even below 10 GeV is the *Precision IceCube Next Generation Upgrade (PINGU*, possibly realized as part of a larger upgrade *IceCube-Gen2* that would also contain high-energy extensions), which is planned to consist of more densely instrumented strings located around the center of DeepCore. As of now, various configurations of such a detector are under discussion; however, an enhancement in sensitivity is in general expected.

The detector's sensitivity, characterized by the effective volume for positrons per optical module $V_{\rm eff,e^+} = N/n_{\rm e^+}$, with N detected hits per module, increases from 583 m³ for Ice-Cube to 767 m³ for DeepCore to 912 m³ for a 20-string PINGU configuration. For supernova searches, this would yield an increase of the sensitivity to Galactic supernovae by roughly $\sqrt{2}$ using all three detectors combined. As a measure of sensitivity the significance⁴⁷ is displayed in figure 4.14 for the detection of an 8.8 M_{\odot} SN as function of its distance [107].

Event-based analyses can profit from the extended capabilities of particle identification at low energies as can be seen in figure 4.15.

⁴⁷The significance is defined as the deviation of the collective dark noise rate $\Delta \mu$, divided by its uncertainty $\sigma_{\Delta \mu}$. Please see section 6.3 for more details on its definition.

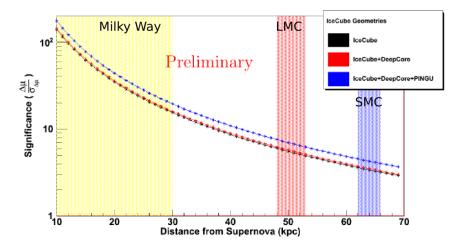


Figure 4.14: Significance versus distance for a Huedepohl SN model for IceCube only, IceCube/DeepCore and IceCube/DeepCore/PINGU where for the latter a 40-string configuration was used (plot taken from [107]). Color coded regions depict the Milky Way (yellow) and the Large (red) and Small (blue) Magellanic Cloud.

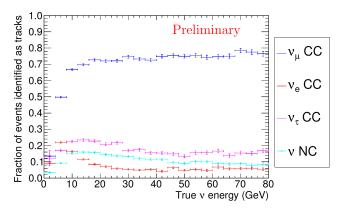


Figure 4.15: Particle identification in PINGU can correctly classify about 70% of all simulated ν_{μ} events as tracks at energies of more than 10 GeV and still about 50% at 5 GeV. The fraction of cascades that are misreconstructed as tracks varies from 10% to slightly more than 20% only (plot from [107]).

For an analysis searching for *Dark Matter*⁴⁸ from the galactic center it was found that not only PINGU's 1 yr sensitivity is slightly better than for the existing IC79 analysis, but also that PINGU can extend the search to lower dark matter candidate masses. GRB analysis would also benefit from such an improvement as neutrinos emitted according to the inelastic collision model lie in this energy range.

⁴⁸Dark Matter is matter, that does neither emit nor interact with light (hence: dark). Although it is not yet experimentally confirmed, there is a variety of evidence for its existence from various observation, e.g. from the motion of galaxies. Assuming the galaxies consisting only of SM matter, the virial theorem, stating $2\langle E_{kin}\rangle = -\langle E_{pot}\rangle$ with time-averaged kinetic and potential energies, is broken. In order to conserve it, the missing amount of gravitational energy is added by the introduction of additional non-observable matter.

SIMULATION AND RECONSTRUCTION

5.1 Simulation

Simulations in IceCube are used for both background estimation (e.g. in the case that no off-source region can be defined and that the background levels cannot be quantified from off-source data) and for the description of a possible signal. As for the data acquisition and the analysis methods, the simulations for GRB and supernova searches differ strongly. In the first case, event-based general purpose simulations are used, similar to most other IceCube analyses, in the second case two special-purpose frameworks provide the simulated data.

5.1.1 Event-based Simulation

The event-based simulation involves three distinct steps:

- The primary particles, e.g. charged leptons or hadronic cascades, and their interactions are simulated by so-called *Generators*. In order to adjust the simulated energy spectra to the assumed models, e.g. for atmospheric backgrounds or the investigated GRB signals, the events provided by the generator are weighted accordingly.
- Particle propagation through the Antarctic ice, including energy losses, is modeled by *Propagators*, which also delivers the resulting number of photons.
- *Detector simulations*, which exert detector effects on the simulated photons and provide the detector response, are added in the last step.

At the end of this chain, simulated events are organized in the same way as experimental data and can be processed with the same analysis tools.

5.1.1.1 Generators and Weighting

The *Cosmic Ray Simulation for Kaskade* software package (*CORSIKA*) simulates atmospheric particle showers from highly energetic cosmic rays [108], subsequently creating down-going atmospheric muons that reach the detector. For atmospheric neutrinos, the *Generates Events for Neutrino Interaction Experiments* software package (*GENIE*) [7] is used to provide atmospheric interaction cross-sections for electron and muon neutrinos as well as for a potential neutrino signal from GRBs.

For both generators, event weights w are calculated which are later used for the determination of the respective simulated event rates in the form of the overall weight sum. For atmospheric muons, the weights are calculated using a flux model from [109] and for atmospheric neutrinos by using the flux model from [110].

5.1.1.2 Propagators

The particles provided by the generators are then passed to the *clsim* module⁴⁹, which, depending on their type, either propagates the particles by itself or chooses another particle propagators, such as the *Propagator with optimal precision and optimized speed for all leptons* (*PROPOSAL*) or GEANT4⁵⁰. Particles in PROPOSAL are modeled from energies of 100 MeV to 10^{11} GeV and the code takes ionization losses, bremsstrahlung, photonuclear interactions, electron pair productions, muon/tauon decays, and Moliere scattering⁵¹ into account by using cross-section parametrizations. With lower energies, however, a parametrization is no longer possible because of precision losses. In this case, direct GEANT4 propagation is used instead. For the GENIE files used in this work, the threshold energies, below which parametrizations are not used, are E < 30 GeV for hadrons and E < 100 MeV for electrons and photons. After propagation of the particles by PROPOSAL or GEANT4, clsim determines the number of Cherenkov photons generated and propagates these by itself, until they either get absorbed or reach a DOM.

5.1.1.3 Detector simulation

If a photon is detected by a DOM, *Detector Simulation* will be performed for the events, that simulate the various detector effects taking place in the hit DOM. Thereby for each effect, such as noise, DOM electronics and triggering separate modules are available.

Vuvuzela [92] is a recently developed module that simulates uncorrelated and in contrast to its precursors also correlated noise (see noise description in section 4.5.3). The uncorrelated part is described by a Poissonian distribution

$$f_{\text{uncorr}}(x) = \frac{\lambda \Delta t^x}{x!} e^{-\lambda \Delta t} ,$$
 (5.1)

with the number of hits x, the rate parameter λ which is ~ 20 Hz for thermal noise and the interval length Δt . For correlated noise, the number of scintillation photoelectrons is modeled by

$$f_{\rm corr}(y) = \frac{\eta^{y}}{y!} e^{-\eta} \quad , \tag{5.2}$$

where η is determined by per-DOM fits to be about 10. The combined noise description is compared to data in figure 5.1 and clearly shows a better albeit not perfect description of detector data (taken from HitSpooling data) than its predecessor *Noise-Generator* that only provided uncorrelated noise hits.

PMT electronics effects, including prepulses, afterpulses and late pulses⁵², are simulated by the *PMTResponseSimulator* module, whereas the LC-logic and the digitization of the

⁴⁹Named after the *Open Computing Language* framework (*OpenCl*) that allows the usage of computing systems consisting of both CPUs and GPUs (central and graphics processing units, respectively). Clsim is accessible via https://github.com/claudiok/clsim.

⁵⁰GEANT4 is a software package for directly simulating the passage of particles through matter [111].

⁵¹Multiple scattering of a particle traversing a medium, named after German physicist Paul Friedrich Gaspard Gert Molière.

⁵²Prepulses are caused by photons hitting the first PMT dynode, afterpulses by ions that are created at farther dynodes and late pulses by backscattered photoelectrons [87].

waveforms is provided by the *DOMLauncher* module. The resulting launches are further processed by the *trigger-sim* module that only retains events that fulfill the trigger conditions used in the detector.

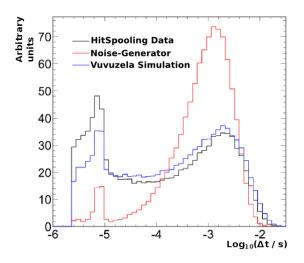


Figure 5.1: Comparison of the noise simulation by Noise-Generator and Vuvuzela with pre-trigger experimental data taken with the HitSpooling system (taken from [92], slightly modified for better readability).

5.1.2 SN Simulation

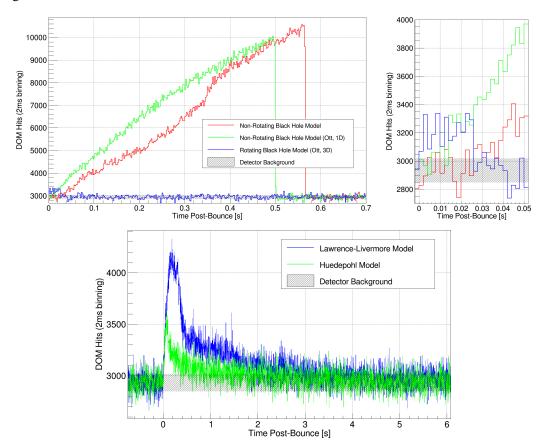
In IceCube two supernova simulations are used for complementary purposes: The framework *Unified Supernova Simulation Routine (USSR)* allows for fast simulations of the detector response to a variety of theoretical SN models and the full detector response tool *supernova simulation (snsim)* uses an event-based simulation chain to provide a complete set of hits in the modules.

USSR: The USSR provides an estimate for the detector response in a different way compared to the standard event-based simulations as it uses an effective volume, which is determined to $\overline{V_{e,eff}} \approx 600 \text{ m}^3$ for electrons/positrons detected by standard DOMs. The number of photons per DOM can be calculated to $N_{\gamma} = \epsilon \cdot n_{\nu} \cdot \overline{V_{e,eff}}$ with a deadtime correction factor ϵ depending on the dark noise rate and the neutrino density n_{ν} . The latter incorporates the differential neutrino flux parametrized as

$$\frac{\mathrm{d}\Phi}{\mathrm{d}E} = \frac{L_{\mathrm{SN}}(t)}{4\pi d^2 \overline{E}(t)} \cdot \left(\frac{1+\alpha(t)}{\overline{E}(t)}\right)^{(1+\alpha(t))} \cdot \frac{E^{\alpha(t)} \cdot \mathrm{e}^{-(1+\alpha(t))E/\overline{E}(t)}}{\Gamma(1+\alpha(t))} \quad , \tag{5.3}$$

which depends on the time-dependent spectral shape $\alpha(t)$, the neutrino luminosities L and energies E as well as the respective time-average $\overline{E(t)}$ [86].

The USSR provides detector responses to a variety of models, e.g. the models mentioned in section 3.2.2.4 (the Lawrence-Livermore model, the Huedepohl model and a non-rotating Black Hole model), recent 1D Black Hole models [112] with progenitor mass ranges from



12 to 120 M_{\odot} and rotating as well as non-rotating Black Hole 3D models from [113], that have been added to the USSR by [114]. A comparison of some of these models is shown in figure 5.2.

Figure 5.2: Total number of DOM hits for rotating and non-rotating $40 \,M_{\odot}$ Black Hole supernova models (top) and for the Huedepohl and Lawrence-Livermore models (bottom), all simulated at 10 kpc distance. The top right plot is a zoomed version of the top left one and shows the comparison between the models on the time scales of the rotating model. The shift of the models from [113] is caused by the assumption that the core bounce correlated with the time of insetting neutrino flux, which is not necessarily correct. However, for that reason, only the spectral shape and the amplitude should be looked at.

The neutrino spectra for a rotating Black Hole simulation – the most accurate description of a GRB-SN in the Collapsar model – are only available for durations up to ~ 36 ms after the core bounce. The resulting rates in this model are more difficult to distinguish from detector background at such early times. However, the rates are similar to the non-rotating model, which will be considered in this work instead. In comparison to the two lower-mass models depicted in figure 5.2, it becomes obvious that the IceCube detector is most sensitive to Black Hole forming SNe and, in consequence, also to GRB-SNe.

In this work, a correction of the detector rates has been implemented to remove the influence of atmospheric muons. The standard deviation of the detector rate underestimated the true one, as the broadening due to atmospheric muons and the non-Poissonian characteristics of the dark noise rate is not considered. The correction algorithm calculates the true standard deviation of the detector rate distribution as $\sigma = \sqrt{\overline{R}} \cdot f$, where $\sqrt{\overline{R}}$ is the mean detector rate and the broadening factor f was determined in [115] to ~ 1.71 for the IC79 detector configuration (the respective correction for the 86-string configuration will be implemented by the working group in the near future).

snsim: A detailed supernova simulation has been implemented in *snsim* [116] which provides a full detector response using elements of the standard event-based simulation chain. Neutrino interactions, e.g. such as the inverse beta decay and electron scatterings, are generated by an injection module for 1 - 100 MeV neutrinos. Their spectra may follow either a Gaussian distribution, a Gamma distribution – which is used as the spectral prediction in the Huedepohl model – or a flat spectrum. As in an event-based simulation, the neutrino-induced primaries in the ice are propagated by GEANT4 and the consequently emitted photons are passed to clsim. After this, detector simulation, including the PMTResponseSimulator and DOMLauncher modules, is added. Output from snsim is either provided in the default event based data stream format after passing DAQ simulation (trigger-sim) or in the SnDaq scaler format.

A comparative plot of snsim and USSR is shown in figure 5.3. The obvious deviation of 40 % is understood by now. A 3 % discrepancy was caused by a lower effective volume in the USSR and was corrected taking new ice models into account. A deviation of about 5 % was caused by incorrect cross-sections which is fixed by using an adjusted effective volume. The detector responses shown in figure 5.2 take both effects into account by using a 1.08 times higher effective volume. The remaining deviation of ~ 20 % arises from the neutrino spectra implemented in snsim and a 15 % effect is caused by missing scaler dead-times and different time definitions in snsim [117].

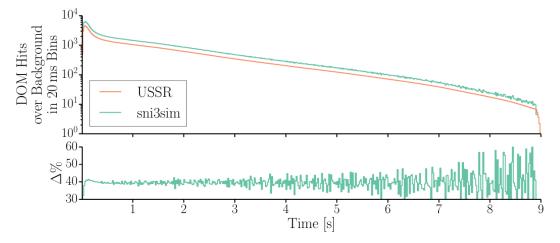


Figure 5.3: Comparison of the supernova simulation frameworks USSR and snsim in terms of DOM hits over background for a Huedepohl model SN at 10 kpc distance before correcting differences in the simulations (plot taken from [116]).

5.2 Reconstruction

For IceCube analyses, various reconstruction methods are used to determine the direction and the energy of simulated events or experimental data. The choice of those methods depends on the event shape (track or cascade) and on the available computational resources. Fast methods are used at early stages e.g. the *LineFit*, but more advanced algorithms can only be applied after a preselection reduced the amount of data drastically. In the following, the reconstructions used in this work as well as a method for estimating the event resolution are presented. The reconstruction of a collective dark noise rate increase for a SN search is presented in chapter 6.

5.2.1 LineFit/ImprovedLineFit

The *LineFit* (*LF*) algorithm is a reconstruction method supposing an infinite muon track which induces photon emission in straight paths. This fit provides a first-guess reconstruction only, as it does neither make any assumptions about the properties of the ice nor about the Cherenkov characteristics of the light emission. In this model, a photon that is emitted at the track's vertex \vec{x} and time *t* hits the ith of *N* hit DOMs at a time t_i . The LineFit finds the most probable track by minimizing the sum of squared distances

$$\min_{t,\vec{x},\vec{v}} \sum_{i=1}^{N} (\vec{x}_i - \vec{x} - \vec{v} \cdot (t_i - t))^2 \quad , \tag{5.4}$$

where $\vec{x_i}$ is the position of DOM *i* and \vec{v} the light speed along the track. This ansatz is based on the assumption that all hits occur locally near the muon.

In the *ImprovedLineFit* (*iLF*) the last assumption is dropped as outliers and scattered hits are taken into account. The latter are identified as such, if an earlier hit occurs within a defined region around the investigated hit, and then eliminated by a simple filter. Removal of outliers is realized by using a *Huber* fit method⁵³, that aims at finding the solution of

$$\min_{t,\vec{x},\vec{v}} \sum_{i=1}^{N} \phi(\rho) \quad , \tag{5.5}$$

where $\rho = \vec{x_i} - \vec{x} - \vec{v} \cdot (t_i - t)$ and $\phi(\rho)$ is the Huber penalty function

$$\phi(\rho) = \begin{cases} \rho^2 & \text{if } \rho < \mu, \\ \mu(2\rho - \mu) & \text{else} . \end{cases}$$
(5.6)

This function identifies hits as outliers if ρ is larger than a constant μ determined from simulations to 153 m [118]. After the optimization the known outliers are discarded and a regular least-square fit is performed on the cleaned dataset. The median angular resolution of the improved LineFit is better by almost 60 % when compared to the standard LineFit.

⁵³Named after the Swiss statistician Peter J. Huber.

5.2.2 SPE/ImprovedSPE/MPE

More advanced algorithms can take further information into account, such as the scattering, the absorption or the Cherenkov angle characteristics of the emitted photons. As those properties have a random character, the equations used in the reconstructions are no longer analytically solvable and the use of statistical methods becomes necessary. The methods chosen in this work are likelihood based reconstructions that provide an estimate for unknown parameters $\vec{\theta}$ by maximizing the likelihood function

$$\mathcal{L}(\vec{x}|\vec{\theta}) = \prod_{i} p(x_i|\vec{\theta}) \quad , \tag{5.7}$$

where the *probability density function (PDF)* $p(x_i | \vec{\theta})$ describes the probability to measure a response \vec{x} under the most likely track hypothesis $\vec{\theta}$. In IceCube, this hypothesis is usually described by the vertex position (x,y,z) and by the direction in terms of the zenith and azimuth angles θ and ϕ .

This ansatz is optimal in the sense that all hits are considered, however, in order to reduce CPU time consumption, only the first photon registered in each DOM is considered in the *single-photo-electron* (*SPE*) likelihood

$$\mathcal{L}_{\text{SPE}}(t_{\text{res}} | \vec{\theta}) = \prod_{i}^{\text{1st hits}} p(t_{\text{res},i} | \vec{\theta}) \quad , \tag{5.8}$$

where t_{res} is the time residual defined as the difference between the measured hit time t_{hit} and the geometrical time t_{geo} assuming an unscattered photon path.

The number n_i of hits in the ith DOM is considered in the *multi-photo-electron (MPE)* likelihood

$$\mathcal{L}_{\text{MPE}}(t_{\text{res}} | \vec{\theta}) = \prod_{i}^{\text{1st hits}} n_i \cdot p(t_{\text{res},i} | \vec{\theta}) \cdot \left(1 - \int_{-\infty}^{t_{\text{res}}} p(t | \vec{\theta}) dt \right)^T , \qquad (5.9)$$

and leads to a better resolution at energies > 10 TeV. For both the SPE and the MPE likelihood the *Pandel function*⁵⁴ [119] is commonly used as the PDF, defined as:

$$p(t_{\rm res} | \vec{\theta}) = e^{d/\lambda_a} \cdot \left(1 + \frac{\tau \cdot c}{\lambda_a}\right)^{d/\lambda} \cdot \frac{\tau^{-d/\lambda} \cdot t_{\rm res}^{d/\lambda - 1}}{\Gamma(d/\lambda)} \cdot e^{-t_{\rm res} \cdot (1/\tau + c/\lambda_a) - d/\lambda_a}$$
(5.10)

with the light speed c in ice, the distance d, the scattering and absorption lengths λ and λ_a and a free parameter τ determined from simulations to 557 ns [98]. Another possibility is to use tables generated with the *Photon Propagation Code (PPC)* [120] providing the number of expected photoelectrons from MC simulations depending on a DOM's location in the ice and its orientation towards the arriving photon. Those multidimensional tables are fitted with spline functions⁵⁵ by the *Photospline* module [121] to cover statistical fluctuation and provide a more condensed representation than the tables.

⁵⁴Named after the German physicist Dirk Pandel.

 $^{^{55}}$ Splines (of order *n*) are polynomial functions (of order *n*) that are commonly used for data fitting. Spline interpolation has the advantage of a small interpolation error and circumvents divergences by their piecewise definition.

The initial parameter set – the so-called seed – for the SPE likelihood is usually a LineFit result; the SPE fit result serves as a seed for the MPE algorithm. Using the improved LineFit as a seed for the SPE fit gives the *improved SPE fit (iSPE)* with an improvement in angular resolution of roughly 13 % compared to the standard fit [118].

It is also common to perform more than one iteration of the same fit with a varied seed to get an improved performance. Those are indicated as e.g. SPEx for an x-fold iterated SPE fit.

5.2.3 FiniteReco

The reconstruction algorithms described above only consider position, time and direction of the track and thereby assume that the track is of infinite length. In *FiniteReco (FR)*, this assumption is replaced by a track hypothesis with starting and stopping points as depicted in figure 5.4. In order to determine these points, FiniteReco uses an infinite track assumption as a seed and projects the hit DOMs onto the track under the Cherenkov angle, leaving the outermost projections as starting and stopping point. In the next step, also including non-hit DOMs, the likelihood ratio

$$\mathcal{L}_{\text{FR}} = \frac{\prod_{i} p_{i}(\text{no hit} | \text{infinite track})}{\prod_{i} p_{i}(\text{no hit} | \text{finite track})}$$
(5.11)

is maximized with the probability p_i (no hit | infinite track) to register no hit in DOM *i* assuming an infinite track and the probability p_i (no hit | finite track) to see no hit assuming a finite track [122]. These no-hit probabilities are calculated using the spline-reconstructed PPC tables. FiniteReco returns the resulting optimal reconstructed vertex position and stopping point as well as the track length *FRLength*.

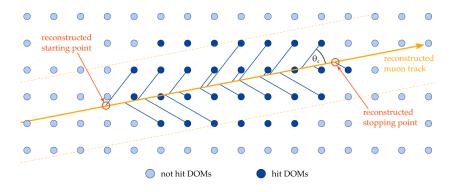


Figure 5.4: Track description by FiniteReco. In contrast to simpler reconstruction algorithms, a starting and stopping point of a track is estimated (plot taken from [122]).

5.2.4 Monopod/Millipede

The cascade reconstruction module *Monopod* estimates the energy as a result of maximizing the logarithm of a Poissonian⁵⁶ likelihood

$$\ln \mathcal{L} = k \ln (E\Lambda) - E\Lambda - \ln k! \quad , \tag{5.12}$$

⁵⁶Named after the French physicist and mathematician Siméon Denis Poisson.

for an energy loss *E*. The number of photons *k* is provided by spline-fitted PPC tables, Λ - the expected number of photons for a template electromagnetic cascade of 1 GeV - is determined from simulation as well [123]. Maximizing the likelihood with respect to energy and direction provides estimates for these quantities.

The reconstruction tool *Millipede* [101] uses the same method for tracks dividing a track into segments and running the Monopod likelihood on each segment *j*, eventually maximizing

$$\sum_{j} \ln \mathcal{L}_{j} = \sum_{j} k_{j} \ln \left(\vec{E} \cdot \vec{\Lambda} \right) - \sum_{j} \left(\vec{E} \cdot \vec{\Lambda} \right) - \sum_{j} \left(\ln k_{j} ! \right) \quad , \tag{5.13}$$

to obtain the best-fit result on \vec{E} .

5.2.5 The Resca Resolution Estimator

In order to determine the quality of the best-fit results provided by e.g. the Monopod reconstruction, resolution estimators are used. For tracks [124] as well as in the *resolution estimator for cascades (resca)* [99], Cramér-Rao based estimators⁵⁷ [125, 126] are used within IceCube exploiting the bound

$$(\operatorname{cov}^{-1}(\vec{\theta}))_{ij} \le F(\vec{\theta})_{ij} \tag{5.14}$$

with the covariance matrix cov of the considered parameters $\vec{\theta}$ and the Fisher information matrix⁵⁸ [127]

$$F_{ij} = -\left(\frac{\partial^2 \ln \mathcal{L}(\vec{\theta})}{\partial \theta_l \, \partial \theta_m}\right) \quad . \tag{5.15}$$

The diagonal elements of the covariance matrix, obtained by the evaluation of equations 5.14 and 5.15, are the square of the standard deviations of the individual variables. The so-derived zenith and azimuth uncertainties σ_{θ} and σ_{ϕ} , respectively, can be translated into a combined opening angle uncertainty

$$\sigma_{\Omega} = \sqrt{\sigma_{\theta}^2 + (\sigma_{\phi} \cdot \sin(\theta_{\text{reco}}))^2} \quad , \tag{5.16}$$

with the reconstructed best-fit angle θ_{reco} .

⁵⁷Named after the Swedish mathematician and statistician Harald Cramér and the Indian statistician Calyampudi Radhakrishna Rao.

⁵⁸Named after the British statistician and biologist Sir Ronald Aylmer Fisher.

SEARCH FOR GALACTIC GRB-SNE WITH THE SUPERNOVA DATA ACQUISITION SYSTEM

In the following chapter, the *Supernova Data Acquisition System* (*SnDaq*) and the efforts to improve the software and the data processing in various aspects will be outlined. In section 6.1, the details of the environment in which SnDaq is running – the *South Pole System SPS* – will be introduced. Thereafter the software stability, e.g. measured by SnDaq's uptime, as well as several testing and maintenance procedures are presented. The calculation of the significance indicating a possible SN detection is described in section 6.3 followed by a more detailed description of the alerts that are executed as function of a possible SN candidate's significance. An efficient muon subtraction algorithm improving these calculations is outlined in section 6.5. A summary of the installed software releases during the times the author of this work was (co-)responsible for SnDaq can be found in appendix A.

6.1 The South Pole System

At SPS three different servers are involved in various stages for SnDaq: the core server 2ndbuild, the control server expcont and the server access which is mainly used for installation.

2ndbuild - Main Component and Data Processing: The SnDaq main component – a framework consisting of several C++/ROOT⁵⁹ programs and classes – is executed on the 2ndbuild server. This core is surrounded by several control and data transfer scripts written in various languages such as Python, Perl and bash that are also running on this machine. The scaler data (called *raw data* in the following), described in section 4.2.2, is transferred by pDaq to 2ndbuild, where the continuously running SnDaq main component reads and processes the data. Thereby, it calculates a significance for the data as described in section 6.3 and eventually provides output in ROOT-formatted files. Depending on the significance of an investigated SN candidate, various sets of information are provided, e.g. data used for a fast supernovae analysis in the North [104] or information emails to different recipients (for more details about the different sets and the actions performed for high-significance alerts, see section 6.4).

⁵⁹The ROOT-software developed at CERN is commonly used for data analysis in a scientific context. It is implemented in C++ using the C++-interpreter CINT for versions below 6. CINT was replaced with Cling from version 6 onwards.

expcont - Monitoring and Controlling: Expcont is the host server for *I3Live*, a control and monitoring tool for most of the data acquisition systems and corresponding (sub-)systems (for more details about I3Live see [85]). SnDaq communicates with I3Live via the python software component *Live Supernova Daq* (*LSD*). The LSD component provides an interface from I3Live to SnDaq and vice versa, e.g. for mediating stop/start commands received by I3Live or SnDaq itself. It also continuously checks the status of SnDaq for additional information such as CPU and memory usage and forwards this information to I3Live which, in turn, displays them on IceCube internal webpages.

The monitoring is divided into several aspects depending on which quantities are to be monitored. A technical monitoring in I3Live already exists, however, an improved software, called moni2.0. is already partly implemented. The calculation of the variables needed for the SnDaq monitoring within moni2.0 was implemented in [104] and this work. Some of those quantities are calculated every ten minutes, e.g. the scaler hit rate per DOM, others at the end of each run such as e.g. the number of supernova candidates in this run. A more physics-related monitoring providing information about the significances and therefore about the relevance of a candidate is provided by dedicated SN-alert and SNEWS monitoring web pages. Future plans incorporate the migration of these webpages to I3Live.

SnDaq also continuously reports quantities that are used for monitoring to the LSD on 2ndbuild and to the control script *checkSnDaq.py* on expcont. The latter is a cronjob-triggered script, developed in this work, that checks SnDaq's status and is able to recover/restart SnDaq if an erroneous state is detected.

access - Installation: In order to install SnDaq on SPS or any other system that might be used e.g. for testing, a dedicated stand-alone installation script was implemented within this work. It executes all the necessary steps needed for staging the main component on a first-access server – called *sps-access* on SPS – and for deploying and starting SnDaq on a 2ndbuild(-like)⁶⁰ server.

6.2 System Stability, Testing and Maintenance

A particular focus in improving the data acquisition system within this work laid on increasing its stability against software crashes including e.g. segmentation violations. For this purpose, SnDaq new testing routines were explored that were used partly locally and partly on a dedicated server system that mirrors the SPS environment – the so-called *South Pole Testing System (SPTS,* for further information see [85]).

The South Pole Testing System: An important aspect to ensure a software's stability is to provide accurate testing mechanisms. Therefore SnDaq was changed in course of this work to not contain implementations that distinguish between the hosting servers – i.e. there is no coding difference on SPS and SPTS. This was almost fully accomplished except of an additional line in the email headers and bodies listing the system's hostname. After achieving independence of the software from the system, SPTS can be used to test almost every step in

⁶⁰Within this work, the installation of SnDaq on spare servers for 2ndbuild, like the *pdaq2* server, was implemented and successfully tested.

the data processing. Additionally it provides the possibility to check the software's compatibility towards future releases of external dependencies such as ZeroMQ3⁶¹ and the upcoming ROOT version 6. The latter will switch from the CINT interpreter to *Cling*. Compilation and execution of SnDaq using the latter was tested successfully on SPTS.

Testing Data and Methods: Testing data for SnDaq on SPTS is categorized into two kinds of datasets, being either regular data (including calibration runs) to test regular behavior or data taken that explicitly shows faulty behavior used to investigate specific problems. Regular data provides C0-testing⁶² capabilities for SnDaq, C1-capability, however, could only partly be achieved.

A necessary step towards C0-testing, that was tested within this work, is the usage of the socalled *replay runs* provided by pDaq on SPTS. In such testing runs data from a single 8 hr run taken at SPS is processed by a replay code which updates the data, so that it always appears to be live on SPTS. The data that pDaq generates in the usual format can then be picked up by SnDaq the same way as on SPS. Additionally pDaq sends also the information needed by the muon subtraction (see section 6.5) via ZMQ. Therefore this testing routine has the advantage that it includes the file and data handling before and after SnDaq processing into the testing cycle. A full 24 hr testing in replay-run mode was successfully executed within this work with no problems observed in the data-taking. This testing method was later-on required to be a standard testing procedure for new SnDaq releases. For future improvement, the HitSpooling system will also be integrated, so that the full SnDaq processing structure can be tested.

Valgrind: For investigating SnDaq's stability concerning memory and CPU consumption as well as searching for possibly hidden memory leaks, a series of tests using the Valgrind⁶³ framework were performed within this work. The results of this testing lead to several bug-fixing releases increasing the system stability by removing most potential memory leaks, except for those caused by external software like ZMQ and the ROOT software⁶⁴. The full output of the testing can be found in appendix B.

SnDaq Uptime: As a result of the tests mentioned above, the current SnDaq uptime is now stably at roughly 99.7 % around-the-clock (see table 6.1 and figure 6.1) with no major software issues like memory leaks or segmentation violations reported in 2016.

The minimal SnDaq downtime is given by pDaq and within this mainly by scaler buffers overflowing in the first seconds of a new run leading to a restart after reading in first data. This led to a downtime of $\approx 2 \text{ min per run before May 2015}$. With the introduction of the

 $^{^{61}} Version 3 of the ZeroMQ framework, a messaging library, online accessible on http://zeromq.org/.$

⁶²C0 testing means statement coverage, here used in the sense that the full processing of SnDaq was tested for a particular dataset. C1 testing means branch coverage which means that every possible branch is tested, e.g. in if-or statements. Datasets containing irregular data are helpful here, however, SnDaq is not yet fully C1-tested.

⁶³Valgrind is an instrumentation framework for building dynamic analysis tools. The software provides tools "that can automatically detect many memory management and threading bugs, and profile your programs in

detail" (for more information see http://valgrind.org/).

⁶⁴Valgrind provides options to suppress warning about memory leaks in the code due to external dependencies such as e.g. ROOT.

pDaq version Lake_Louie, this was fixed and, in addition continuous runs were implemented, increasing pDaq's own uptime. SnDaq's minimal downtime, in consequence, reduced by roughly a factor two to about 0.1 % (see figure 6.1b). The goal of achieving uptimes of 99 % was passed in 2015, reaching uptimes of close to 100 %.

Table 6.1: Uptime statistics for SnDaq for each season. Data is shown from 2012-01-01 up to 2016-09-07, covering the times in which the author was responsible for the SnDaq.

season	data shown	clean uptime (excl. short runs)
2012	full year	97.49%
2013	full year	98.23%
2014	full year	98.34%
2015	full year	99.51%
2016	01-01 till 09-07	99.71%

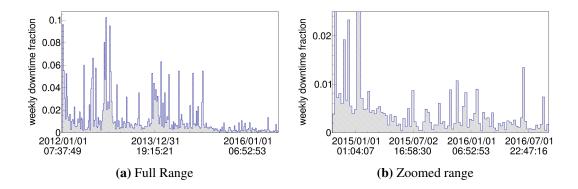


Figure 6.1: SnDaq weekly downtime fraction in the time frame of this thesis. Data is shown from 2012-01-01 to 2016-09-07, covering the times in which the author was responsible for SnDaq. The left plot shows the full range; the plot on the right zooms into the last months to illustrate the reduction of baseline downtime due to introduction of continuous runs which were introduced in May 2015 with pDaq version Lake_Louie.

6.3 Significance Calculation

The scaler data described in section 4.2.2, that are provided in an asynchronous 1.6384 ms binning, are read by SnDaq and processed further. For synchronization, the data is rebinned into a global 2 ms array. However, as the amount of data in this fine binning is rather large, those datasets will only be read out for high-significance candidates (see section 6.4). After synchronization, a second rebinning into 500 ms slices is performed. This interval serves as the main analysis binning and as building element for the other analysis binnings of 1.5 s, 4 s and 10 s. The three latter are realized by overlapping sliding averages that are moved every 500 ms. The 0.5 s binning was chosen to investigate short neutrino bursts, e.g. from Black

Hole forming supernova. The interval of 1.5 s is used for investigation of intermediately long neutrino bursts as e.g. predicted by the Lawrence-Livermore model. The 4 s binning reflects the time-constant of a exponentially decreasing flux from a proton-neutron star cooling phase of about 3.8 s [86]; the 10 s binning was chosen, as the duration of SN1987A is of the same time-scale. In an efficiency study, the 1.5 s analysis was found to have the highest sensitivity to supernovae in the Galaxy for current models [128].

For each bin an analysis is performed evaluating the likelihood function

$$\mathscr{L} = \prod_{i=1}^{N_{\text{DOM}}} \frac{1}{\sqrt{2\pi\sigma_i}} \cdot \exp\left(-\frac{(r_i - (\mu_i + \epsilon_i \Delta \mu))^2}{2\sigma_i^2}\right) \quad , \tag{6.1}$$

with individual rates r_i for each DOM out of the number of active DOMs N_{DOM} in the investigated 500 ms binning. The mean values μ_i and their respective standard deviations σ_i are taken from the sidebands depicted in figure 6.2. As the analysis window size is fixed to 500 ms and an exclusion zone interval of 29.5 s is reserved, the sidebands cover 570 s⁶⁵.

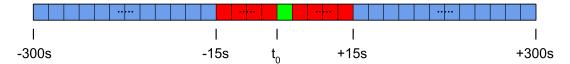


Figure 6.2: SnDaq analysis scheme. Shown are the 500 ms analysis window in green, the exclusion zones in red and the sidebands in blue. For the 1.5, 4 and 10 s binnings, the analysis window is larger, while the sidebands become smaller by the the respective amount.

Each DOM has a module-specific quantum efficiency ϵ_i (for the complete listing of highquantum efficiency modules, see table 4.2). In this work, the 1.35 higher efficiencies for all high-QE DOMs were taken into account as a first step. The accurate values of the efficiencies on a DOM-by-DOM basis study are planned to be included by the working group in the future.

Minimizing $-\ln(\mathcal{L})$ yields the dark noise rate deviation

$$\Delta \mu = \underbrace{\left(\sum_{i=1}^{N_{\text{DOM}}} \frac{\epsilon_i^2}{\sigma_i^2}\right)^{-1}}_{\sigma_{\Delta \mu}^2} \cdot \left(\sum_{i=1}^{N_{\text{DOM}}} \frac{\epsilon_i^2(r_i - \mu_i)}{\sigma_i^2}\right) \quad , \tag{6.2}$$

with the respective standard deviation $\sigma_{\Delta\mu}$. For characterizing SN candidates, the significance ξ is introduced as

$$\xi \coloneqq \frac{\Delta \mu}{\sigma_{\Delta \mu}} \quad . \tag{6.3}$$

In the case of pure Poissonian noise, the significance distribution can be described – according to the central limit theorem – by a Gaussian distribution centered at $\xi = 0$ with a standard deviation of $\sigma_{\xi} = 1$. The probability of a significance below a threshold s is then $p_{\xi < s} = s \cdot \sigma_{\xi}$.

⁶⁵Those number are valid for the 500 ms analysis only. For rebinned analyses, rebin factors apply.

However, as correlations between the DOMs, introduced by after pulses or atmospheric muons, invalidate the assumption of Poissonian noise, the equations have to be recalculated by regarding a dark noise rate deviation of

$$\Delta \mu = \underbrace{\left(\sum_{i,j=1}^{N_{\text{DOM}}} C_{ij}^{-1}\right)^{-1}}_{\sigma_{\Delta \mu}^{2}} \cdot \left(\sum_{i,j=1}^{N_{\text{DOM}}} C_{ij}^{-1}(r_{i} - \mu_{i})\right) \quad .$$
(6.4)

In this equation, the inverse covariance matrix is given in a two-DOM calculation by

$$C_{ij}^{-1} = \frac{1}{\sigma_x^2 (1 - \rho^2)} \cdot \begin{pmatrix} 1 & -\rho \\ -\rho & 1 \end{pmatrix}$$

where σ_x is the same standard deviation for both DOMs and the correlation coefficients ρ are assumed to be positive for simplicity.

The corrected significance – if the correlation coefficients are known – can be calculated in the N_{DOM} case to $\xi_{\text{corr}} = \xi/\sqrt{1+\rho}$ (for the detailed calculation, see appendix A in [115]). However, as such an analysis requires the knowledge of all $N_{\text{DOM}} = 5160$ coefficients, that can in principle change over time, as well as the calculation of the 5160x5160 matrix at least once per run⁶⁶, this approach was discarded. A more practical solution to reduce the influence of atmospheric muons will be presented in section 6.5.

6.4 Alert Handling

In the case that SnDaq calculates a significance crossing a given threshold – a so-called alert – various actions are triggered, e.g the sending of information into the North or requests of further data from other (sub-)systems. The respective thresholds are given by an OR combination of a limit on the significance ξ calculated as shown in section 6.3 with a limit on the significance ξ' , for which the atmospheric muon correction has been applied (for details about the correction method please see section 6.5).

The muon subtraction itself is triggered at $\xi > 4.0$ and a first alert information is send to I3Live. For the combination $\xi > 7 || \xi' > 4.4$ a couple of interactions are triggered: an alert datagram will be send to the *snnet* server as well as an email to the working groups, and the lightcurve is forwarded to I3Live. The header and body of the email to the working group depends on the significance as well, taking 3 different stages of information from a normal level to silver and gold alerts. The corresponding actions are summarized in figure 6.3. Table 6.2 displays the actions performed if either ξ or the muon corrected significance ξ' is larger than the given threshold. Additionally, the relative amount of alerts after muon correction and the respective rates are given.

⁶⁶The quality of this calculation increases with a recalculation on shorter timescales, which, consequently, implies a more time-consuming correction.

action	$\xi >$	$\xi' >$	$N_{\rm alerts}^{\rm corr}/N_{\rm alerts}^{\rm total}$	<i>R</i> _{alerts}
Subtract atmospheric muons	4.0	-n.c	-n.c	-n.c
Save the full analysis window in 2 ms resolution into the .root file	6.00	4.00	-n.c	-n.c
Send alert information to I3Live	4.00	-n.c	-n.c	-n.c
Request HS data for the alert window	8.40	5.80	7/7	1.2 / 14 d
Send text message to working group members	8.50	6.00	3/3	0.5 / 14 d
Gold trigger	10.00	10.00	no detect	no detect
Export 2 ms data for fast analysis	8.20	7.30	10/13	2.2 / 14 d
Send alert to snnet	7.00	4.40	414/476	1.9 / 8 hr
Forward alert to SNEWS	8.40	5.80	7/7	1.2 / 14 d
Send mail to the working group	7.00	4.40	414/476	1.9 / 8 hr
Forward lightcurve to I3Live	7.00	4.40	414/476	1.9 / 8 hr

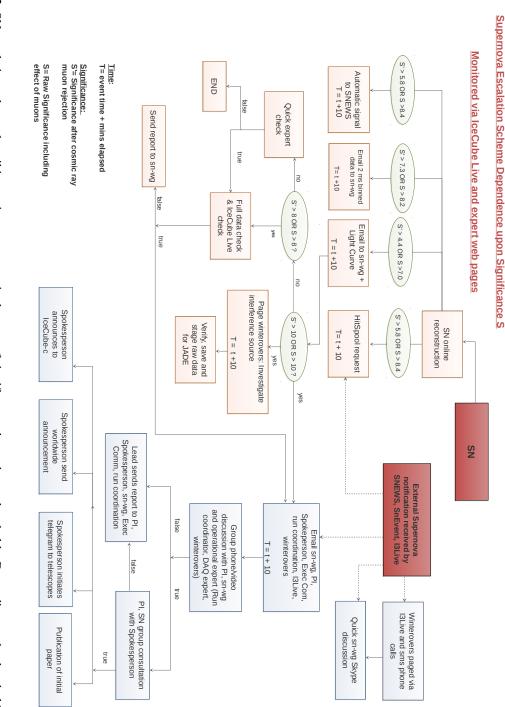
Table 6.2: SnDaq Alert actions at significance threshold crossing. For the gold trigger, there is no sufficient statistics to calculate $N_{\text{alerts}}^{\text{corr}}/N_{\text{alerts}}^{\text{total}}$ and R_{alerts} . However, for some actions – marked with "-n.c.-" for "not calculated" – , it is not required to calculate those values.

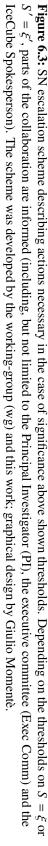
The optimization yielding the thresholds for the muon corrected significances will be described in section 6.5. The actions are executed in the same order as shown in the table except that the request for HitSpooling data is requested at the earliest possible stage if the uncorrected significance crosses its threshold. Due to the importance to have these data, it is requested first, i.e. before the muon subtraction.

Of particular importance is the email to the *snnet* server, which is then forwarded to the SNEWS (SuperNova Early Warning System) system. IceCube has been part of this network since 2005, together with six other experiments, namely Super-K, LVD, Kamland, Borexino, DayaBay and Halo. The purpose of SNEWS is to report coincident alerts between the experiments pointing towards a SN to a greater community of amateur astronomers, as they can determine the optical lightcurve with an enormous field of view. In order to involve further experiments, a collaboration with the AMON network⁶⁷ [129] and the gravitational wave community is envisioned [130, 131].

Besides actions triggering other sub-systems as the collection of HS data, the sending of datagrams to the SNEWS network, and the sending of 2ms data for a fast analysis described in more detail in [104], the most important means to spread significant alerts within the IceCube collaboration is the email send out to the working group. In the case of high-significance alerts, further actions are performed to inform the IceCube community. As this should not be done by software alone, an escalation scheme was developed (see figure 6.3 for details).

⁶⁷The Astrophysical Multimessenger Observatory Network (AMON) aims at combing cosmic ray, photon, gravitational wave and neutrino detection experiments into a multimessenger analysis with enhanced sensitivity. Collaborating experiments are i.a. IceCube, Fermi, Swift and the gravitational wave detector LIGO.





For example in the case of a so-called "Gold trigger" the winter-over personnel is notified to investigate any possible interfering sources, and to abstain from executing planned special runs e.g. for calibration and/or testing runs. Furthermore, instructions on how to backup and send data from a 48 hr buffer into the North are send. The email recipients list is extended to technical and scientific staff in order to coordinate further discussion leading either to public announcements if the alert was found to be real or discarding if not.

6.5 Implementation of an Efficient, Robust and Realtime Atmospheric Muon Subtraction

As outlined in section 6.3, the significance distribution deviates from the Poissonian expectation because of the influence of correlations. In order to reduce correlations within one DOM, a deadtime of 250 μ s was introduced while a different method has to be chosen for DOM-to-DOM correlations, as caused by atmospheric muons. To quantify the effect of a muon subtraction, the number of cosmic ray muon induced hits was simulated in [128]. A hit-based subtraction therein shows a gain in signal-background separation power especially for low significances caused by faint or distant SNe (see figure 6.4). Although the effect is stronger for low-flux models, e.g. for the Huedepohl model, a subtraction is in general beneficial for all assumed models.

It can be seen that significances of $\xi > 8.7$ caused by Black Hole-forming supernovae can be detected at distances of up to about 200 kpc assuming a specific radial distribution model for supernova progenitors in the Milky Way [132]. The data taken over three years from April 2008 to May 2011 with IceCube is shown compared with simulations in figure 6.5 following the same radial distribution model. In order to be conservative, those simulations use an 8 % lower effective volume than the best ice models and cross-sections currently predict.

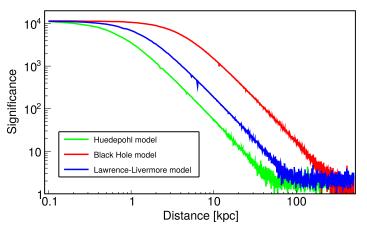


Figure 6.4: Simulated significances as function of distance between the Earth and the progenitor star (taken from [103]).

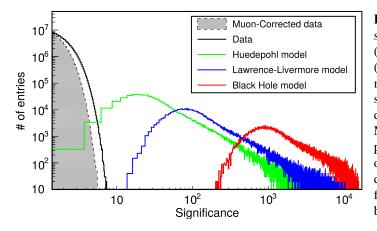


Figure 6.5: Experimental significance distribution without (black dashed line) and with (gray filled area) atmospheric muon subtraction. The simulated significances follow the radial distribution model [132] for the Milky Way. Only for the lightest progenitor mass model, an overlap with the experimental data is observed. Plot taken from [133] (slightly modified for better readability).

In context of a search for GRB-SNe, the aim of this work was to improve the visibility of Black Hole forming SNe in the Milky Way and the Magellanic Clouds.

6.5.1 The Subtraction Method

The basic method for a muon subtraction was developed and successfully tested in [115]. From the obvious correlation (see 6.6) between the significance and the SMT8 rate one can infer a correctional algorithm that fits a linear function between an estimate of the muon hit rate R_{μ}^{hit} and the significance ξ and calculates a corrected significance as

$$\xi' = \xi - b \cdot R_{\mu} - a \quad , \tag{6.5}$$

taking the fitting function's offset *a* and slope *b* into account. The result of such a subtraction can be seen in figure 6.6. The candidate triggering the muon subtraction has a significance $\xi = 6.03$ that gets corrected to about $\xi' = 3.7$.

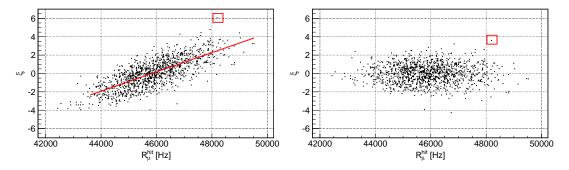


Figure 6.6: Significance as function of SMT8 hit rate before (*left*) and after (*right*) application of the correction method. The candidate triggering the according SNEWS alert is marked by the red box. The fit function to the correlation is shown as red line.

Other considered methods, such as using HitSpooling data or correcting the raw data before SnDaq processing, are too resource-consuming and unstable and were discarded even though they could in principle provide more accurate results.

The testing in [115] was performed offline with online-processed SnDaq data and corresponding muon data which was provided by the processing and filtering system PnF. The muon hit rate in this case was taken as the integrated hit rate from each global trigger that contains an SMT8 trigger (for details about the trigger, see section 4.3.1). However, as this data was only available after a couple of days, the method was not suitable for correction of e.g. SNEWS alerts as this has to be done essentially in realtime. Therefore part of this work was to identify possible ways to provide muon data to SnDaq at SPS, to port the method to an online realtime correction, increase it's robustness and to test whether the realtime-character of the analysis can be preserved.

Considering the choice on estimates of atmospheric muons, the fastest option turned out to be the usage of a first-guess estimate in the form of the SMT8 trigger, which can be provided by pDaq even before the application of any filter by PnF. From this perspective, pDaq muon data is the only estimate that is usable for an atmospheric muon subtraction without sacrificing SnDaq's real-time characteristics⁶⁸. The choice of the SMT8 trigger is not optimal as its energy threshold of 550 GeV is higher than the 400 GeV IceCube threshold. However, an attempt to use a trigger with a lower threshold as the volume trigger had no significant effect on the performance of the here presented method either individually or in combination with the SMT8 trigger [116].

To increase the robustness of the method and to limit the range of fitting to reasonably high SMT8 rates⁶⁹ a rate limit r_{thresh} was implemented in a robust way⁷⁰ as

$$r_{\text{thresh}} = \text{median}(r) - 3 \cdot \text{mad}(r)$$
 . (6.6)

Therein, the median absolute derivative mad(r), given by

$$\operatorname{mad}(r) = \operatorname{median}\left(\left|r_i - \operatorname{median}(r)\right|\right) , \qquad (6.7)$$

is used for a set r of individual rates r_i . A minimal threshold of $\xi \le -10$ was introduced to prevent SnDaq's negative significance fall-back values to enter the calculations.

6.5.2 Muon Corrected Significance Thresholds

After muon subtraction, the thresholds for alert handling can be reconsidered. Following the results of a recent study, limits of $\xi' = 5.6$ for sending alerts to SNEWS and $\xi' = 4.2$ for sending alerts to the working group were implemented. SNEWS alerts are then expected to happen every 20 days respecting the required maximum number of high-significance alerts of "no more than one per week" [134]. The chosen thresholds within this work are more stringent, respecting an increased limit of no more than one per 10 days⁷¹. At these thresholds, 77 % of a signal emitted by a supernova in the Large Magellanic Clouds are conserved [135]. In comparison to the 12 % achieved without the subtraction [136], the method increases the sensitivity by roughly a factor of six.

In the following paragraphs, the efforts to check, which alert rate is technically feasible conserving the realtime character of SnDaq, are discussed.

⁶⁸SnDaq on SPTS was about 2.7 times faster than realtime before introduction of the muon subtraction, see section 6.5.2.

⁶⁹Too low rates can be caused i.a. by removed strings or DOMs in pDaq data.

⁷⁰The less sensitive a statistical measure is towards outliers, the more robust it is. Median and median absolute derivate are robust, while e.g. the arithmetic mean and the standard deviation are not.

⁷¹Such a limit is internally already used in order to accommodate the inclusion of more experiments.

Processing Speed Checks: In order to check how long SnDaq needs to process the data as function of the alert thresholds, the dataset for run 119468 from 2012 was reprocessed on SPTS⁷². I3Live reports⁷³ this run to be of 8:00:23 hrs length and fulfilling all good-run list criteria [137]. SnDaq online processed data, however, were available for 7.63 hrs = 27485 s in two parts: The shorter set "A" covers 5160 s and the second set "B" comprises 22325 s of data. Several alerts are included in that dataset: Two alerts with $\xi > 6.0$ in the small dataset and four alerts with $\xi > 6.0$ in the larger part. The according pDaq trigger data for 8 hrs was simulated assuming that hits occur every 5 µs, corresponding to the SMT8 trigger rate of roughly 2 kHz. The number of hit channels is thereby represented by using Gaussian-distributed random variables with a mean value of $\mu = 12$ and a standard deviation of $\sigma = 2$ which is consistent with observed values in corresponding PnF files. The number of hits is therefore of the same order of magnitude as in real data, however, as only the processing speed is of interest for this test, the number does not have to reflect reality.

The results of the test runs are summarized in table 6.3. Shown first is the duration of a baseline run determining the processing speed with a muon subtraction for each $\xi > 6.0$ fluctuation. As baseline run it reflects the case of no muon subtraction as six calls to perform a subtraction in 8 hrs is a negligible overhead. In the next run, the subtraction is applied for each alert crossing the $\xi = 4.0$ threshold, which yields in total 226 method calls. This causes a processing speed decrease of about 30 %. However, SnDaq is still about two times faster than realtime. The last run is performed to investigate the runtime increase that is caused by the additional writing of candidate summaries to the files with disabled muon subtraction and a threshold of $\xi > 4.0$. As expected processing takes longer than in the baseline run but the main decrease in speed is caused by the subtraction method itself. The additional writing, however, raises the data size of the output files from 247 Mb to 641 Mb for the small dataset and from 3.8 Gb to 16 G for the larger dataset⁷⁴. As long as SnDaq is the only running system on 2ndbuild this is considered to be unproblematic.

Run	Set	$\Delta t_{\rm proc}$ [s]	$\Delta t_{\rm data} / \Delta t_{\rm proc}$	calls to μ-subtr. (per min)
baseline (mean of 3 runs, subtr. at $\xi > 6.0$)	A	1903 ± 8	2.71 ± 0.01	2 (0.06)
	B	8026 ± 72	2.79 ± 0.03	4 (0.03)
low threshold (mean of 4 runs, subtr. at $\xi > 4.0$)	A	2751 ± 125	1.88 ± 0.09	44 (0.96)
	B	11685 ± 1016	1.92 ± 0.16	182 (0.93)
writing only (1 run, subtr. at $\xi > 4.0$)	A B	2186 9039	2.36 2.47	

Table 6.3: Processing statistics for testing runs on SPTS. Shown is the processing duration Δt_{proc} and the time Δt_{data} over which the data was taken.

⁷²Processing of the data on SPTS was done with a Beer_Trooper9 release.

⁷³As taken from https://live.icecube.wisc.edu/run/119468/ as of April 6th, 2017

⁷⁴The increase in the file size is larger for dataset A as it contains more candidates per time than the dataset B.

6.5.3 Performance of the Atmospheric Muon Subtraction

After the release deployment, an increase in CPU consumption from 33 % to 44 % as well as a slight increase in memory usage from roughly 18 % to about 20 % was observed. This is uncritical for the 2ndbuild server. Most important for the realtime character is, however, that there is no notable increase in latency⁷⁵ due to the muon subtraction method. In the optimal case, the latency is constant, with the exception of new runs starting which requires some initialization. Increasing latency hints towards a processing speed slower than a realtime data taking. As can be seen in figure 6.7, the mean latency increases only slightly from 438.4 s to 444.3 s which is a minor effect of 1.3 %, and, most importantly, stays constant over time.

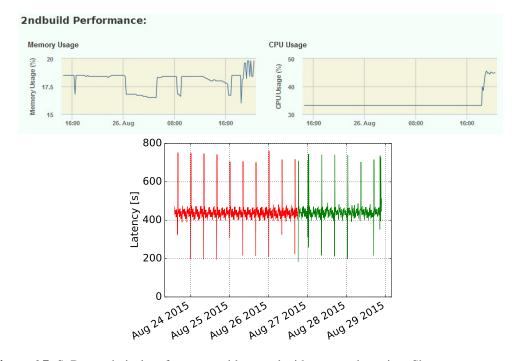


Figure 6.7: SnDaq technical performance without and with muon subtraction. Shown are memory consumption (*upper left*), CPU consumption (*upper right*) and latency (*bottom*). All three quantities show increases after switching to muon subtraction. The obvious peaks in the latency are expected as they are caused by run starts. The upper plot is a screenshot from the technical SnDaq monitoring pages [138]. The data for the bottom plot were also taken from that page.

Starting with the SnDaq version Beer_Trooper9, the alerts were adjusted from a purely uncorrected alert handling to combined alert handling as described in section 6.4. As the muon subtraction is only called for a SN candidate with $\xi > 4.0$, a complete significance distribution with and without subtraction does not exist. However, it is possible to show a distribution of all significances that are above the *snnet*-threshold without and with muon subtraction applied (see figure 6.8). The duration of the investigated period, considering an uptime of 99.69 %, is about 577.43 days⁷⁶.

⁷⁵Latency is the time between the raw data time and the time at which SnDaq processes the data.

⁷⁶Seven large but clearly erroneous alerts have been removed from the data sample. Underlying reasons for those are either missing pDaq trigger data for the muon correction or more than 1000 inactive DOMs.

It is possible to estimate the performance of the subtraction from the number of original significances in the Gaussian tails of the distributions shown in figure 6.8. The ratio of this number over the total number of investigated bins is equivalent to the probability for a significance to be larger than the respective thresholds. Such a probability can be further translated into the standard deviation σ of the according Gaussian distribution centered at mean μ by evaluating the normal inverse function

$$x = F^{-1}(p | \mu, \sigma) = \{x : F(x | \mu, \sigma) = p\} \quad .$$
(6.8)

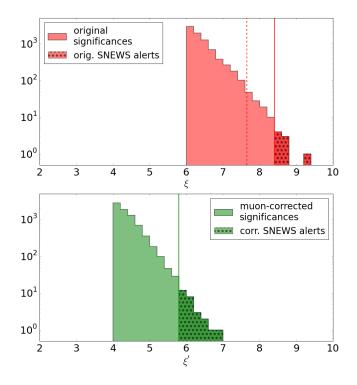


Figure 6.8: Gaussian tails of the significance distributions for all analyses without (top) and with (bottom) application of the muon correction. The distributions start at the respective thresholds for alerts to be send to *snnet*: $\xi > 6.0$ for the uncorrected and $\xi' > 4.0$ for the corrected significances. Alerts that are forwarded to SNEWS respecting the new thresholds are found to the right of the accordingly colored solid lines in the star-filled parts. The former threshold of $\xi > 7.65$ is marked by a red dashed line.

In this formula *p* is the probability

$$p(Z \le z) = \int_{-\infty}^{z} \frac{1}{\sqrt{2\pi}} \exp\left(\frac{-t^{2}}{2}\right) dt \quad ,$$
 (6.9)

where z is the so-called z-score given as $z = (x-\mu)/\sigma$. As there is no closed solution for equation 6.9, the integration has to be computed numerically⁷⁷ to determine the z-scores. The standard deviations σ_{ξ} and $\sigma_{\xi'}$ can then be evaluated as ratio of the z-score over the respective threshold.

This method is only valid if the alerts can be uniquely assigned to one of the four analyses. However, SnDaq only provides the highest alert in the respective analysis for each bin, which means that less significant alerts in the other analyses are hidden. Therefore, the number of alerts, if counted as described, is only the minimal number for each analysis. As it is not possible to say whether alerts in other analyses were overshadowed or not, the maximal

⁷⁷In this work, the SciPy package [139] was used for the numerical evaluation of equation 6.9.

numbers are also calculated, assuming all alerts in the other binnings hide an alert in the investigated analysis. The resulting maximal count is therefore naturally the same for all analyses. Both minimal and maximal values are listed in table 6.4 along with the z-scores, standard deviations and the correction factors $\sigma_{\xi}/\sigma_{\xi'}$. The latter are rather similar for the various analyses which indicates that the method is working consistently.

It is also evident that the muon subtraction yields a corrected significance distributions whose width is rather close to the Poissonian expectation of $\sigma_{\xi} = 1$. The remaining deviation from this is only about 3 - 5% which can be attributed to afterpulses [115] and undetected atmospheric muons. The improvement achieved by the realtime correction method is in agreement with the expectations from the offline implementation and from simulation [115, 128].

Table 6.4: Significance distribution parameters before and after muon subtraction for all alerts send to snnet since installation of the online muon subtraction. The total number of investigated bins $N_{\text{tot}} = 9.98 \cdot 10^7$ corresponds to the period of 577.43 days.

Binning [s]	$N_{\xi>6}$	$N_{\xi'>4}$	$z_{\xi=6}$	$z_{\xi'=4}$	σ_{ξ}	$\sigma_{\xi'}$	$\frac{\sigma_{\xi}}{\sigma_{\xi'}}$
(min/max)	$(N_{\xi>6}/N_{\rm tot}[10^{-5}])$	$(N_{\xi'>4}/N_{\rm tot}[10^{-5}])$					2
0.5 (min)	2506 (2.51)	2099 (2.10)	4.05	4.10	1.48	0.98	1.52
1.5 (min)	2072 (2.08)	1968 (1.97)	4.10	4.11	1.46	0.97	1.48
4 (min)	1619 (1.62)	1571 (1.57)	4.16	4.16	1.44	0.96	1.56
10 (min)	1749 (1.75)	1821 (1.82)	4.14	4.13	1.45	0.97	1.50
all (max)	7946 (7.96)	7459 (7.48)	3.78	3.79	1.59	1.05	1.51

6.6 Upper Limits for Black Hole Forming SNe Detection

In context of a search for Black Hole forming SNe that provide candidates for SNe-GRBs following the theory described in section 3.2, the SnDaq significances over the last years were investigated. The period of data regarded for this search ranges from 2012-01-01 00:00:01 to 2017-03-29 19:57:24. The uptimes until 2016-09-07 can be found in table 6.1. The uptime for the remaining data was measured to be 99.72 %, yielding a total search window of T = 5.18 yrs.

A significance threshold for a possible candidate will be set according to figure 6.9. This figure shows the fraction of events below a certain significance cut for simulations distributed following the radial star distribution of the Galaxy by [132]. Using this, one can derive that a threshold of $\xi = 10$ would be sufficient to allow essentially 100 % of Black Hole forming SNe to be detected.

As can be seen in figure 6.10, no event was found in the investigated data exceeding the threshold of $\xi = 10$. Therefore as result of this search, an upper limit can be set to the number of galactic Black Hole supernovae using the Feldman-Cousins approach [140].

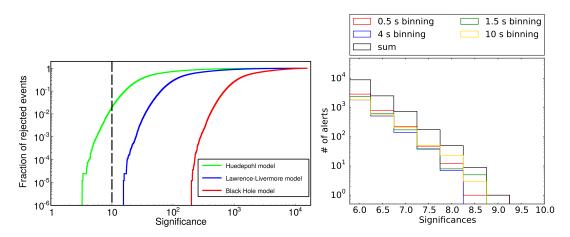


Figure 6.9: Fraction of rejected events as function of the respective significance threshold. The significance threshold of $\xi \le 10$ for the Black Hole SNe is marked by the red dashed line. Plot taken from [133] (slightly modified for readability).

Figure 6.10: Number of significances $\xi > 6.0$ displayed as sum and individually for the four binned analyses run in parallel.

The upper limit was chosen to be given for this work within a confidence interval of 90% (i.e. at 90% C.L.). This means that in 90% of all repetitions of the limit estimation, the given upper limit is obtained. The upper limit using this approach is determined to

$$N^{90\% \text{ C.L.}}/\text{yr} = N_{\text{FC}}^{90\% \text{ C.L.}}(n_b, n_{\text{obs}})/\varepsilon_{\text{det}}/T$$
 , (6.10)

with the number of observed significances n_{obs} , the number of significances expected from background n_b and the detection efficiency ε_{det} , estimated from figure 6.9 as 1 for the Black Hole model. With zero observed events with significances $\xi \le 10$ and zero events with $\xi \le 10$ expected for the background, the respective Feldman-Cousins limit is given by $N_{FC}^{90\% \text{ C.L.}}(0,0) = 1.33$, so that

$$N^{90\% \text{ C.L.}}/\text{yr} = 0.47 \text{ yr}^{-1}$$
 (6.11)

This upper limit on the number of Black Hole forming SNe in our Galaxy is a factor two better than the latest published upper limit [141]. In the case that in the next years no galactic supernova is detected, the collected statistics is expected to further improve this limit. Assuming that the background will continue to be negligible, the upper limit will scale linearly with the inverse of the measurement time.

6.6.1 Systematic Effects

Systematic effects have to be taken into account as simulated events are used. Uncertainties arise from the effective volume assumed in the simulation, the neutrino interactions in Earth matter and the detector volume, mass induced neutrino oscillations as well as from the underlying supernova model and the respective *Equation of State (EoS)*. As the simulations shown in this chapter assume a normal neutrino hierarchy and a hard equation of state, these settings reflect the benchmark scenario in the following discussion.

The detector related systematic uncertainties are dominated by the effect of the effective volume which was estimated to about 13% in [5, 141], combining a 7.4% effect caused by scattering and absorption in the Antarctic ice, a 10% uncertainty on the photosensor sensitivity and a 5% effect of the positron track length [133]. However, as explained in 5.1, the effective volume is underestimated in the simulations by 8%. The systematic uncertainty caused by the artificial deadtime of $250 \mu s$ accounts to 3% [133].

Neutrino oscillations in the Earth matter are not considered by the simulation software. This yields another systematic effect of about -8% as quoted by [142] for the default Lawrence-Livermore model. As normal hierarchy is assumed in above plots the relative systematic effect towards this is about $\pm 25\%$ depending on the oscillation scenario [86]. The neutrino cross-sections of the described processes account to 1% for both inverse beta decay and scattering on electrons and to 20% for reactions with oxygen in the Black Hole model⁷⁸.

The assumed equation of state introduces a model uncertainty that also has to be considered. Using the hard EoS [143] as benchmark, the softer one [144] yields 50 % lower significances. However, recent observation of high neutronstar masses of about $2 M_{\odot}$ [145] can exclude soft equations of state if the resulting maximal neutronstar mass is too low. The respective masses derived using the hard EoS are roughly $2.2 M_{\odot}$ but only $1.62 M_{\odot}$ using the soft EoS [146]. Following this and the consideration that also more massive neutronstars may exist [147], a harder EoS is usually favored (see e.g. [148]). For this work, however, the soft EoS will be considered to provide a limit on the minimal significance.

Taking the square root of the sum over the quadratures of the individual uncertainties yields an overall systematic uncertainty of $^{+35.6}_{-61.4}$ %. Consequently, this yields a shift of the minimal significance simulated for the Black Hole model from $\xi = 120$ as taken in figure 6.9 to significances of about $\xi = 45$. However, as this does not affect the choice of the threshold of $\xi = 10$, the upper limit remains the same as in equation 6.11.

⁷⁸The cross-section uncertainty for reactions with oxygen is with 3 % significantly smaller for the Huedepohl model.

SEARCH FOR LOW-ENERGETIC NEUTRINOS FROM COLLISIONALLY HEATED GAMMA RAY BURSTS

Low-energy neutrinos that are emitted from GRBs in the inelastic collision model described in section 3.1 have been proposed to produce an observable signal within the DeepCore subdetector. The exploratory search presented here investigates the possibilities of detecting such a signal in one year of data taken with the IceCube detector. As the high gamma-luminous GRB130427A was observed in 2013, the analysis was performed for the IceCube data taking season IC86-II that includes the observed gamma ray emission for this GRB. It should be noted that GRB130427A is associated with SN2013cq [149] and therefore is an interesting candidate for this work in the context of a search for a supernova-GRB connection.

The experimental data as well as the atmospheric background and signal simulation datasets are presented in section 7.1. The experimental dataset at the starting point of this analysis is dominated by atmospheric backgrounds, mostly muons. In order to reduce those backgrounds, events are further processed only if they fulfill the selection criteria described in section 7.2. This initial event selection reduces the amount of data so far that it becomes possible to perform the likelihood analysis presented in section 7.3. In the same section, the final event selection step, which is based on a likelihood analysis, is performed and condenses the remaining data to the final sample. Systematic uncertainties originating from e.g. detector effects and neutrino properties are discussed in section 7.4. This section also presents the final results of this analysis. A guiding scheme associating the various stages of this analysis to the sections is shown in figure 7.1.

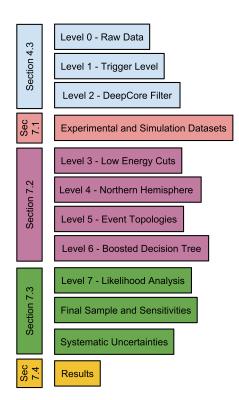


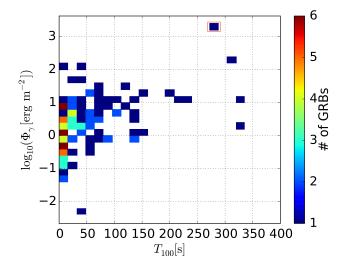
Figure 7.1: Analysis scheme

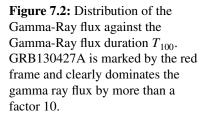
7.1 Experimental and Simulated Datasets

The data used in this work can be divided into three different classes. The first one comprises experimental GRB data, which are provided by several satellite missions and summarized in GRBWeb (see section 3.1.3). The second class contains experimental data from the IceCube detector and the third class consists of background and signal simulation events. Those data classes are described in sequence in the following paragraphs.

Experimental Data – GRB Selection: In an exploratory analysis, it is good practice to aim for an as low as possible background. For this reason, the northern hemisphere was chosen as the region of interest, which shows lower background rates, as the Earth serves as a shielding material against atmospheric muons. Therefore, GRBs originating from this hemisphere were selected from the GRB catalog for the IC86-II season. Only GRBs at times of good IceCube data-taking are used (for details on the definition of good data-taking, see the next paragraph), which leads to a sample that contains 123 GRBs. A list summarizing their most important parameters can be found in appendix C.

For the choice of analysis strategy, it is important to know the nature of the sources and properties such as the duration⁷⁹ and strength of the emitted gamma flux. A 2D histogram of the duration T_{100} and the gamma flux for the sources investigated in this work is shown in figure 7.2. GRB130427A – marked in the figure by a red box – clearly dominates the sample as its gamma-ray flux of almost 2 erg/cm² is about a factor 800 larger than the median flux of the other GRBs and a factor 10 larger than the second highest flux. Its duration $T_{100} = 274.55 \text{ s}$ – not including the afterglow duration – makes GRB130427A the third-longest GRB in the sample. For details about GRB130427A see the side note at the end of this paragraph.





Based on the quantities discussed above, stacked likelihood analyses investigating different emission spectra models as well as a single-source likelihood analysis investigating the highly gamma-luminous GRB130427A more closely are conducted.

⁷⁹The GRBs duration is given as T_x , the time in which the observing satellite experiments report x% of a GRB's gamma emission. In this work T_{100} is used which is the most inclusive duration.

<mark>6</mark> GRB130427A

A side note

The exceptionally bright GRB130427A was detected by the Fermi-GBM and -LAT subsystems as well as by the Swift-BAT telescopes [150, 151] at about 07:47:06 UTC on April 27th, 2013. The *CARMA* millimeter-wave observatory^{*a*} determined the bursts origin to 173.1367 °r.a., 27.6989 °dec (J2000). Reference [150] reports that "[...] GRB130427A had the largest fluence, highest-energy photon (95 GeV), longest gamma-ray duration (20 hrs), and one of the largest isotropic energy releases ever observed from a GRB".

The GRB has caused large interest in the scientific community. Publications include a study of the energy spectra showing various features that put stress on existing models and make it challenging to explain all the features simultaneously [153]. The afterglow characteristics are discussed in [154] and the possibility of GRB130427A being powered by a Magnetar is investigated in [155].

^aThe Combined Array for Research in Millimeter Astronomy (CARMA) interferometer combines 23 radio telescopes to an interferometer [152].

Experimental Data – Off-time Sample: The experimental data available for this IC86-II analysis is divided into 1,188 runs⁸⁰ covering a period from May 15^{th} , 2012 (first run is # 120156) to May 2^{nd} , 2013 (last run is # 122276). The initial sample contains three earlier test runs that were removed (Runs # 120028, 120029 and 120030). In a first step to improve data quality, only runs that are listed as "Good Runs" in the so-called *Goodrunlist* are selected. The criteria defined in this list for a run to be "good" are documented in [137] and i.a. require a minimal runtime of 10 mins and the absence of light in the detector, that is e.g. caused by calibration flasher runs.

The data quality is further improved by using only runs that are longer than 2 hrs as shorter runs might indicate problems. Finally, runs containing strings with more than 25 % inactive DOMs are discarded, as the veto capabilities used on various stages of the event selection will suffer from an incomplete detector. In total 171 runs were excluded. Thereof, two are non-good runs, 66 are runs with a large number of inactive DOMs per string and 103 are short runs. The lifetime of the remaining datasets in the sample is 325.4 days.

In general, analyses in IceCube have to follow the *blindness* concept, which requires the analysis to be developed on background and signal simulation and not on the complete – possibly signal-containing – data. This guarantees that there is no (un-)intentional enhancement of the signal by the event selection. In this analysis, background is taken from data, which has to be signal-free to respect blindness. In context of a GRB search, this is achieved by splitting the data into an on-time and an off-time sample. For the off-time sample, the GRB windows that potentially contain signal events under the assumption of coincident neutrino and gamma emission are excluded. The respective window size chosen in this work is $[\pm 2 \text{ hrs}]$ around the GRBs' T_{100} . The lifetime of the off-time sample is roughly 307 days, which leaves 18.4 days for the on-time sample. The latter is only looked into after the complete event-selection and likelihood analysis were developed and finalized. The event rates of the off-time dataset is

⁸⁰Usually a *run* corresponds to the data taken over a period of 8 hrs, however, shorter runs can be caused by deliberate intervention or problems occurring during the data taking.

shown in figure 7.3. The influence of atmospheric muons is clearly observable, however, in contradiction to the supernova data acquisition system (see chapter 6), the influence of atmospheric muons is corrected intrinsically by the event selection and the likelihood algorithm and not by a dedicated correction method.

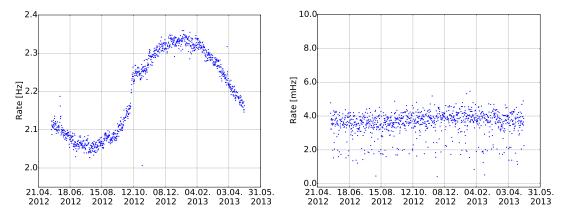


Figure 7.3: Experimental off-time data event rates on an early (left) and a late (right) event selection level (for event selection details, see section 7.2). As can be clearly seen, the effect of seasonal variations becomes negligible at later event selection stages. The x-axis scale starts on April 21st, 2012 and ends on May 31st, 2013.

Simulation Datasets: For the background simulation, CORSIKA datasets are used for atmospheric muons and GENIE datasets are used for atmospheric neutrinos (for details about the generation of IceCube simulation see section 5.1). All simulation datasets are produced using the newest noise description provided by Vuvuzela, the newest IceModel SPICE- $\lambda_e a$ and the newest DOM simulation provided by DomLauncher (for details see section 5.2). For both background and signal neutrino simulation, the same electron and muon neutrino datasets are used, however, with a different weighting.

As the analysis presented in this chapter is focusing on the low-energy DeepCore extension, GENIE datasets for signal simulation are used in an energy range of 3 - 1000 GeV. The background simulation events are weighted according to atmospheric spectra as explained in section 5.2 and the signal simulation is weighted according to the respective model. For both cases, the original GENIE weights, that only incorporate detector effects, are multiplied with a respective flux assumption.

As a flux of GRB neutrinos coming from the northern hemisphere is subject to Earth neutrino matter oscillations, oscillation effects have to be taken into account, e.g. using the *NuCraft* package [156]. In this work, NuCraft's default spherical Earth model, the PREM (Preliminary Reference Earth Model [157]), and the respective mass density values were selected. The oscillated flux for a neutrino flavor $i = v_e, v_u, v_\tau$ is given by

$$\Phi_i(E,\theta)^{\text{osc}} = \sum_{j=\nu_e,\nu_\mu,\nu_\tau} p_{ij}(E,\theta) \cdot \Phi_j^{\text{unosc}}$$
(7.1)

with the NuCraft neutrino mixing probabilities $p_{ij}(E,\theta)$ depending on energy E and zenith angle θ , and the unoscillated fluxes Φ_j^{unosc} .

As the flavor ratio expected at Earth is (1:1:1) (see section 2.3), this equation simplifies to

$$\Phi_i(E,\theta)^{\text{osc}} = \Phi^{\text{unosc}} \cdot \sum_{j=\nu_e,\nu_u,\nu_\tau} p_{ij}(E,\theta) \quad .$$
(7.2)

It turns out that, in the relevant energy range, neutrino oscillations only contribute with a one per mil effect for some weights, mostly less. This effect is even smaller for the summed rates, as individual weights may partly cancel out each other. Therefore neutrino oscillations are negligible for this analysis. However, for reasons of completeness, they will be taken into account in this work as described above.

The unoscillated part of the flux which is multiplied with the detector weight, is described by $\Phi^{\text{unosc}} = E^{-2} \cdot f(E)$ with a spline fitted function f(E) for the respective spectrum in figure 3.5. The flux can also be weighted following a simpler and more generic flux, e.g. $\Phi^{\text{unosc}} = E^{-2}$, that can be used to compare the performance of this work to the performance of other analyses. The signal datasets generated by reweighting and the respective analyses are named according to the underlying spectrum: " E^{-2} ", "(Γ)600", "(Γ)100" and "(Γ)100npc" for a $\Gamma = 100$ spectrum with an additional neutron-proton-converter component. For the single source search, the inelastic model with the highest expected neutrino flux is used, which is also reflected in the name "(Γ)600single".

7.2 Initial Event Selection

The event selection presented here mainly aims at reducing the predominant amount of atmospheric background in both experimental and simulated data to a small enough rate that can be handled by the likelihood analysis. "Initial" refers to the steps performed before the likelihood analysis; the final event selection stage presented later uses the likelihood algorithm itself. As the event selection relies on more and more complicated algorithms to reduce the amount of data, a step-wise approach is chosen. Thereby simpler and resource-friendly algorithms can be used on early levels, while resource-intensive algorithms are employed at later stages.

After passing the level1 and level2 steps, as described in section 4.3.2, the data are transferred to the North, where further processing takes place. The event selection up to level6 aims at reducing the atmospheric muon background and tailors the resulting dataset to the purpose of this analysis. This includes the DeepCore filter stream on level2, as a low-energetic neutrino search in particular profits from the low-energy extension DeepCore. The next step is the lowE-level3 selection which introduces cuts that provide a low-energy sample. As this work restricts itself to GRBs from the northern hemisphere, the so-called *level4* step cuts against events originating from the southern hemisphere. Eventually, the *level5* step takes event topologies into account. The steps on levels 4 and 5 are shared with the event selections presented in [122] and [99].

On this low-energy, northern hemisphere dataset, more specialized and advanced event reconstructions are processed to generate the required input parameters that are passed to a machine-learning algorithm – in this work a so-called *Boosted Decision Tree* (BDT) – which will be described in more detail below. This BDT provides a score for each event classifying it as a signal-like and a background-like event. A rather weak cut on this score builds the event selection *level6*, yielding a sample with a reduced background rate such that it is suitable for the likelihood mechanism. The choice of discrimination variables as well as the setting of the BDT training parameters follows reference [99]. To summarize the initial event selection, the achieved efficiencies for the different samples and the respective rates on level6 are shown in section 7.2.5.

7.2.1 LowE-Level3

The so-called *lowE-level3* is defined by all events passing the *lowE level3 script* which is available for each data taking season (see e.g. [158] for the 2013 version). As the GENIE simulation datasets were chosen to be as new as possible and origin from 2013 instead of 2012, like the off-time data, the lowE-L3 script is different for both sets. However, the change is of minor nature and only affects one cut variable⁸¹. After adjusting the scripts, to guarantee consistency, the modified version was made available to the collaboration. All cuts implemented on this level are described in the following list. The order of the listing reflects the ordering of their application.

NoiseEngine: The *NoiseEngine* module [92] removes noise pulses from the InIcePulses series by dividing the pulse series into multiple time windows of same length. All possible pairs of hits within one of these windows are tested whether they show more signal-like or more noise-like signatures by calculating the pair's zenith angle θ and azimuth angle ϕ . If a clustering in θ and ϕ in a *HEALPix* (*Hierarchical Equal Area isoLatitude Pixelization*)⁸² binned map is observed with more than three entries in at least one bin, the hit series is considered to be more signal-like and passes the NoiseEngine.

MicroCountHits & MicroCountPE: In order to suppress noise hits, a dynamic time window of 300 ns around every DeepCore hit is defined, which is moved around the hit to maximize the number of further hits within the window. As the assumption is that non-noise hits with temporal coincidence cluster in this window, the event is kept, if the window contains at least two pulses. The cut also requires more than 2 PE of deposited charge in the window.

NAbove200: Events with a charge of 12 PE or more in the region above -200 m in *z*-direction occurring prior to the trigger time are discarded in order to reduce the number of down-going muons.

VertexGuessZ: To further penalize down-going muons, the *z*-component of the first hit in an sRT-cleaned pulse map is used as an estimate of the full event's *z*-vertex. If this variable is larger or equal than -120 m, the event is kept.

TotalChargeFiducial/ChargeRatio: Events build from the sRT-cleaned pulse series have to deposit charge in the DeepCore fiducial volume to pass the cut. Additionally, events are excluded if their totally deposited charge is larger or equal to 1.5 times the charge in the DeepCore fiducial volume.

⁸¹The change affects the cut variable *RTVetoSeries250PE*; more details can be found in the respective paragraph. ⁸²HEALPix is a method to pixelize the 2-sphere, see e.g. [159].

DCFilterPulses_VetoPE: Uncleaned events with a charge larger than 7 PE in the veto region – again the region outside the DeepCore fiducial volume – are discarded to reduce the influence of atmospheric muons.

RTVetoSeries250PE: For this cut, hits from cRT-cleaned pulses in the veto region are sorted into two-dimensional clusters using a radius of 250 m and a time window of 1 μ s. If the largest cluster in the veto region – defined as described above – contains at least 4 PE, the event is discarded to reduce the rate of background events. As mentioned before, this cut is further refined in the 2013 lowE-Level3 script. However, for consistency, it is used in this form for all datasets.

C2QR6: This cut is based on the ratio of charge deposited in the first 600 ns of the event over the total deposited charge. Events with a value higher than 0.4 are kept. Through-going muons show lower values because their charge is deposited over a longer path. The cut is performed on the sRT hit map with the first two hits removed in order to avoid noise hit contributions.

BSummary: An event is kept, if

- NoiseEngine is passed,
- MicroCountHits > 2, MicroCountPE > 2 PE
- NAbove200 < 12 PE, VertexGuessZ < -120 m,
- TotalChargeFiducial > 0, ChargeRatio < 1.5,
- DCFilterPulses_VetoPE < 7 PE, RTVetoSeries250PE < 4 PE and C2QR6 > 0.4.

The respective rates for all datasets on level3 are shown in table 7.1. Please note that the signal simulation rates are scaled to make them comparable to simulated background rates. Therefore, the simulated signal rates are normalized to the expected number of events on the last event selection stage for the respective spectrum. In this and all other tables and plots in this section, only the distributions and rates for a $\Gamma600$ spectrum are shown exemplarily. Tables and plots for the remaining investigated spectra can be found in appendix D if not mentioned otherwise.

Level	off-time data [mHz]		atm. ν _µ [mHz]		
L3		 	$\begin{array}{r} 12.05 \\ \pm \ 0.01 \end{array}$	 	

Table 7.1: Rates on event selection level3. Signal rates are shown for the Γ 600 spectrum. The rates for the remaining spectra can be found in appendix D.

7.2.2 Level4

The cuts implemented on this level on the one hand aim at removing events that can not be processed by the later-on executed event reconstruction algorithms, as they contain too few hits. The minimum amount of hits required by e.g. the Monopod and Millipede reconstruction is six, as they take six parameters into account for the fitting – namely the three vertex parameters, the direction given in zenith and azimuth angle and the energy. The influence of the cut $nCh(sRT) \ge 6$ on the various datasets is shown in figure 7.4.

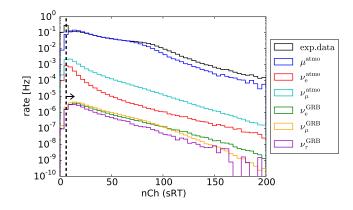


Figure 7.4: nCh(sRT) distribution on level3. The arrow points to the region where events pass the level4 cut. GRB signal rates – arbitrarily scaled – are shown exemplarily for the Γ 600 spectrum.

On the other hand, as this work focuses on the northern hemisphere, events reconstructed to origin from the southern hemisphere are cut out at this stage. However, as the quality of the reconstructions used here (an SPE fit with two iterations and the LineFit, both described in section 5.2) is not as advanced as reconstructions on later levels, the cut is chosen to be rather soft. Instead of setting the horizon as a limit, events that are slightly above the horizon – with $\cos(\theta) < 0.2$ – also pass. The conditions that have to be met by the events are $\cos(\theta_{\text{LF}}) < 0.2$ and $\cos(\theta_{\text{SPE2}}) < 0.2$. The respective distributions are shown in figure 7.5 and demonstrate a large separation potential between the atmospheric muon background and the signal, which is also reflected in the cut efficiencies that are summarized in table 7.2.

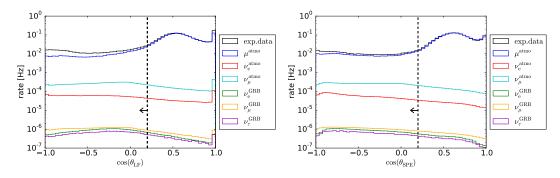


Figure 7.5: Reconstructed zenith angle distribution on level3: *left*: $\cos(\theta_{LF})$, *right*: $\cos(\theta_{SPE2})$. The arrow points to the region where events pass the level4 cut. GRB signal rates – arbitrarily scaled – are shown for the $\Gamma600$ spectrum.

Table 7.2: Event selection level3 to level4 efficiencies. Signal efficiencies are shown for the Γ 600 spectrum.

Levels	off-time data [%]		atm. ν_{μ} [%]		
L4/L3		49.12 ±0.07	47.82 ±0.04	49.8 ±0.4	51 ±3

7.2.3 Level5

The cuts implemented on this level are more refined than the previous ones and can take different hit topologies into account. The main target of the cuts is to reduce the influence of atmospheric muons and noise hits. The variables used on this stage are introduced in the following paragraphs.

Velocity Ratio: This topological cut parameter was developed in the context of a search for low-energetic neutrinos originating from dark matter [99]. First, events with less than two HLC pulses are excluded. The ratio v_{12}/v_{13} is the ratio of the velocities $v_{1j} = d_{1j}/\Delta t_{1j}$, where d_{1j} and Δt_{1j} are the geometrical and temporal distance between the 1st and the jth hit. Ratios smaller than 0.2 can origin from noise hits or long tracks, where the latter hit occurs after traveling longer distances in either time or space. In contrast cascade-like events show rather short distances between the consequent hits and low scattering that also limits the event's extension. Following the original proposal [99], events with a ratio larger than 0.5 are kept.

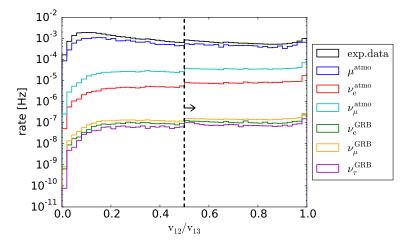


Figure 7.6: Velocity ratio distribution on level4. The arrow points to the region where events pass the level5 cut. GRB signal rates – arbitrarily scaled – are shown for the Γ 600 spectrum.

Topological Trigger Conditions: With the high rate of atmospheric muons entering the detector, there is also a chance of coincident events taking place that are misreconstructed as a single event, as schematically shown in figure 7.7.

In order to identify such coincident events, geometrical and temporal information is used by the Topological Trigger (TT) algorithm [160]. This method considers pairs of hits as connected if they occur closer than 15 optical modules on the same string or less than 150 m distant to each other on a different string. They are connected by causality if the difference $\Delta t - \Delta r/c$ is less than 450 ns for a pair with temporal distance Δt and geometrical distance Δr . The algorithm then tries to identify two clusters TTO and TT1, for which the variables nCh(TT0) and nCh(TT1) hold the number of hits in the 1st and 2nd cluster, respectively. The minimal number of hits required to form a cluster is five, otherwise the respective value TT0 or TT1 is set to 0. This explains the observed gaps in the distributions shown in figure 7.8. The condition nCh(TT0) > 0 – which actually corresponds to nCh(TT0) > 4 - cutsout noise events, while the cut on coincident events is realized by the condition nCh(TT1) = 0.

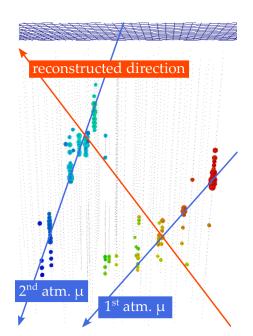


Figure 7.7: Schematic of two down-going atmospheric muons being misreconstructed as one up-going event. Plot taken from [122].

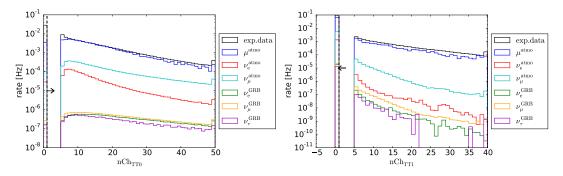


Figure 7.8: Topological trigger distributions on level4: *left*: nCh(TT0), *right*: nCh(TT1). The arrow points to the region where events pass the level5 cut. GRB signal rates – arbitrarily scaled – are shown for the Γ 600 spectrum.

Hit Veto: The particular veto region is defined as the part of IceCube that excludes the DeepCore fiducial volume. The cut requires that no hit is found in the cRT-cleaned pulse series within the veto region: $nCh_{veto}^{cRT} \leq 1$. Veto region hits are only counted before the SMT3 trigger time in order to keep hits that start in DeepCore and move outwards. Additionally, in analogy to the L4 cut restricting the number of events for the purpose of reconstruction quality, the same cut is applied on the pulse series used above: $nCh_{DC}^{cRT} \geq 6$.

Efficiencies from level4 to level5 are shown in table 7.3, again exemplarily for the Γ 600 spectrum as well as for background simulation and experimental data.

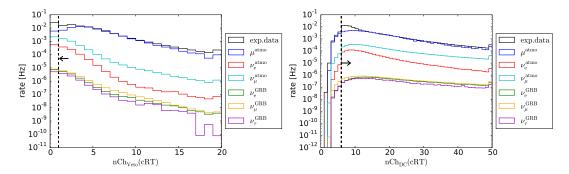


Figure 7.9: Hit veto parameter distributions on level4: left plot shows $nCh_{Veto}(cRT)$ and right plot shows $nCh_{DC}(cRT)$. The arrow points to the region where events pass the level5 cut. GRB signal rates – arbitrarily scaled – are shown for the $\Gamma600$ spectrum.

Table 7.3: Event selection level4 to level5 efficiencies. Signal rates are shown for the $\Gamma 600$ spectrum.

Levels	off-time data [%]	-	atm. ν_{μ} [%]	-	F-	-
L5/L4			51.5 ±0.1			

7.2.4 Level6 - Boosted Decision Trees

On this level, a machine learning algorithm is used to further classify the data into signallike and background-like events. The method chosen here is a so-called *Boosted Decision Tree* (*BDT*) using the implementation provided by the *pyBDT* software [161]. The underlying concept as well as the input parameters used for the classification are presented in this section. Afterwards, the training of the BDT and its performance is presented followed by a description of the cut on the BDT score that yields the event selection level6.

7.2.4.1 Boosted Decision Tree - Concept

A decision tree algorithm is, according to his name, representable by a tree structure as depicted schematically in figure 7.10: Starting with the *root node*, the path along the tree is given by a decision at each further node that is based on a discrimination variable c_j . Depending on the variables distribution and the classification of the events parameter x_i , a different path is chosen. At so-called *leaves*, marking the end point of such a path, a classification of the event into signal-like (S) and background-like (B) becomes possible.

The initial sample on level5 is split into two equally large samples of which one forms the *training sample* and the other one constitutes the *testing sample*. The training sample is used by the BDT to identify the discrimination variable distributions and defines the paths for separating signal and background events. The BDT's result is given for the testing sample as a score quantifying the signal-likeness (or background-likeness) of an event, with higher scores indicating an event to be more signal-like.

In order to enhance the quality of the algorithm, multiple trees - a so-called forest - are trained sequentially. The score of the previous tree is modified for the successor tree by a Boosting mechanism called AdaBoost [163]. Thereby the weights of the events are changed depending whether they got classified correctly by the BDT or not. In the first case, the weights get lowered, in the latter increased, so that the next tree focuses on the previously misclassified events. The resulting BDT is calculated as a weighted sum over the scores, where the weights are the forest's boost factors at each tree. The individual boost factors are the product of a user-defined boost-strength and the error-rate of the individual tree.

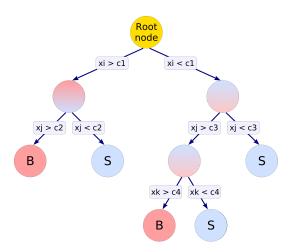


Figure 7.10: Schematic of a Boosted Decision Tree structure, taken from [162].

A second additional mechanism to improve the BDT results is *pruning*. This method aims at combining subtrees with low separation potential. Despite the obvious reduction of complexity, this is useful to reduce the effect of *overtraining* that will be explained later.

In the next section, the distributions of discrimination variables for the different data sets are shown; the ones for background simulation are given as a reference; the background from here on will be obtained from the experimental off-time datasets.

7.2.4.2 Discrimination Variables

In the following, the variables used in the BDT are described, concluding with the respective distributions on level5.

Monopod Zenith, *Z* & Energy: The Monopod reconstruction, described in section 5.2.4, is used to reconstruct cascade-like events. The algorithm's zenith, z-component of the reconstructed vertex and energy are chosen as input parameters for the BDT. The energy distribution is supposed to show its largest separation potential towards higher energies as atmospheric muons should extend more to higher energies but signal events are supposed to contribute more at lower energies, especially for the spectra with low Lorentz factors. Zenith and z-component of the vertex can be used to veto down-going events.

Millipede Zenith: The reconstructed zenith angle from the track reconstruction Millipede (see section 5.2.4) is also used as input parameter as atmospheric muons are still the dominating background contribution.

Resca *Z*: The *z*-uncertainty determined by the resca service (see section 5.2.5) gives discrimination potential of signal against atmospheric muons as the uncertainty in the *z*-component is supposed to be larger for true tracks than for true cascades since reconstruction is performed under the cascade hypothesis.

FiniteReco Length: The length of the finite track reconstructed by FiniteReco (see section 5.2.3) also gives a second input parameter considering the energies of the events. The length itself should be a strong separator between track- and cascade-like events, yielding shorter values for the latter.

Ndir & Ldir: These two parameters are defined on so-called *direct hits*. Those are required to occur in a time window of [-15 ns, +75 ns] around the geometrically expected time that an unscattered photon needs from the reconstructed track to the hit DOM. The underlying reconstruction is an MPE fit that is seeded with a 32-fold iterated SPE fit. The input parameter for the BDT are the number of direct hits n_{dir} and the direct length l_{dir} defined as the distance between the outermost direct hits projected on the reconstructed track. For both quantities, in principle, larger values mean more precise reconstruction.

rLogLSPE32: Another quality parameter used in the BDT is the *reduced log-likelihood* (*rlogL*) that is defined for a 32-fold iterated iSPE fit on the sRT-cleaned hit series as

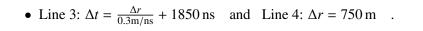
$$rLogL = \frac{-\log(L_{iSPE32})}{N_{sRT} - 2.5}$$
 (7.3)

"Reduced" hereby refers to the consideration of an effective number of degrees of freedom in the denominator $n_{d.o.f}$. In general, this would be done by using the denominator $n_{d.o.f} - n_{par}$, where $n_{d.o.f} = N_{sRT}$. For an iSPE32 fit the number of parameters n_{par} determined in the fit is five, namely the three vertex coordinates and the direction in zenith and azimuth angle. However, in order to eliminate a strong energy dependency, the denominator was replaced with the term $N_{sRT} - 2.5$ (see [164], optimized value taken from [165]).

nVetoHitsPulses: This cut was developed in [122] and takes causality into account to veto atmospheric muons. As the format of experimental data changed from the year 2011 to 2012, the algorithm was adjusted to take pulses into account instead of launches as in the original version. The rewritten code was made available to the collaboration.

The cut algorithm considers all hits in relation to a reference hit, in this case, the third HLC hit in the SMT3. The temporal and geometrical differences of the ith hit with respect to the reference hit $\Delta t = t_{ref} - t_i$ and $\Delta r = |r_{ref} - r_i|$, respectively, are then used to span a veto region as shown in figure 7.11. The veto aims at removing atmospheric muons and therefore the region encloses the space in which atmospheric muons are supposed to be found. In the plots, the lines that limit such a region are indicated in red. Atmospheric muons are expected to enter the detector below *Line 1*, as well as leaving the detector below *Line 2*. Hits below *Line 3*, which is parallel to Line 1 but shifted in time, are also caused by incoming muons which are delayed by more than the time shift, so veto hits lie above this line. Line 4 eventually marks a distance where no veto hit can be found as this is outside the detector volume. Respective values for time difference and geometrical shift for the different lines have been optimized in [122] for background separation potential, yielding

• Line 1: $\Delta t = \frac{\Delta r}{0.3 \text{m/ns}} + 150 \text{ ns}$, Line 2: $\Delta t = \frac{-\Delta r}{0.2 \text{m/ns}} + 500 \text{ ns}$



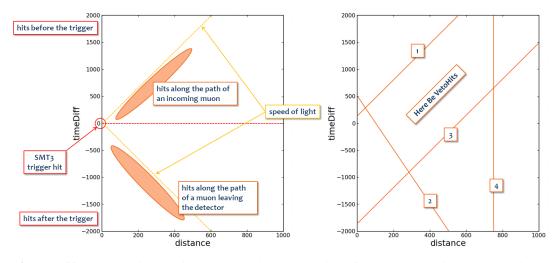


Figure 7.11: *Left:* physical motivation, *right:* implementation of the veto region in the geometrical and temporal distance space. The veto region is chosen along the path of muons entering the detector shown in the right plot. Taken from [122].

Discrimination Variable Distributions: Distributions of Monopod reconstructed zenith angles and *z*-components are shown for the Γ 600 spectrum in figures 7.12 and 7.13 as examples. For the other input parameters, the respective plots can be found in appendix D.1.

Most interesting regarding those plots is, however, not the absolute value of the rate but the shape as very different distributions make it easier for the BDT to separate signal from background.

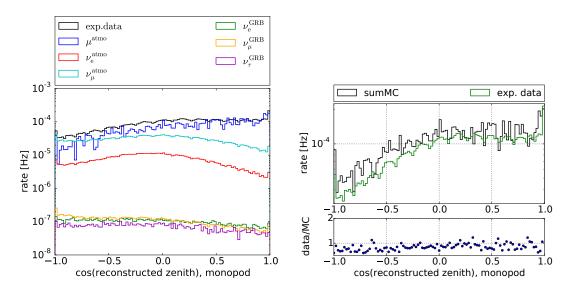


Figure 7.12: Monopod reconstructed cos(zenith) distributions on level5. GRB signal rates – arbitrarily scaled – are shown for the $\Gamma600$ spectrum. Shown are individual contributions on the left and the sum of background simulations (sumMC) vs. experimental data on the right, as well as the data/MC ratio.

The Monopod reconstructed zenith displayed in figure 7.12 provides a nicely separable example. The distribution for experimental data and atmospheric muons peaks in the down-going region while the signal neutrino distributions peaks in the up-going region. In this example, the data/simulation ratio (data/MC) is rather flat and centered around 1, however, slight deviations are observable.

For the second example – the Monopod reconstructed *z*-component displayed in figure 7.13 – the data/MC ratio is large. However, this is only caused by the simulation, especially for atmospheric muons, running out of statistics. In the following discussion and in the BDT, background will be taken from the off-time sample. Thus, the data/MC deviation is no reason of concern for this work.

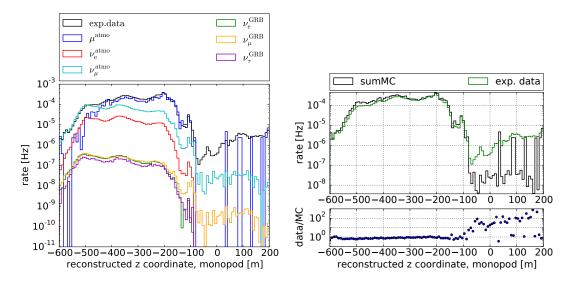


Figure 7.13: Monopod reconstructed *z*-coordinate distributions on level5. GRB signal rates – arbitrarily scaled – are shown for the Γ 600 spectrum. Shown are individual contributions on the left and the sum of background simulations (sumMC) vs. experimental data on the right, as well as the data/MC ratio (note the logarithmic scales).

The correlation between the discrimination variables is depicted in figure 7.14 (exemplarily for the Γ 600 spectrum, for other spectra see appendix D.2). As expected, the strongest correlation is observable between Ldir and Ndir that are correlated by the underlying principle. As those are the only ones showing a larger correlation, one can conclude that none of the variables chosen is redundant.

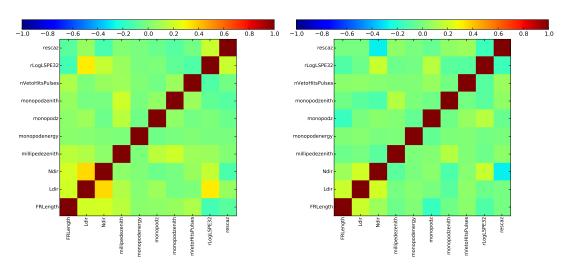


Figure 7.14: Correlation coefficients of the input parameters for a BDT trained for the Γ600 spectrum. Off-time data is shown in the left plot and signal in the right. Except for the self-correlations and the correlation between Ldir and Ndir as well as a minor correlation between rLogLSPE32 and Ldir/Ndir, no unexpected correlation is observable.

7.2.4.3 BDT Training

When training a BDT, it can become subject to so-called *overtraining* that can be further classified into training sample and data/MC overtraining. In general, the term refers to a learner restricting training data too tightly and thereby recognizing differences in the respective training samples while it is not able to recognize the differences between signal and background. The BDT is trained with a setting of 320 trees, a maximum tree depth of 3, a boosting strength of 0.7 and a conservative pruning strength of 35. This choice of settings yields no signs of overtraining; the checks performed are explained in more detail further below.

Training Sample Overtraining: A way to detect training sample overtraining is provided by the Kolmogorov-Smirnov test⁸³ (*KS* test) which is performed to check whether two distributions origin from the same data sample. Higher KS p-values hereby indicate better matching of training and testing sample, while low values – below 0.001 – indicate overtraining. The results of the test are exemplarily shown for the $\Gamma600$ spectrum in figure 7.15. As training and testing samples for signal and background clearly match with KS p-values of 0.9 for signal and 0.4 for background, the effect of training sample overtraining can be excluded for the chosen setting.

⁸³Named after the Soviet mathematicians Andrei Nikolajewitsch Kolmogorow and Nikolai Wassiljewitsch Smirnow.

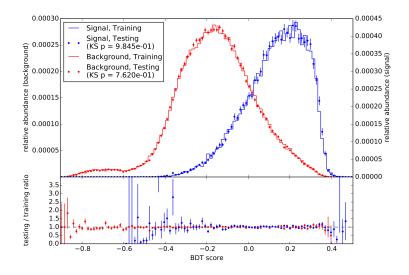


Figure 7.15: Training sample overtraining check exemplarily shown for the Γ 600 spectrum. As the respective KS p-values are rather large (0.9 and 0.7), training sample overtraining can be excluded. The ratio of signal and background testing sample to training sample is shown below, and also shows no unexpected behavior, as the ratio centers at 1 for high statistics regions.

Data/MC Overtraining: Another kind of overtraining is the so-called data/MC overtraining, especially problematic for analyses like this work, where background is taken from data, while the signal hypothesis origins from simulations. Overtraining here means a possible separation of signal-like data events from signal-like simulation events that origins from imperfect simulation. As this overtraining, in contradiction to the before mentioned one, is not clearly identifiable by a KS-test, the only way to exclude such overtraining is a check for the skewness of the data/MC ratio in the transition region from background to signal. A small ratio in the signal region and consequently a large ratio in the background region disturbing a monotonous characteristics indicate this kind of overtraining as signal-like data events are cut away.

For the Γ 600 spectrum, the resulting score distribution is exemplarily shown in figure 7.16. As can be seen, the data/MC ratio is rather monotonous showing no skewness effect in the transition region, which excludes data/MC overtraining as a major effect.

As both kinds of overtraining effects may be excluded, an initial cut on the BDT score can be set. The value -0.1 was chosen for all spectra and is close to the turnover point, where the rate of atmospheric muons begins to decrease and starts becoming subdominant to the atmospheric neutrino rate. However, the cut is weaker for the soft spectra, allowing for more background events. The resulting datasets are the basis for the time consuming event selection at level7.

As can be seen in figure 7.17, the efficiencies at this cut score are not as large as for harder cuts. However, for some spectra, such a more stringent cut will be applied later on level7. Efficiencies with respect to level5 are shown in table 7.4. As can be seen, the BDT removes almost a third of the data while keeping more than 90 % of the signal.

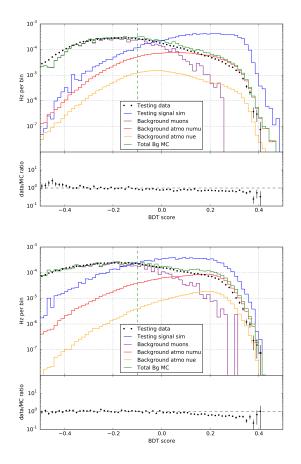


Figure 7.16: BDT score distributions for the Γ 600 (top) and the Γ 100 (bottom) spectrum. The initially chosen BDT score cut value of -0.1 is shown by vertical green dashed lines. Later-on, a harder cut is chosen for all the spectra, yielding optimal sensitivities.

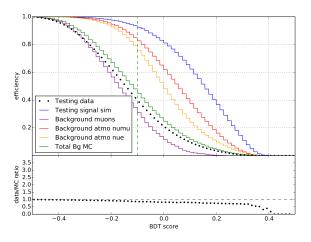


Figure 7.17: BDT score cut efficiencies shown for the Γ 600 spectrum. The initially chosen BDT score cut value of -0.1 is indicated by a vertical green dashed line.

Levels	off-time data [%]			atm. ν _µ [%]			
L6/L5	37.3 ±0.1	28 ±1	83.2 ±0.3	85.4 ±0.2	92 ±4	_	92 ±8

Table 7.4: Event selection level5 to level6 efficiencies. Signal rates are shown exemplarily for the Γ 600 spectrum.

7.2.5 Rate Summary

The resulting rates at the different event selection levels are shown in table 7.5 and in figure 7.18. Most important to quantify the effects of the event selection, however, are the ratios of the rates from level3 to level6, which are of order 20% for signal neutrinos (in all investigated spectra) and atmospheric background neutrino. For the atmospheric muon background, which dominates the data on early levels, the ratio is about one per mil, which eventually makes atmospheric neutrinos the dominating background at level6. With a rate of 3 mHz it is now possible to perform the likelihood algorithm, described in the next section.

Table 7.5: Event selection rates from level3 to level6. Signal efficiencies are shown exemplarily for the Γ 600 spectrum.

Level	off-time data [mHz]	atm. μ [mHz]	atm. ν _e [mHz]	atm. ν _μ [mHz]
L3	2178 ± 3	1824 ± 2	2.740 ± 0.002	12.05 ± 0.01
L4	114.3 ± 0.1	76.8 ± 0.5	1.346 ± 0.002	5.76 ± 0.01
L5	9.10 ± 0.02	7.02 ± 0.14	0.731 ± 0.002	2.97 ± 0.01
L6	3.40 ± 0.01	1.99 ± 0.07	0.6079 ± 0.0002	2.535 ± 0.001
L6/L3	$(0.156 \pm 0.001)\%$	$(0.109 \pm 0.004)\%$	$(22.2 \pm 0.7)\%$	$(21.0 \pm 0.4)\%$

Level	sig. ν _e [μHz]	sig. ν _μ [μHz]	sig. ν _τ [μHz]
L3	2025 ± 4	2764 ± 2	1562 ± 9
L4	1154 ± 3	1377 ± 2	805 ± 6
L5	606 ± 4	651 ± 2	424 ± 5
L6	558 ± 3	598 ± 2	388 ± 4
L6/L3	$(27.6 \pm 1.0)\%$	$(21.6 \pm 0.4)\%$	$(24.8 \pm 0.2)\%$

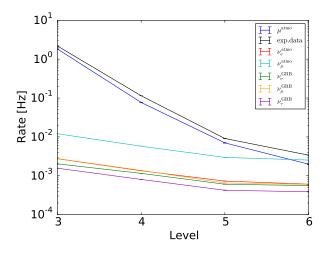


Figure 7.18: Event selection rates for level3 to level6. Signal rates are shown exemplarily for the Γ 600 spectrum. Most remarkably is that atmospheric neutrinos have become the dominant background at level6.

7.3 Likelihood Analysis and Final Event Selection

The fundamental method is based on an unbinned likelihood analysis. In contrast to a cutand-count method, which counts the events observed in the on-time region and simply compares this with the expected counts evaluated within the off-time regions, a likelihood ansatz uses the probability of each individual event to be a signal or background event. Each events' probabilities then contribute to a signal and background *probability density function (PDF)* – presented in section 7.3.2 – that are used to define a test statistic *T* as explained in section 7.3.1. The significance of an event being signal-like is derived from this test statistics in a frequentist approach outlined in section 7.3.3.

7.3.1 Likelihood Method and Test Statistics

The unbinned likelihood algorithm used in this analysis is provided by the grbllh software. Central to the approach is the likelihood function \mathcal{L} evaluated for, in total, N events with parameter sets x_i for the ith event. With the number of observed events n consisting of n_s signal events and n_b background events, the likelihood can be written as

$$\mathcal{L}(N, x_i; n) = P(N; n_s + n_b) \cdot \prod_{i=0}^{N} p_i(x_i)$$
, (7.4)

where *P* is the probability to see *n* out of *N* events following the Poissonian distribution $P = n^N/N! \cdot \exp(-n)$ and p_i are the probability functions for the ith event to have parameters x_i . The latter can be expressed as $p_i = n_s/N \cdot S + n_b/N \cdot B$ with a signal and a background part that contains signal- and background-only PDFs *S* and *B*, respectively. Using these in equation 7.4 yields

$$\mathcal{L}(N, x_i; n_s + n_b) = \frac{(n_s + n_b)^N}{N!} \cdot \exp(-n_s - n_b) \cdot \prod_{i=0}^N \frac{n_s \cdot S + n_b \cdot B}{n_s + n_b} \quad .$$
(7.5)

In principle, the aim is to find the parameters that maximize equation 7.5. However, for computational reasons, it is more convenient to equivalently maximize the logarithm of the likelihood given by

$$\ln(\mathcal{L}(N,x_i;n_s+n_b)) = -n_s - \langle n_b \rangle - \ln(N!) + \sum_{i=0}^N \ln(n_s \cdot S(x_i) + \langle n_b \rangle \cdot B(x_i)) \quad , \tag{7.6}$$

with the median number of background events $\langle n_b \rangle$. Eventually, the test statistic value T is defined as the likelihood ratio normalizing the likelihood 7.6 at the best-fit value \hat{n}_s to the background-only likelihood function

$$\ln(\mathcal{L}_{0}(N,x_{i};n_{b})) = \ln(\mathcal{L}(N,x_{i};n_{s}+n_{b}))\Big|_{n_{s}=0} = -\langle n_{b}\rangle - \ln(N!) + \sum_{i=0}^{N}\ln(\langle n_{b}\rangle \cdot B(x_{i})) \quad , (7.7)$$

such that

$$T = \ln\left(\frac{\mathcal{L}}{\mathcal{L}_0}\right) = -\hat{n}_s + \sum_{i=0}^N \ln\left(\frac{\hat{n}_s}{\langle n_b \rangle} \frac{S(x_i)}{B(x_i)} + 1\right) \quad .$$
(7.8)

Assuming that correlations between space, time and energy are sufficiently small, S and B can be split into separate parts as

$$S(x_i) = S_{\text{space}}(d_i) \cdot S_{\text{time}}(t_i) \cdot S_{\text{energy}}(E_i)$$
 and (7.9)

$$B(x_i) = B_{\text{space}}(d_i) \cdot B_{\text{time}}(t_i) \cdot B_{\text{energy}}(E_i) \quad .$$
(7.10)

Using this, the test statistic can be written as

$$T = -\hat{n}_s + \sum_{i=0}^{N} \ln\left(\hat{n}_s \cdot \frac{1}{\langle n_b \rangle} \cdot \left(r_{\text{space}} + r_{\text{time}} + r_{\text{energy}}\right) + 1\right) \quad , \tag{7.11}$$

with individual likelihood ratios for space, time and energy r_{space} , r_{time} and r_{energy} , respectively. Introducing the total, normed PDF ratio $r_{\text{tot}} = \frac{1}{\langle n_b \rangle} \left(r_{\text{space}} + r_{\text{time}} + r_{\text{energy}} \right)$, this can be rewritten as

$$T = -\hat{n}_s + \sum_{i=0}^{N} \ln\left(\hat{n}_s \cdot r_{\text{tot}} + 1\right) \quad .$$
 (7.12)

7.3.2 Probability Distribution Functions

7.3.2.1 Space PDF

The uncertainty in determining the direction and therefore the space PDF can be illustrated by the angular resolution, shown in figure 7.19. The overall weighted median angular resolution that is achieved by the Monopod reconstruction, exceeds the muon-flavor reconstruction only below 30 GeV. However, it improves from roughly 40° at level6 to about 32° with a harder BDT score cut.

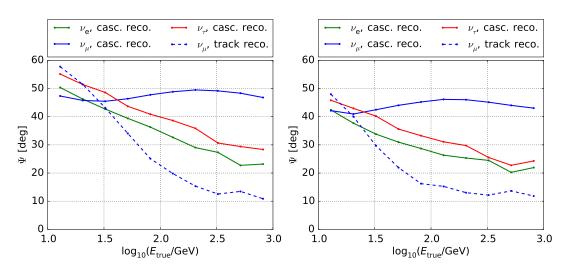


Figure 7.19: Angular resolution Ψ depicted as angular distance between true and reconstructed direction against energy at level6 (left) and on level6 with a harder cut on the BDT score at 0.1 (right) that is, as explained later, chosen for the final sample. In order to show a large energy range, the plots are generated for the E^{-2} spectrum which is the hardest spectrum in this work and therefore holds the highest neutrino energies. Solid lines show the resolutions achieved by the Monopod cascade reconstruction for the various neutrino flavors. The dashed line is the result of the Millipede track reconstruction for ν_{μ} .

Interesting for a characterization is not only the angular resolution but also the so-called *pull* which is the ratio of the angular resolution Ψ to the estimated angular uncertainty σ_{Ω} . The latter is given by

$$\sigma_{\Omega} = \sqrt{\sigma_{\theta}^2 + (\sigma_{\phi} \cdot \sin \theta)^2}$$
(7.13)

and takes the zenith and azimuth resolutions σ_{θ} and σ_{ϕ} calculated by resca into account. For a perfect reconstruction this ratio equals 1; however, as can been seen in figure 7.20, the ratio shows an energy dependence. In order to correct for this effect, a linear function is fitted to the median pulls in each energy bin. As again E^{-2} provides the hardest spectra and therefore shows the largest neutrino energy range with sufficient statistics, the fit on this spectrum was used and applied to all others as well. From now on, $\Psi = f(E_{\text{reco}}) \cdot \sigma_{\Omega}(E_{\text{reco}})$ is used as the angular uncertainty where the fitting function was determined to be

$$f(E_{\text{reco}}) = 0.366 \cdot \log_{10}(E_{\text{reco}}/\text{GeV}) + 0.242$$
 . (7.14)

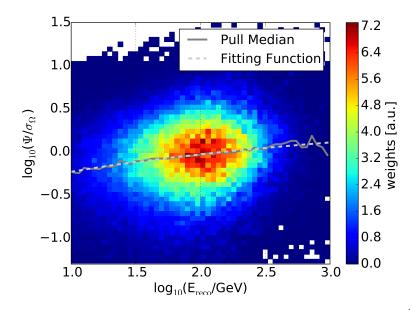


Figure 7.20: Distribution of the pull for the neutrino signal simulation following the E^{-2} spectrum vs. the logarithm of the reconstructed energy. The median of the pull Ψ/σ_{Ω} is shown (solid gray line) as well as the fit to the medians (dashed light gray line) giving the respective correction function. White areas mark regions where no data are available.

The signal space direction distribution is constructed such that it becomes maximal if the event directs towards the GRB. The underlying PDF is given as a von-Mises distribution⁸⁴, which is equivalent to the first-order term of the Kent distribution⁸⁵. The von-Mises distribution basically represents a 2D Gaussian distribution on the sphere instead of a plane, which is preferable, as it guarantees normalization even for large angular uncertainties. The distribution is given by:

$$S_{\text{space}} = \frac{1}{4\pi} \frac{\kappa}{\sinh(\kappa)} \exp^{\kappa \cdot \cos(\Psi)} \quad , \tag{7.15}$$

where the concentration parameter

$$\kappa = (\sigma_{\Omega}^2 + \sigma_{\text{GRB}}^2)^{-1} \tag{7.16}$$

depends on the accuracy of the GRB's position σ_{GRB} . In the case where the Fermi-GBM detector provides the most precise GRB direction, the formula 7.16 is extended to take Fermi-GBM's systematic errors of 2.6° (weight of 0.72) and 10.4° (weight of 0.28) into account [166]. With

$$\kappa_{2.6} = \frac{1}{\sigma_{\Omega}^{2} + \sigma_{\text{GRB}}^{2} + (2.6^{\circ})^{2}}$$
$$\kappa_{10.4} = \frac{1}{\sigma_{\Omega}^{2} + \sigma_{\text{GRB}}^{2} + (10.4^{\circ})^{2}}$$

⁸⁴Named after the Austria-Hungarian mathematician Richard Edler von Mises.

⁸⁵Named after the statistician John T. Kent.

and the respective weights, the signal space PDF for GRBs localized by Fermi-GBM becomes

$$S_{\text{space}}^{\text{GBM}} = 0.72 \cdot S_{\text{space}} \Big|_{\kappa = \kappa_{2.6}} + 0.28 \cdot S_{\text{space}} \Big|_{\kappa = \kappa_{10.4}} \quad . \tag{7.17}$$

The background space PDF is calculated using spline fits on the Monopod reconstructed $\cos \theta_{\text{zenith}}$ distribution taken from experimental off-time data.

Both signal and background distributions are shown in figure 7.21; for the signal PDF three different angular resolutions $\sigma = 1/\sqrt{\kappa}$ are chosen as examples.

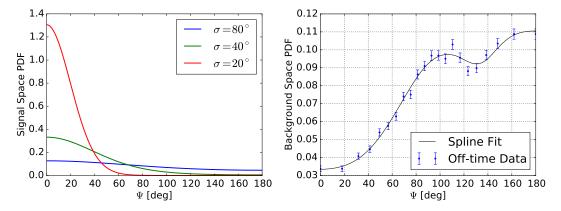


Figure 7.21: Space PDFs used in the likelihood algorithm for signal (left) and background (right). For the signal PDF, three different angular resolutions σ are chosen exemplarily. The 40° and 20° examples hereby enclose the expected median angular resolution of about 30°. The 80° example is chosen to illustrate the PDF shape for large deviations of the GRB from the event direction. The background PDF is fit to off-time data for the Γ 600 spectrum at level6 with an additional BDT score cut at 0.1.

7.3.2.2 Time PDF

The signal time distribution for each GRB is chosen to be flat over the respective T_{100} . On both sides, Gaussian tails extend this distribution. The width of the Gaussian distribution is set to T_{100} , if T_{100} lies within the interval [2 s, 30 s], otherwise the Gaussian width is set to the interval limit nearest to T_{100} . The Gaussian distribution is truncated at 4σ at both sides, which gives a total time window of $T_{100} + 8\sigma$.

The background PDF is chosen to be flat over the same total time window. The ratio of signal time PDF to background time PDF is shown in figure 7.22.

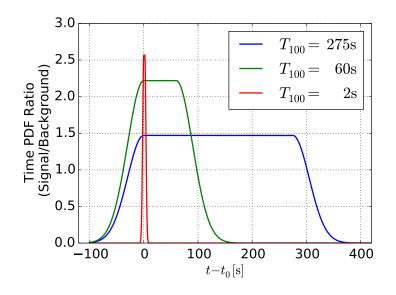


Figure 7.22: Signal to background time PDF ratio for exemplarily chosen long, medium and short bursts. The long burst duration was set close to the duration of GRB130427A.

7.3.2.3 Energy PDF

The energy used in the likelihood is determined by the Monopod reconstruction. The energy spectrum, weighted according to the investigated model, enters the signal energy PDF; the background energy PDF is estimated by using spline fits to the experimental off-time data. Both distributions are shown exemplarily for the $\Gamma600$ spectrum in 7.23.

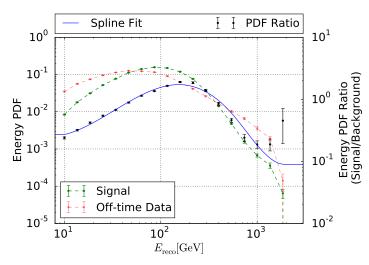


Figure 7.23: Off-time and signal data are shown exemplarily for the Γ 600 model at level6 with a BDT score cut at 0.1. *Left y-axis*: Energy PDFs for background taken from off-time data and signal. *Right y-axis*: Signal to background energy PDF ratio as blue line, calculated by spline-fitting the ratio shown in black.

7.3.3 Frequentist Evaluation

In this work, a frequentist approach is chosen to calculate the statistical significance. Thereby, pseudo-experiments are used to determine the test statistic value for background-only and signal-contaminated samples.

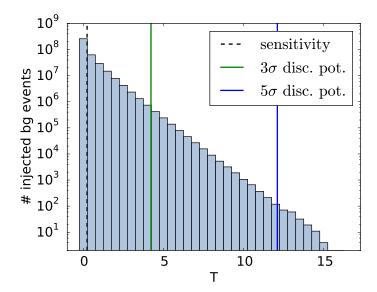
In each background trial, a pseudo-random number of observed events is chosen within the $T_{100} + 8\sigma$ time interval by sampling the Poissonian distribution

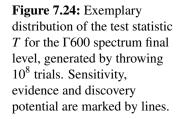
$$P_{j} = \frac{\langle n_{b} \rangle_{j}^{N}}{N_{j}!} \cdot \exp(\langle n_{b} \rangle_{j}) \quad , \tag{7.18}$$

with the background rate $\langle n_b \rangle_j$ of the j^{th} GRB. If a so-determined number is larger than zero, an event time is drawn from the time PDF and an azimuth value is drawn between 0 and 2π . The reconstructed energy is sampled from the binned background energy distribution. The zenith angle is sampled from the energy bin corresponding to the previously chosen value. The estimated directional error is determined the same way by sampling from the energy-zenith bins that corresponds to the previous values. Afterwards, the signal and background PDFs as well as the test statistic are calculated.

The signal-contaminated sample contains 10^4 pseudo-experiments where simulated signal events are injected in addition to background events. The signal injection is repeated with a new sample that has increased weights, until the required flux limit is reached. The limits investigated in this work refer to the *sensitivity* and the *evidence potential*. Sensitivity is defined as the flux at which 90% of the signal-contaminated trials have a test statistic value larger than the median of the background-only trials. With this choice of required percentage, sensitivity is quoted at 90% confidence level (90%C.L.). The 5σ discovery potential is defined as the lowest flux that yields a test statistic value larger than 5σ at 50% probability to observe the signal. Equivalently, the 3σ discovery potential – often referred to as evidence potential – is defined at 3σ .

The background-only test statistic distribution is shown in figure 7.24, with lines indicating sensitivity, evidence and discovery potential thresholds⁸⁶. The BDT score cut will be chosen at optimal sensitivity. However, a possible optimization on evidence potential yields similar results, as will be shown later.





In order to proceed, two important quantities need to be introduced: the effective area and the number flux. The resulting flux limits will be given on the number-flux which is calculated from the number of signal events at the respective limits divided by the effective area.

⁸⁶In this figure as well as in the following calculations, the median for the test statistic distributions has been rounded to 0.0 by the grbllh software. As the distribution is clearly dominated by the entries at T = 0.0, the resulting shift is rather small, e.g. 0.24 for the Γ 600 spectrum.

Effective Area: The effective area is a measure that quantifies how many events survived the cuts in-between generation level and a following event selection level. For a half-sky search, it is defined as

$$A_{\rm eff} = \frac{\sum_i w_i}{\Delta E \cdot 2\pi} \quad , \tag{7.19}$$

with an energy interval ΔE and the weights w_i at generation level.

The effective energies for the respective datasets on L6 – including the later optimized BDT score cut – are shown as function of energy for the northern and southern hemispheres and as function of the cosine of the zenith angle in figure 7.25. For the latter, the cosine of the zenith angle is chosen to provide a directional variable taking the space angle element into account. The behavior of the effective area follows the expectation for a northern hemisphere search as the value decreases towards the southern hemisphere.

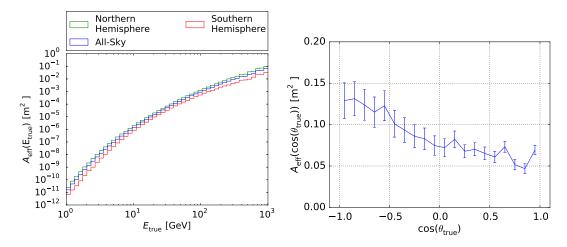


Figure 7.25: Effective areas as function of energy for the two hemispheres (*left*) and as function of $\cos(\theta_{\text{true}})$ (*right*). Both plots are shown for the $\Gamma600$ spectrum exemplarily on L6 with an additional BDT score cut at 0.1.

In comparison to a previous ν_{μ} -only search (see figure 7.26), the effective area for an allflavor approach yields a factor of two higher effective areas at 100 GeV and a factor of four higher effective areas at about 200 GeV. At energies below 40 GeV, the ν_{μ} search shows higher values because of harder cuts implemented in that analysis. Also, for higher energies of about 1 TeV, this analysis is competitive with regard to previous works, e.g. to [42] – an analysis optimized for highest energies reaching 10⁹ GeV which quotes an effective area of about 10^{-2} m² at 1 TeV. Although the respective optimization aims at different energy regimes, this work's effective area is a factor ten higher with more than 10^{-1} m² achieved at 1 TeV.

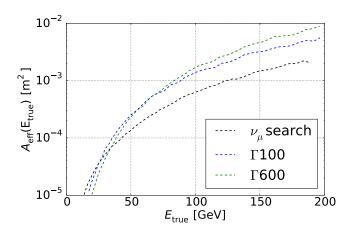


Figure 7.26: Effective areas for the most relevant energy range of this work for the $\Gamma600$ (green line) and $\Gamma100$ (blue line) spectra. As can be seen, the soft spectrum has a higher effective area at lower energies which changes at about 65 GeV. The black line is the effective area of a ν_{μ} northern sky transient search [158].

Number Flux: In order to determine a flux, the ratio of the required number of signal events and the effective area is used in this work. For the stacked searches, the mean effective area is defined as

$$\bar{A}_{\text{eff}}^{\text{nsky}} = \frac{\sum\limits_{\text{E-bins}} A_{\text{eff}}^{\text{nsky}}(E) \cdot w(E)}{\sum\limits_{\text{E-bins}} w(E)} \quad , \tag{7.20}$$

where w(E) denotes the respective spectral weight for each event. For the single source analysis, this is further refined as the effective area is calculated in a zenith band of ± 0.1 rad around the source's true zenith as

$$\bar{A}_{\text{eff}}^{\text{GRB}} = \frac{\sum\limits_{\text{E-bins}} A_{\text{eff}}^{\text{GRB}}(E) \cdot w(E)}{\sum\limits_{\text{E-bins}} w(E)} \quad .$$
(7.21)

With the definitions of a spectral-weighted effective area, a number flux can be defined as

$$\Phi = \frac{n_s^{\text{thres}}}{\bar{A}_{\text{eff}}} \quad , \tag{7.22}$$

with the number of signal events n_s^{thres} required to pass the respective threshold, such that

$$\Phi^{\text{sens}} = \frac{n_s^{\text{sens}}}{\bar{A}_{\text{eff}}} \quad \text{and} \quad \Phi^{\text{disc.pot.}} = \frac{n_s^{\text{disc.pot.}}}{\bar{A}_{\text{eff}}} \quad .$$
(7.23)

7.3.4 Level7 - Final Event Selection and Sensitivities

Misreconstructed Events: Another quality cut was applied for the final sample as the test statistic distribution can be rather sensitive to misreconstructed events. To exclude such events, two soft cuts were implemented that require the estimated angular resolution by resca and the reconstructed energy to be in reasonable regions. The latter cut is defined as a limit on the reconstructed energy which is reasonable as it cuts out high energy events that this analysis is not aiming at. The cut conditions are implemented as $\Psi < 5$ rad and $E_{\text{reco}} < 2$ TeV. With less than 2% of the events removed, those cuts are weak for the hard spectra compared to the optimized cut on the BDT score that will be explained in the following.

BDT Score Optimization: The number sensitivity, the effective area and the number flux sensitivity for the $\Gamma600$ model for various BDT cut score values is exemplarily shown in figure 7.27. The optimization results for the remaining spectra can be found in appendix E.1. The number of trials for the optimization scan is reduced to $10^7 - i.e.$ a factor of 100 - which means a slight loss in accuracy but a required decrease in computation time. As the optimization is done for sensitivity, the statistics is sufficient for this calculation.

As expected, effective area and number counts decrease with harder cuts. The flux sensitivity shows a clear minimum, which defines the optimal BDT cut score. However, as the minimum is wide, there is also some flexibility left, where to put the cut.

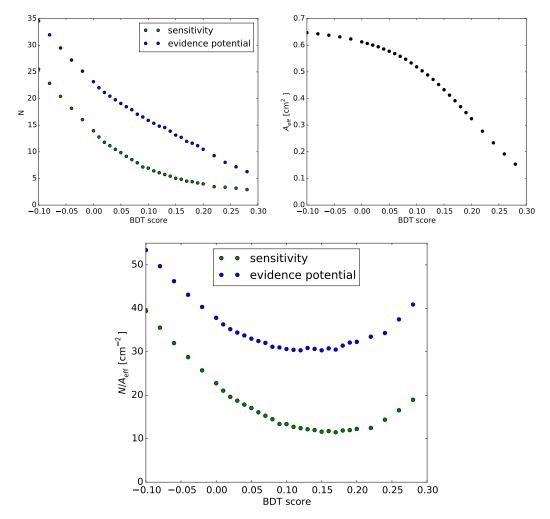
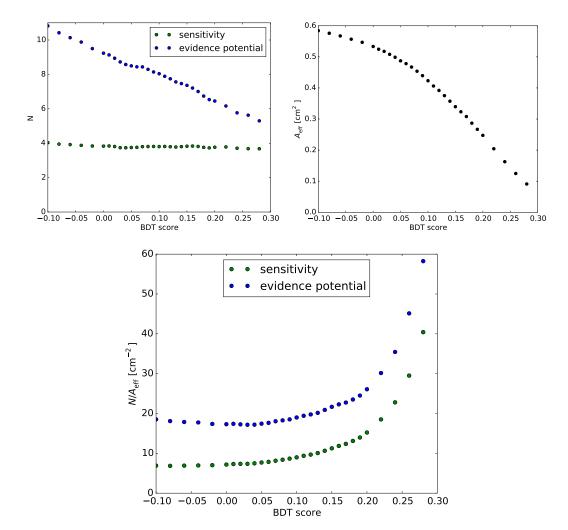


Figure 7.27: Flux optimization for the Γ 600 stacked search. Given are both sensitivity and evidence potential (3σ potential) curves. The optimized score cut (at 0.17) was chosen to maximize the sensitivity on the number flux.

The optimal BDT score cut value is in the same range of 0.16-0.17 for all stacked analyses; in all cases, the sensitivity yields a clear minimum and the shapes of the sensitivity and evidence



potential curves are similar. However, this is not the case for the single source search, for which the according plots are shown in figure 7.28.

Figure 7.28: Flux optimization for the Γ 600 single source search. Given are both sensitivity and evidence potential (3σ potential) curves. The optimized score cut (at -0.08) was chosen to maximize the sensitivity on the number flux.

While the effective area varies only slightly in shape, the number sensitivity basically becomes flat, what happens for the stacked searches only at rather hard BDT score cuts. However, the minimal flux occurs at a BDT score of -0.08. Although a much larger score is possible if an optimization on the evidence potential was used instead, the softer cut value was chosen to remain consistent in optimization and in order to impose a too stringent cut.

The results of the optimization for the individual spectra as well as the rates and efficiencies on final level are given in table 7.6. Note that the signal rates are determined as ratios of the number sensitivity over the summed T_{100} of the contributing GRBs. For the stacked searches, this sum is roughly 23 times higher than for the single source search, which explains their

lower signal rates. The lower background rates for the stacked searches is due to the harder BDT score cut.

	Optimal	l Off-time	e Sample	Sig	nal
Spectrum	BDT	Rate	L7/L6	Rate	L7/L6
	Score	ε [μHz]	[%]	[µHz]	[%]
E-2	0.17	250(3)	7.4(1)	637(10)	39(1)
600	0.17	365(4)	10.7(1)	702(4)	45(1)
100	0.17	/ 505(4)	14.9(1)	889(2)	46(2)
100npc	0.16	542(5)	15.9(2)	915(2)	47(1)
600single	-0.08	3106(11)	91.3(4)	14383(56)	96(1)
Spectrum	$A_{\rm eff}$	N ^{90% C.L.}	$\Phi_{\text{sens}}^{90\% \text{ C.L.}}$	N _{ev} ^{90% C.L.}	Φ ^{90% C.L.}
-	[cm ²]	Sens	$[\mathrm{cm}^{-2}]$		$[cm^{-2}]$
E-2	0.94	4.1	4.3	10.4	11.1
600	0.39	4.5	11.4	11.9	30.5
100npc	0.03	5.9	235.6	15.1	548.6
100	0.03	5.7	212.5	14.7	610.6
600single	0.58	3.9	6.9	10.4	18.1

Table 7.6: Results of the BDT score cut optimization.

7.3.5 Systematic Uncertainties

Systematic effects have to be regarded as simulated events are used in the likelihood method to obtain the sensitivities as shown above. Such effects derive from various sources, e.g. the modeling of the optical modules and the Antarctic ice as well as from the assumed neutrino nucleon cross-sections, whose uncertainty, as it turns out, contributes most.

In order to investigate DOM efficiencies, GENIE datasets in which the assumed efficiency is set to ± 10 % around the standard values are used. These datasets are processed through the same event selection as the other simulation datasets. This includes the same BDT that was trained with the respective standard set, so no new training is applied for systematics. The same BDT score cut is consequently applied on L7. The expected behavior, namely that the DOM efficiency effects soft spectra more, as they contribute more low-energetic events, is not observed. This is due to the usage of spectral-weighted effective areas, which cut out the low-energy regimes. The observation that the overall effect is still pronounced in the $\Gamma600$ spectrum is not yet fully understood.

The effect of varying scattering and absorption coefficients has been studied in recent searches for high- as well as low-energetic neutrinos [42, 99]. For both energy regimes, the systematic effect is estimated to be about 10 %. The effect of absorption is hereby stronger than the effect of scattering which was shown in a high-energy GRB search [42]. For low-energy neutrino searches, however, absorption is a minor effect compared to scattering, so that the estimate is rather conservative.

The influence of seasonal variations in the atmospheric muon rate has become negligible at later event selection levels as can be seen in figure 7.3. However, previous studies with grbllh have shown that respecting those variation by introducing a rate systematic of 10% had no influence on the sensitivities calculated by grbllh [42].

Another systematic effect is introduced by coincident events. In the event selection, however, the effect is treated by the Topological Trigger algorithm which tries to identify coincident events and removes them from the data. The systematic error caused by the imperfection of the algorithm is estimated to be of order 1 % in the relevant energy range of this work [167].

DIS neutrino-nucleon cross-section introduce the largest systematic error. In a study estimating the systematic effect for even lower energies within the PINGU low-energy extension, a 15% effect is estimated [8]. Various IceCube studies, also in the low-energy regime, like e.g. [99], assume, however, only 10%. In order to make a conservative assumption, the uncertainty in this work is set to be 15%.

Neutrino oscillations in earth matter have been investigated in this work – as described in section 7.1 – but show no observable influence in the relevant energy regime. The commonly used systematic effect of the oscillation parameters of about 6 % [99] does not contribute for all-flavor analyses like this work.

The total systematic uncertainty is eventually determined from the above mentioned individual contributions $\sigma_{sys, i}$ as

$$\sigma_{\rm sys, \, tot} = \sqrt{\sum_{i} \sigma_{\rm sys, \, i}^2} \quad . \tag{7.24}$$

A summary of the studied systematics as well as the final sensitivities are given in table 7.7. The latter are determined by adding the systematics effects on the uncorrected systematics from table 7.6.

Spectrum	DOM Eff.	Ice Model	ν_{μ} cross sec	coinc	Sum	$\Phi^{90\% \text{ C.L.}}_{\text{sens, sys}}$
	[%]	[%]	[%]	[%]	[%]	$[cm^{-2}]$
E-2	+ 8	10	15	1	20	5.2
600	+12	10	15	1	22	13.9
100	- 2	10	15	1	18	278.0
100npc	- 1	10	15	1	18	250.8
600single	+ 9	10	15	1	20	8.3

Table 7.7: Individual and summed systematic uncertainties as well as the corrected sensitivities.

7.4 Results of the Stacked and Single Source Searches

After reviewing of the above presented event-selection and likelihood method the analysis received unblinding permission by the collaboration. Therefore, the on-time datasets were processed through the same event selection steps as the off-time sample with the respective optimized BDT score cut. The results of the likelihood method are presented in this section.

The on-time rates on final level are displayed in table 7.8 and are in agreement with the off-time samples for the thermal spectra (see table 7.5) within the error bands; only the E^{-2} spectrum shows a higher, however, unproblematic rate. Note that the signal rates are determined as ratios of the number sensitivity over the summed T_{100} of the contributing GRBs. For the stacked searches, this sum is roughly 23 times higher than for the single source search, which, in consequence, explains their lower signal rates. The lower background rates for the stacked searches is due to the harder BDT score cut.

The on-time datasets for the various spectra contain several events that are coincident with observed GRB gamma emission. The number of expected events from background and signal simulation, N^{expected} , the number of events coincident with gamma emission, $N^{\text{on-time}}$, and the number of events that are qualified as signal-like, $N^{\text{signal-like}}$, are also given in table 7.8. However, in no case, the total likelihood ratio r_{tot} exceeds 0.23; thus the likelihood of having a signal event is always smaller than that for background, i.e. none of the events is classified as signal-like. A summary of the on-time events as well as a detailed description of the most interesting on-time events can be found in the following section.

Table 7.8: On-time rates and event counts. Give are as well the signal rate, the expected event count from background and signal simulation and the number of events that are qualified by the likelihood PDF ratio as signal-like.

Spectrum	$R^{\text{on-time}}$ [µHz]	<i>R</i> ^{signal} [µHz]	N ^{expected}	N ^{on-time}	N ^{signal-like}
E-2	381(15)	637(10)	6.52(16)	11	0
600	389(16)	702(4)	6.98(13)	9	0
100	484(17)	889(2)	8.79(12)	14	0
100npc	544(19)	915(2)	9.34(13)	16	0
600single	2921(43)	14383(56)	4.75(3)	1	0

7.4.1 On-Time Events

Although none of the observed on-time events is qualified as signal event, some of them show signal-like behavior in one or more of the separated likelihood ratios for space, time and energy r_{space} , r_{time} and r_{energy} , respectively. Therefore they will be investigated more closely further below. Table 7.9 gives information on the two most significant events for each of the spectra. The on-time events found for the $\Gamma100$ and $\Gamma100$ npc models are the same events with slightly different likelihood ratios in space and energy. While the likelihood ratios for time basically remains unchanged, the different BDTs are able to change the background slightly, so that the values differ for the space and energy likelihood ratio. The latter gets modified additionally by the different weights.

The two most interesting on-time events – the one found by the single source search and the one with the overall highest likelihood ratio – are described in more detail in dedicated paragraphs further below. None of those events nor one of the less significant ones that can be found in appendix F, is coincident with the five most significant ones found by a high-energy muon neutrino northern hemisphere search [168].

Table 7.9: The most significant on-time events and the corresponding GRBs. The IceCube run number, the GRB name, the identification number of the event as well as the GRB's T_{100} and various likelihood reconstruction parameters are shown. The latter includes the space angle deviation $\Delta\Omega$ between the GRB's and the event's directions as well as the time difference $\Delta t = t_{\text{GRB, start}} - t_{\text{event}}$.

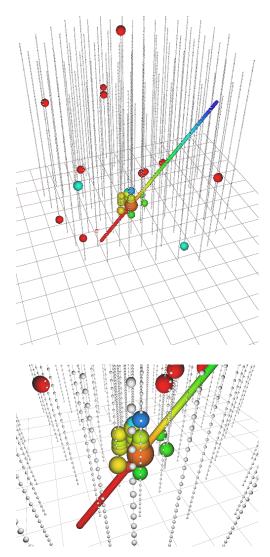
Spectrum	Run	GRB	T ₁₀₀ [s]	$\Delta\Omega[^{\circ}]$	Δt [s]	E [GeV]	
		Event		r _{space}	r _{time}	r _{energy}	r _{tot}
E^{-2}	120182	120522B	28.16	127.91	-30.33	34.57	
		14679138		0.20	1.44	0.36	0.016
	120914	121108A	138.13	42.22	-39.40	12.29	
		39065122		1.22	0.75	0.27	0.038
600	120710	120923A	29.57	96.80	51.18	79.57	
		54319615		0.44	1.97	1.31	0.119
	122111	130327A	10.00	83.38	7.57	224.01	
		22982658		0.59	2.57	1.47	0.233
100	120668	120914A	10.24	54.35	-5.08	7.11	
		54245113		0.73	2.27	0.96	0.120
	120977	121118A	33.80	66.75	62.52	14.10	
		10398811		0.99	1.59	1.15	0.137
100npc	120668	120914A	10.24	54.35	-5.08	7.11	
_		54245113		0.76	2.27	0.10	0.122
	120977	121118A	33.80	66.75	62.52	14.10	
		10398811		1.03	1.59	1.10	0.127
600single	122252	130427A	274.55	134.07	176.44	41.32	
		39978326		0.002	1.47	0.79	0.001

Single Source Search On-time Event: A detailed list with event and GRB information can be found in table 7.10. The event itself occurs about 3 min into the GRBs T_{100} , however, the event shows an angular separation to the GRB of about 130°, which makes this on-time event an off-source event. From the event display in table 7.10, the signature does not give clear evidence of a track or a cascade. The respective angular separation from the events Millipede reconstruction towards the GRB is only 30°, pointing closer to GRB than the Monopod reconstructed cascade. As no assumption can be made concerning the event's

signature, Monopod has to be used. However, this points out how important particle identification would be for low neutrino energies.

Table 7.10: Summary of the single source search on-time event and the related GRB. Early hits in the event display are color-coded in red, later hits in blue. The same coding applies for the Millipede reconstructed track. The bubbles' size is proportional to the deposited charge. The Monopod reconstructed cascade is not shown here for simplicity, but its vertex is closely located to the central orange bubble.

GRB information:	
GRB	130427A
Start Time	2013-04-27 07:47:06
T_{100}	274.55 s
Zenith	117.62°
Azimuth	249.13°
Event information:	
Event Time	2013-04-27 07:50:02
EventID	39978326
RunNumber	122252
Monopod Energy	41.32 GeV
Monopod Zen	89.72°
Monopod Azi	108.17°
Millipede Zen	131.11°
Millipede Azi	282.58°
Combined informa	tion:
Δt	00:02:56
$\Delta \Omega$ Monopod	134.07°
$\Delta \Omega$ Millipede	30.63°
Likelihood informa	ution:
Space PDF ratio	0.002
Time PDF ratio	1.471
Energy PDF ratio	0.788
Total PDF ratio	0.001

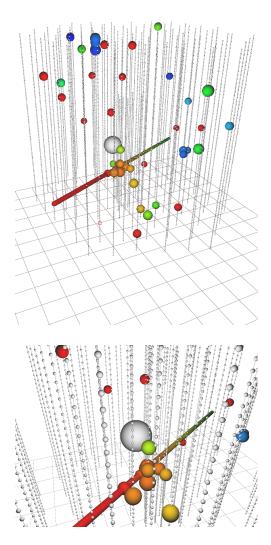


Overall Most Signal-like On-time Event: A detailed list with event and GRB information can be found in table 7.11. The event's total likelihood ratio of 0.23 is the highest ratio observed for all the investigated models. The event has been found by the $\Gamma600$ stacked search. Comparing to the single source on-time event, its time PDF ratio value is higher as the GRB is much shorter. The Monopod angular separation is also much smaller, which leads

to a larger space PDF value. Furthermore, the Millipede and Monopod reconstruction deliver rather similar values in this case.

Table 7.11: Summary of the on-time event with the overall highest total PDF ratio and the related GRB. Early hits in the event display are color-coded in red, later hits in blue. The same color-coding applies for the millipede reconstructed track. The Monopod reconstructed cascade vertex is shown as light gray bubble.

GRB information:	
GRB	130327A
Start Time	2013-03-27 01:47:30
T_{100}	10.0 s
Zenith	145.71°
Azimuth	209.21°
Event information:	
Event Time	2013-03-27 01:47:37
EventID	22982658
RunNumber	122111
Monopod Energy	224.01 GeV
Monopod Zen	86.99°
Monopod Azi	282.85°
Millipede Zen	115.85°
Millipede Azi	56.60°
Combined informa	tion:
Δt	0:00:08
$\Delta \Omega$ Monopod	83.38°
$\Delta\Omega$ Millipede	95.16°
Likelihood informa	ution:
Space PDF ratio	0.585
Time PDF ratio	2.567
Energy PDF ratio	1.468
Total PDF ratio	0.233



7.4.2 Determination of Upper Limits

From the likelihood PDF ratios the test statistic value T is calculated as described in equation 7.12. As the likelihood does not qualify any on-time event as signal-like, the respective test statistic, consequently, equals to zero for all of them.

The results, however, will be used to set *upper limits* on the number flux for the various models. The upper limit at 90% C.L. is defined as the lowest flux needed to obtain a test statistic value $T > T_{obs}$ in 90% of all trials. Sensitivity, evidence and discovery potential as well as the upper limit are shown for the Γ 600 stacked search as an example in figure 7.29.

The upper limits for all investigated models can be found in table 7.12. Note that the single source search has a lower upper limit of $\Phi_{upper limit}^{90\% \text{ C.L.}} = 8.3 \text{ cm}^{-2}$ compared to the corresponding stacked search with an upper limit of $\Phi_{upper limit}^{90\% \text{ C.L.}} = 13.9 \text{ cm}^{-2}$. Possible explanations are that, firstly, for the single source search a softer BDT cut was applied and secondly, for the stacked searches, there was no individual BDT score optimization applied for each contributing GRB.

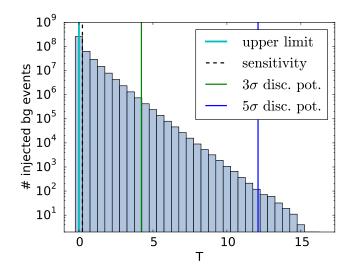


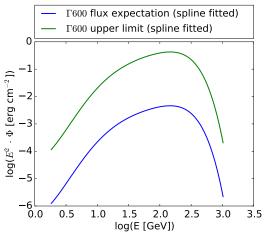
Figure 7.29: Exemplary distribution of the test statistic *T* for the Γ 600 spectrum final level, generated by throwing 10^8 trials. Sensitivity, evidence and discovery potential as well as the upper limit, resulting from an observed test statistic of *T* = 0.0, are marked by lines.

Table 7.12: Resulting parameters for the different spectra after evaluation of the on-time samples. Due to the rounding mentioned in footnote 86, section 7.3.3 the upper limits are numerically equal to the corresponding sensitivities.

Spectrum	N ^{on-time}	N ^{signal-like}	T-value	$\Phi_{\text{upper limit}}^{90\% \text{ C.L.}} [\text{cm}^{-2}] \\ \left(= \Phi_{\text{sens, sys}}^{90\% \text{ C.L.}}\right)$
E-2	11	0	0.0	5.2
600	9	0	0.0	13.9
100	14	0	0.0	278.0
100npc	16	0	0.0	250.8
600single	1	0	0.0	8.3

Integrating the theoretically expected flux shown in figure 3.5 for the $\Gamma600$ model yields $\Phi = 0.08 \text{ cm}^{-2}$. This is a factor 100 lower than the upper limit set on the single source neutrino flux. A comparison of the expectation from theory and the experimentally determined upper limit is shown in figure 7.30. The flux from theory was determined for a GRB at a redshift of z = 0.1; for GRB130427A a redshift of z = 0.34 was reported [150, 151]. Taking this into account and assuming the expected flux to be a quadratic function of distance and a linear function of E_{iso} , a finding would be possible if the GRB was either ten times stronger or about three times less distant. Although this work can neither confirm nor exclude a neutrino flux from GRB130427A, it could be shown that the all-flavor approach gives a strong tool that gets close to the verge of a detection or exclusion for this highly gamma-luminous GRB.

The upper limits set on the neutrino flux in the stacked searches are shown as function of the hardness of the respective models in figure 7.31. While the inclusion of the additional neutron-proton converter component lowers the upper limit on the number flux in the $\Gamma 100$ model by 10%, a higher Lorentz factor of $\Gamma = 600$ yields a decrease by a factor of 20. A detailed analysis of the upper limits as function of the Lorentz factor was, however, beyond the scope of this work, but could, in principle, be conducted with additional models supplied by the authors [169].



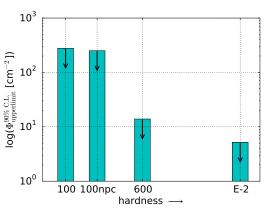


Figure 7.30: Upper limit on the neutrino flux for the Γ 600 single source search (green line). The integral of the upper limit is about a factor 100 larger than that of the expectation from theory (see section 3.1.2; blue line).

Figure 7.31: Upper limits as function of the hardness of the spectra investigated in the stacked searches. The hardness is proportional to the ratio of the respective maximal energy over the E^{-2} maximal energy. Arrows point towards the region that is not excluded by the upper limit.

7.4.3 SNEWS Coincidence Search

In search for a possible connection of GRBs and supernovae, a coincidence search between the on-time events found by the analysis described above and the high-significance events detected by SnDaq in the corresponding data-taking season was conducted. Thereby, the highest SN significance within a ± 2 hr-window around each GRB's starting time, was determined. The overall most-significant SN candidate has a significance of $\xi = 7.32$; the respective muon corrected significance is estimated⁸⁷ to be about $\xi' = 3.44$. The SNEWS alert was reported 1:19:29 hrs after GRB120522B in the 4 s binning⁸⁸. The observed gamma-ray duration was, however, only $T_{100} = 28.16$ s.

Within ± 30 days around the candidate fourteen alerts with $\xi \ge 7.32$ have been reported. The respective probability to detect at least one alert with $\xi \ge 7.32$ within ± 2 hrs around the candidate results therefore amounts to 4%. Following Poissonian statistics, this would be equivalent to a rather weak exclusion of a random coincidence with about 1.8σ . Taking into

⁸⁷The muon correction factor ξ'/ξ was here estimated to be of 2.13, the mean value in a seasonally corresponding period from March to July 2016.

⁸⁸As taken from the SNEWS monitoring website http://butler.physik.uni-mainz.de/icecube-snews-monitoring/h tml/snews_i3_sn.html accessed on March 31st, 2017.

account that the distribution is not Poissonian but broadened by at least a factor 1.4 [115], this is further reduced. However, this analysis provides the first tool to investigate the GRB-SNe subclass by taking the results of both the individual SN and GRB search into account.

CONCLUSION AND OUTLOOK

With the accomplished detection of an astrophysical neutrino flux, the next major challenge that IceCube faces is the detection of the respective sources. In order to increase the number of potential candidates, the low-energy regime has come more and more into focus. The most gamma-luminous astrophysical events that are expected to provide a low-energy neutrino flux origin from supernovae and gamma-ray bursts. A possible connection of both sources is predicted by the collapsar model in form of the GRB-SNe subclass, where Black Hole forming SNe are accompanied by a GRB breaking out of the infalling SNe progenitor material. This works aims for the improvement of existing and the exploration of new techniques to detect low-energy neutrinos for the SN and GRB source classes and, in particular, for the GRB-SNe subclass.

To improve the capabilities of supernovae detection, the likelihood algorithm was extended by an efficient atmospheric muon subtraction algorithm that successfully suppresses the influence of a major background for neutrino detection with IceCube. Using this technique, the detection probability for SNe in the Magellanic Clouds was improved by a factor of six. This is, in particular, important for SNe from low-mass progenitors; for high-mass models, e.g. describing Black Hole formation, the predicted significances are already detectable with essentially 100 % if they occur within our Galaxy. As those models provide theoretical candidates for GRB-SNe, the currently most stringent upper limit on the number of supernovae in our Galaxy was improved by a factor of two to $N_{upper limit}/yr = 0.47 \text{ yr}^{-1}$ at 90% C.L.

To search for GRBs emitting low energetic neutrinos produced by the inelastic collision model, an explorative analysis was performed based on existing and well-defined event selections. This work is the first analysis that tests a low-energy and therefore an all-flavor approach to a GRB neutrino search with IceCube. Starting with several noise-reducing preselection cuts, a dataset was produced that later-on was more refined by the usage of machinelearning algorithms. The score of those Boosted Decision Trees was optimized to achieve the best sensitivity. The consequently determined effective areas show that this work – and thus the all-flavor approach – is beneficial in comparison to previous muon flavor only analyses. This work yields a factor of two higher effective areas at 100 GeV and a factor of four higher effective areas at about 200 GeV. At higher energies it also connects smoothly to the results of previous analyses. As none of the observed on-time event is qualified as signal-like, upper limits are given as result of the search for various neutrino emission models. The investigation of the different models in the stacked shows that the upper limit depends on the hardness of the spectrum, such that harder spectra go along with lower upper limits. Thereby, a factor of six higher Lorentz factor yields a 200 times lower upper limit than the inclusion of the neutron-proton converter component. The single source search for neutrino emission from the high-gamma luminous GRB130427A is almost at the verge of detection or exclusion. The first upper limit on its number flux was set by this work to $\Phi_{upper limit} = 8.3 \text{ events/cm}^2$ at 90% C.L.

The above mentioned analysis methods for GRBs and SNe are quite distinct in their analysis procedure. Particularly interesting is the subclass of GRB-SNe for which a coincidence analysis was conducted, searching for correlated high-significance SNe alerts and events ontime with GRB emission. Assuming Poissonian statistics, a random coincidence between the highest significance of a supernova candidate in one year of data and the respective GRB can be excluded with 1.8σ . Although this is a rather weak exclusion, the underlying analysis provides a first GRB-SNe analysis tool for IceCube in the low-energy regime that can easily extended to take more data across multiple years into account.

This work as well as several other low-energy analyses clearly show that low-energy neutrino searches are a very promising tool for IceCube/DeepCore. However, the existing methods can be improved further by several refinements. For SnDaq, the main technical goal is to keep the uptime stable at the current high level of 99.79 % around-the-clock, if not improve on that even more. A second goal is to extend the collaboration with other experiments, i.a. the AMON alert network and the gravitational wave community. Additionally, an implementation of a *Bayesian-Block* analysis [170] that tries to find an optimal segmentation of the data into blocks of variable width is currently under investigation as alternative to the likelihood analysis in predefined bin widths.

Several improvements on the GRB analysis have been identified within this work but an implementation was beyond the scope of this thesis. They include the usage of more refined reconstruction tools as e.g. a hybrid reconstruction, which takes the initial hadronic cascade and the leptonic signatures into account. In this context also the identification of hadronic and electromagnetic cascades, as currently investigated in a dark matter search, is highly anticipated. Additional improvements are provided by better understanding of various detector aspects including noise behavior and of the Antarctic ice. The latter improvements are already partly available and the respective datasets are already in production. In order to learn more about the dependency of the upper limits on the spectral hardness, a detailed study with various Lorentz factors could be conducted.

For both kinds of searches presented in this work, multi-year analyses should be conducted. Especially for the GRB search, four more years of pulse-based data are available, eventually yielding a factor two improvement in sensitivity. Finally, both analyses are expected to profit from the planned successor PINGU/IceCube-Gen2 that will lower the energy threshold even more as it is more densely instrumented which should yield a substantially better particle identification at the relevant energies.

A SNDAQ RELEASES

The table below holds a summarizing description of the releases published and installed on SPS within the period, in which the author of this work was main or co-responsible of SnDaq.

Name	Release Date	Most Import Features (as taken from changelog ⁸⁹)
Hounskull	2012-01-20	Lightcurve displayed on I3Live Corrected startup artifacts
Galea	2012-07-02	Scaler overflow handling 2ms data transfer via SPADE for fast analysis Sn alert mail forwarding by I3Live
Morion1	2013-01-24	SnDaq installation and start via fabric script <i>fab.py</i> SnDaq communication all through I3Live via ZMQ Control script <i>checkSnDaq.py</i> on <i>expcont</i> Logging redesigned, including different levels SnDaq supports HitSpooling requests for all time ranges Fixed various sources of crashes (Valgrind identified) Differences between SPTS and SPS removed
Morion2	2013-02-14	<i>fab.py</i> now supports installation of specific revisions Raw files will be stored for 24 hours <i>checkSnDaq.py</i> logs to I3Live web pages
Kabuto1	2013-11-12	Added all remaining moni2.0 quantities <i>fab.py</i> supports "stage" and "deploy" to any target server Leap second support based on a NIST file ⁹⁰ redesign of SnDaq's time-class
Kabuto2	2013-12-13	Moni2.0 10 min quantities sent during startup and shutdown
Kabuto3	2014-04-15	Implemented fixes for raw data gaps Implemented consistency check for invalid timestamps in raw data header

Table A.1: SnDaq Releases

Kabuto4	2014-06-27	Minor bug fixes
Kabuto5	2014-07-08	First implementation of online muon subtraction
Kabuto6	2014-07-11	Minor bug fixes
Beer_Trooper	2014-07-25	Muon subtraction implemented for all binnings
Beer_Trooper2	2014-07-28	Missing pDaq trigger data handling
Beer_Trooper3	2014-07-31	Improved pDaq trigger data timestamp handling
Beer_Trooper4	2014-08-15	Implemented workaround for SnDaq crashes on sending alerts before writing data to file (also fixed the underlying bug)
Beer_Trooper5	2014-09-02	Added muon-corrected significance to alert SMS
Beer_Trooper6	(not installed)	Implemented check on minimum pDaq trigger rate
Beer_Trooper7	2014-10-23	Increased pDaq trigger data period to stabilize muon subtraction fits
Beer_Trooper8	2015-01-27	SnDaq supports ZMQ3
Beer_Trooper9	2015-03-03	Minor bug fixes
Beer_TrooperX	(not installed)	Improved fabric for online muon subtraction Replaced RMS with the more stable MAD in online muon subtraction
Beer_TrooperXI	2015-08-26	Added muon-corrected alert handling

⁸⁹The *changelogs* are the release descriptions stored along with the release in the version control system. ⁹⁰The *National Institute of Standards and Technology (NIST)* provides a table with all the leap seconds inserted in the current year.

Valgrind output first testrun

The output listed below is that of the series run from 15th to 25th of October 2012 for an example run called with

```
valgrind --track-origins=yes --leak-check=full --error-limit=no
--suppressions=$R00TSYS/etc/valgrind-root.supp ./bin/sni3dag -r
```

where the last option suppresses the information about memory leaks that are intentionally caused by the ROOT software. As can be seen below the conditional jump is caused within the external *Extensible Markup Language (XML)* libraries. The other ones are either uncritical ("0 bytes lost"), caused by the external ROOT software ("by 0x500ED4C: TString::Replace") or in need to be investigated further ("at 0x4C2AC27: operator new[](unsigned long)").

```
==27655== Memcheck, a memory error detector
 ==27655== Copyright (C) 2002-2011, and GNU GPL'd, by Julian Seward et al.
==27655== Using Valgrind-3.7.0 and LibVEX; rerun with -h for copyright info
==27655== Command: ./bin/sni3daq -r
==27655== Parent PID: 22455
 ==27655==
==2/r655== Conditional jump or move depends on uninitialised value(s)
==27655== at 0x71564E0: inflateReset2 (in /lib/x86_64-linux-gnu/libz.so.1.2.3.4)
==27655== by 0x71565D8: inflateInit2_ (in /lib/x86_64-linux-gnu/libz.so.1.2.3.4)
==27655== by 0x9ECEBE5: ??? (in /lib/x86_64-linux-gnu/libz.so.1.2.3.4)
==27655== by 0x9ECEBE5: ??? (in /lib/x86_64-linux-gnu/libz.so.1.2.3.4)
                                by 0x9ECE8E5: {?? (In /usr/iib/x86_04-inux-gnu/iixml2.s0.2/.08)
0 x99ECF011: __xmlParserInputBufferCreateFilename (in /usr/lib/x86_64-linux-gnu/libxml2.so.2.7.8)
by 0x9EA42B1: xmlNewInputFromFile (in /usr/lib/x86_64-linux-gnu/libxml2.so.2.7.8)
by 0x9EB7B35: xmlCreateURLParserCtxt (in /usr/lib/x86_64-linux-gnu/libxml2.so.2.7.8)
by 0x9EB4C5: xmlSAVParseFileWithData (in /usr/lib/x86_64-linux-gnu/libxml2.so.2.7.8)
by 0x641FC2A: Sni3DaqConfigXmlParser::init(int, char const*, char const*, char const*)
 ==27655==
 ==27655==
 ==27655==
 ==27655==
 ==27655==
                                   (Sni3DaqConfigXmlParser.C:471)
                           by 0x40DA81: Sni3Daq::init(int) (sni3daq.C:229)
by 0x4067AE: main (sni3daq.C:1349)
Uninitialised value was created by a heap allocation
==27655==
==27655==
==27655==
                                 http://difecture.us/science/science/science/science/science/science/science/science/science/science/science/science/science/science/science/science/science/science/science/science/science/science/science/science/science/science/science/science/science/science/science/science/science/science/science/science/science/science/science/science/science/science/science/science/science/science/science/science/science/science/science/science/science/science/science/science/science/science/science/science/science/science/science/science/science/science/science/science/science/science/science/science/science/science/science/science/science/science/science/science/science/science/science/science/science/science/science/science/science/science/science/science/science/science/science/science/science/science/science/science/science/science/science/science/science/science/science/science/science/science/science/science/science/science/science/science/science/science/science/science/science/science/science/science/science/science/science/science/science/science/science/science/science/science/science/science/science/science/science/science/science/science/science/science/science/science/science/science/science/science/science/science/science/science/science/science/science/science/science/science/science/science/science/science/science/science/science/science/science/science/science/science/science/science/science/science/science/science/science/science/science/science/science/science/science/science/science/science/science/science/science/science/science/science/science/science/science/science/science/science/science/science/science/science/science/science/science/science/science/science/science/science/science/science/science/science/science/science/science/science/science/science/science/science/science/science/science/science/science/science/science/science/science/science/science/science/science/science/science/science/science/science/science/science/science/science/science/science/science/science/science/science/scien
 ==27655==
 ==27655==
 ==27655==
 ==27655==
 ==27655==
 ==27655==
 ==27655==
                                 by 0x9EB7B35: xmlCreateURLParserCtxt (in /usr/lib/x86_64-linux-gnu/libxml2.so.2.7.8)
by 0x9EBD4C5: xmlSAXParseFileWithData (in /usr/lib/x86_64-linux-gnu/libxml2.so.2.7.8)
 ==27655==
 ==27655==
                                  by 0x641FC2A: Sni3DaqConfigXmlParser::init(int, char const*, char const*, char const*)
                                   (Sni3DagConfigXmlParser.C:471)
                                 by 0x40DA81: Sni3Daq::init(int) (sni3daq.C:229)
by 0x4067AE: main (sni3daq.C:1349)
==27655==
 ==27655==
 ==27655==
 ==27655== Warning: set address range perms: large range [0x395a5040, 0x16ce9aa40) (undefined)
 ==27655== Warning: set address range perms: large range [0x395a5030, 0x16ce9aa50) (noaccess)
 ==27655==
 ==27655== HEAP SUMMARY:
 ==27655==
                                     in use at exit: 5,478,977 bytes in 54,908 blocks
 ==27655==
                               total heap usage: 9,593,099 allocs, 9,538,191 frees, 8,812,737,702 bytes allocated
 ==27655==
 ==27655== 0 bytes in 1 blocks are definitely lost in loss record 1 of 38,577
                                   at 0x4C2AC27: operator new[](unsigned long) (in /usr/lib/valgrind/vgpreload_memcheck-amd64-linux.so)
  ==27655==
 ==27655==
                                 by 0x63F29F1: Sni3SicoAnalysis::gualifyAllChannels() (Sni3SicoAnalysis.C:761)
 ==27655==
                                  by 0x63EF45C: Sni3SicoAnalysis::DoAnalysis() (Sni3SicoAnalysis.C:220)
                                 by 0x63E7D0E: Sni3DataArray::triggerAllDataConsumers() (Sni3DataArray.C:186)
by 0x63F4951: Sni3DataScaler::DoAnalysis() (Sni3DataScaler.C:117)
 ==27655==
  ==27655==
                                 by 0x63E7D0E: Sni3DataArray::triggerAllDataConsumers() (Sni3DataArray.C:186)
by 0x63F4951: Sni3DataScaler::DoAnalysis() (Sni3DataScaler.C:117)
 ==27655==
 ==27655==
 ==27655==
                                 by 0x63E7D0E: Sni3DataArray::triggerAllDataConsumers() (Sni3DataArray.C:186)
```

```
==27655==
                       by 0x63E475B: I3Eval_t::fillAnalysisArray() (i3eval.C:214)
==27655==
                       by 0x4069EA: main (sni3daq.C:1371)
==27655==
==27655== 0 bytes in 1 blocks are definitely lost in loss record 2 of 38,577
                       at 0x4C2AC27: operator new[](unsigned long) (in /usr/lib/valgrind/vgpreload_memcheck-amd64-linux.so)
==27655==
==27655==
                       by 0x63F2A24: Sni3SicoAnalysis::qualifyAllChannels() (Sni3SicoAnalysis.C:763)
by 0x63EF45C: Sni3SicoAnalysis::DoAnalysis() (Sni3SicoAnalysis.C:220)
==27655==
                       by 0x63F7D0E: Sni3DataArray::triggerAllDataConsumers() (Sni3DataArray.C:186)
by 0x63F4951: Sni3DataScaler::DoAnalysis() (Sni3DataScaler.C:117)
==27655==
==27655==
==27655==
                       by 0x63E7D0E: Sni3DataArray::triggerAllDataConsumers() (Sni3DataArray.C:186)
                       by 0x63F4051: Sni3DataScaler::DoAnalysis() (Sni3DataScaler.Ct117)
by 0x63E7D0E: Sni3DataArray::triggerAllDataConsumers() (Sni3DataArray.C:186)
==27655==
==27655==
==27655==
                        by 0x63E475B: I3Eval_t::fillAnalysisArray() (i3eval.C:214)
==27655==
                       by 0x4069EA: main (sni3daq.C:1371)
==27655==
=27655== 96 bytes in 3 blocks are possibly lost in loss record 30,101 of 38,577
==27655== at 0x4C2AC27: operator new[](unsigned long) (in /usr/lib/valgrind/vgpreload_memcheck-amd64-linux.so)
==27655== by 0x500ED4C: TString::Replace(int, int, char const*, int)
                       by 0x500ED4C: lString::Replace(int, int, char const*, int)
(in /afs/physik.uni-mainz.de/opt/root-5.30.01_64/lib/libCore.so)
by 0x558ABDE: TStreamerInfo::Compile() (in /afs/physik.uni-mainz.de/opt/root-5.30.01_64/lib/libRIO.so)
by 0x959F8B0: TStreamerInfo::Build() (in /afs/physik.uni-mainz.de/opt/root-5.30.01_64/lib/libRIO.so)
by 0x95451E6: TBufferFile::WriteClassBuffer(TClass const*, void*)
==27655==
==27655==
==27655==
                       by 0x95451E6: TBufferFile::WriteClassBuffer(TClass const*, void*)
(in /afs/physik.uni-mainz.de/opt/root-5.30.01_64/lib/libRIO.so)
by 0x957E640: TKey::TKey(TObject const*, char const*, int, TDirectory*)
(in /afs/physik.uni-mainz.de/opt/root-5.30.01_64/lib/libRIO.so)
by 0x955D829: TFile::CreateKey(TDirectory*, TObject const*, char const*, int)
(in /afs/physik.uni-mainz.de/opt/root-5.30.01_64/lib/libRIO.so)
by 0x9552BF7: TDirectoryFile::WriteTObject(TObject const*, char const*, char const*, int)
(in /afs/physik.uni-mainz.de/opt/root-5.30.01_64/lib/libRIO.so)
by 0x94FE7D15: TObject::WriteTObject(TObject const*, char const*, char const*, int)
(in /afs/physik.uni-mainz.de/opt/root-5.30.01_64/lib/libRIO.so)
by 0x4FE7D15: TObject::Write(Char const*, int, int) const
==27655==
==27655==
==27655==
==27655==
                       by 0x40F405: Sni3Daq::stop(int) (sni3daq.C:471)
by 0x40F465: Sni3Daq::checkStop() (sni3daq.C:657)
by 0x406973: main (sni3daq.C:1359)
  =27655==
==27655==
==27655==
==27655==
==27655==
                  41,280 bytes in 1 blocks are definitely lost in loss record 38,549 of 38,577
                       at 0x4C2AC27: operator new[](unsigned long) (in /usr/lib/valgrind/vgpreload_memcheck-amd64-linux.so) by 0x63EFFBE: Sni3SicoAnalysis::InitSicoAnalysis(Sni3SicoAnalysis::Descriptor&) (Sni3SicoAnalysis.C:157)
==27655==
==27655==
                       by 0x63F01D5: Sni3SicoAnalysis::Sni3SicoAnalysis(Sni3SicoAnalysis::Descriptor&) (Sni3SicoAnalysis.C:12&)
by 0x412443: Sni3SicoAnalysis* Sni3Daq::initSni3
<Sni3SicoAnalysis, Sni3SicoAnalysis::Descriptor>(Sni3SicoAnalysis::Descriptor&) (sni3daq.C:169)
by 0x40E944: Sni3Daq::init(int) (sni3daq.C:398)
by 0x40E944: Sni3Daq::init(int) (sni3daq.C:398)
==27655==
==27655==
==27655==
==27655==
                       by 0x4067AE: main (sni3daq.C:1349)
==27655==
==27655== 41.280 bytes in 1 blocks are definitely lost in loss record 38.550 of 38.577
==27655==
                       at 0x4C2AC27: operator new[](unsigned long) (in /usr/lib/valgrind/vgpreload_memcheck-amd64-linux.so)
by 0x63EFFD9: Sni3SicoAnalysis::InitSicoAnalysis(Sni3SicoAnalysis::Descriptor&) (Sni3SicoAnalysis.C:158)
==27655==
                       by 0x63FF195: Shi3SicoAnalysis::Shi3SicoAnalysis(Shi3SicoAnalysis::Descriptor&) (Shi3SicoAnalysis(C:136)
by 0x63F61D5: Shi3SicoAnalysis::Shi3SicoAnalysis(Shi3SicoAnalysis::Descriptor&) (Shi3SicoAnalysis.C:128)
by 0x412443: Shi3SicoAnalysis* Shi3Daq::initShi3
<Shi3SicoAnalysis, Shi3SicoAnalysis::Descriptor>(Shi3SicoAnalysis::Descriptor&) (shi3daq.C:169)
by 0x40E944: Shi3Daq::init(int) (shi3daq.C:398)
==27655==
==27655==
==27655==
==27655==
                       by 0x4067AE: main (sni3daq.C:1349)
==27655==
=27655== 41,280 bytes in 1 blocks are definitely lost in loss record 38,551 of 38,577
==27655== at 0x4C2AC27: operator new[](unsigned long) (in /usr/lib/valgrind/vgpreload_memcheck-amd64-linux.so)
                       by 0x63EFFF4: Sni3SicoAnalysis::InitSicoAnalysis(Sni3SicoAnalysis::Descriptor&) (Sni3SicoAnalysis.C:159) by 0x63F01D5: Sni3SicoAnalysis::Sni3SicoAnalysis(Sni3SicoAnalysis::Descriptor&) (Sni3SicoAnalysis.C:128)
--27655--
==27655==
                       by 0x412443: Sni3SicoAnalysis* Sni3Baq::initSni3
<Sni3SicoAnalysis, Sni3SicoAnalysis::Descriptor</pre>(Sni3SicoAnalysis::Descriptor&) (sni3daq.C:169)
by 0x40E944: Sni3Daq::init(int) (sni3daq.C:398)
==27655==
==27655==
==27655==
                       by 0x4067AE: main (sni3daq.C:1349)
==27655==
==27655== 41,280 bytes in 1 blocks are definitely lost in loss record 38,552 of 38,577
                       at 0x4C2AC27: operator new[](unsigned long) (in /usr/lib/valgrind/vgpreload_memcheck-amd64-linux.so) by 0x63F000F: Sni3SicoAnalysis::InitSicoAnalysis(Sni3SicoAnalysis::Descriptor&) (Sni3SicoAnalysis.C:160)
==27655==
==27655==
                       by 0x63F01D5: Sni3SicoAnalysis::Sni3SicoAnalysis(Sni3SicoAnalysis::Descriptor&) (Sni3SicoAnalysis.C:128)
by 0x412443: Sni3SicoAnalysis* Sni3Daq::initSni3
==27655==
==27655==
                        <Sni3SicoAnalysis, Sni3SicoAnalysis::Descriptor>(Sni3SicoAnalysis::Descriptor&) (sni3daq.C:169)
                       by 0x40E944: Sni3Daq::init(int) (sni3daq.C:398)
by 0x4067AE: main (sni3daq.C:1349)
==27655==
==27655==
==27655==
==27655== LEAK SUMMARY:
==27655==
                        definitely lost: 165,120 bytes in 6 blocks
                       indirectly lost: 240 bytes in 10 blocks
possibly lost: 96 bytes in 3 blocks
==27655==
==27655==
=27655== still reachable: 4,159,055 bytes in 41,371 blocks
==27655== suppressed: 1,154,466 bytes in 13,518 blocks
==27655== Reachable blocks (those to which a pointer was found) are not shown.
==27655== To see them, rerun with: -leak-check=full -show-reachable=yes
==27655==
  =27655== For counts of detected and suppressed errors, rerun with:
==27655== ERROR SUMMARY: 10 errors from 8 contexts (suppressed: 136 from 136)
```

<\pre>

GRB CATALOG

Table C.1 shows the most important parameters – as provided by GRBWeb – for the GRBs investigated within this work.

Table C.1: GRB catalog as taken from GRBWeb. Shown are, right ascension *RA* and declination Decl – given in degree (J2000)⁹¹–, the angular uncertainty ERR, several times limiting the GRB flux duration, the fluence and the IceCube internal run number.

Name	RA	Decl	ERR	T_{100}	T_{90}	Date	T1	T2	Fluence	RunNumber
	[deg]	[deg]	[deg]	[s]	[s]	[UTC]	[s]	[s]	[erg cm ⁻²]	
120519A	178.366	22.407	0.634	5.7	0.72	2012-05-19 17:18:14.64	-0.5	5.2	3.7E-6	120172
120520A	45.86	35.28	8.3	5.76	5.76	2012-05-20 22:46:24.663	-4.74	1.02	4.409E-7	120176
120521C	214.286	42.145	0.0003	32.87	26.7	2012-05-21 23:22:07.0	-1.03	31.84	1.1E-6	120181
120522B	56.07	54.85	2.02	28.16	28.16	2012-05-22 08:39:16.839	-11.52	16.64	9.324E-6	120182
120528A	295.13	6.5	5.98	16.39	16.39	2012-05-28 10:36:00.217	-0.77	15.62	3.792E-6	120102
120520A	175.96	78.83	3.27	77.06	77.06	2012-05-20 10:50:00:217	0.77	77.06	7.173E-6	120202
120530A 120531A	290.4	1.22	11.03	25.35	25.35	2012-05-31 09:26:38.365	-2.82	22.53	9.099E-7	120207
120531A 120603A	198.794	4.326	0.6427	5.36	0.38	2012-06-03 10:32:09.854	-0.06	5.3	1.0E-6	120241
120605A	243.61	41.51	2.62	18.11	18.11	2012-06-05 10:52:15.904	-0.64	17.47	3.253E-6	120260
120608B	313.26	12.64	5.08	24.84	24.84	2012-06-08 18:38:33.035	-14.34	10.5	3.174E-6	120276
120609A	67.32	13	7.54	1.79	1.79	2012-06-09 13:54:35.623	-0.77	1.02	4.196E-7	120303
120612B	211.88	34.56	7.08	63.24	63.24	2012-06-12 16:19:45.548	-10.5	52.74	2.062E-6	120313
120614A	312.73	65.16	0.1216	45	-1	2012-06-14 05:49:10.0	0	45	1.0E-5	120318
120616A	79.69	56.44	8.54	0.05	0.05	2012-06-16 15:06:50.639	-0.05	0	2.576E-7	120329
120617A	22.309	33.804	0.251	0.5	0.5	2012-06-17 15:02:47.025	0	0.5	2.1E-6	120334
120618A	77.31	75.85	2.59	17.6	17.6	2012-06-18 03:03:49.875	-0.13	17.47	5.580E-6	120336
120624A	4.773	7.167	0.4427	3.58	0.3	2012-06-24 07:24:22.982	0	3.58	6.5E-6	120376
120624B	170.886	8.933	0.0101	309.952	274	2012-06-24 22:19:30.985	-20	289.952	1.916E-4	120378
120625A	51.26	51.07	1.17	7.43	7.43	2012-06-25 02:50:46.037	-0.26	7.17	1.022E-5	120379
120630A	352.3	42.495	0.0274	0.7	0.6	2012-06-30 23:17:33.0	-0.1	0.6	6.1E-8	120400
120702A	227.8	36.76	8.48	35.07	35.07	2012-07-02 21:23:19.171	-1.02	34.05	1.598E-6	120406
120703B	69.49	34.74	2.6	64.51	64.51	2012-07-03 10:01:11.688	-0.51	64	1.108E-5	120408
120703C	210.51	46.26	5.15	77.57	77.57	2012-07-03 11:56:56.87	-2.05	75.52	2.597E-6	120408
120711B	331.71	59.996	0.0324	63.5	60	2012-07-11 03:11:02.58	-12.1	51.4	5.6E-7	120431
120713A	161.68	40.66	16.71	13.82	13.82	2012-07-13 05:25:29.139	-3.07	10.75	1.130E-6	120438
120715A	272.15	58.79	3.73	29.69	29.69	2012-07-15 05:25:25:15573	-4.86	24.83	2.195E-6	120438
120715A 120716A	313.089	9.558	0.1747	235.02	234.49	2012-07-16 17:05:03.908	-1.02	24.85	1.47E-5	120444
120716A 120716B	304.53	59.41	5.09	235.02	234.49	2012-07-16 13:51:02.134	-5.89	19.07	5.223E-6	120450
120710B 120722A		13.251	0.0004	24.90 47.8	42.4			47.5	1.2E-6	120430
	230.497					2012-07-22 12:53:26.0	-0.3			
120724A	245.18	3.508	0.0003	130	72.8	2012-07-24 06:39:02.0	-30	100	6.8E-7	120477
120727A	163.26	25.09	15.27	0.9	0.9	2012-07-27 08:29:39.081	-0.9	0	1.091E-7	120487
120727B	37.76	16.36	1	10.49	10.49	2012-07-27 16:20:19.529	-0.22	10.27	9.235E-6	120502
120729A	13.074	49.94	0.0003	105.02	71.5	2012-07-29 10:56:14.0	-3.08	101.94	5.1E-6	120508
120802A	44.842	13.768	0.0005	63.7	50	2012-08-02 08:00:51.0	-35.68	28.02	1.9E-6	120520
120803B	314.236	53.304	0.0003	51.83	37.5	2012-08-03 11:06:06.0	-2.67	49.16	2.5E-6	120524
120805A	216.538	5.825	0.0005	48	48.00	2012-08-05 21:28:09.0	-15.39	32.61	8.2E-7	120531
120806A	308.99	6.33	4.25	26.63	26.63	2012-08-06 00:10:08.866	-0.26	26.37	4.902E-6	120531
120811C	199.683	62.301	0.0003	52.6	26.8	2012-08-11 15:34:52.0	-9.7	42.9	3.0E-6	120548
120814A	26.19	22.45	3.71	0.89	0.89	2012-08-14 04:49:12.579	-0.38	0.51	3.831E-7	120556
120814B	90.57	33.13	10.68	0.19	0.19	2012-08-14 19:16:06.746	-0.19	0	1.284E-7	120558
120816B	341.155	2.156	2.51	0.768	0.768	2012-08-16 23:58:18.852	0	0.768	9.7E-5	120566
120819B	171.54	49.42	7.94	66.3	66.3	2012-08-19 01:08:26.765	-5.63	60.67	1.334E-6	120572
120822A	181.72	80.56	7.7	1.54	1.54	2012-08-22 15:03:56.399	-1.28	0.26	1.085E-7	120587
120824A	70.92	17.63	3	111.62	111.62	2012-08-24 14:16:00.734	-8.19	103.43	5.919E-6	120593
120830C	110.03	17.53	3.39	49.67	49.67	2012-08-30 16:51:36.68	-15.62	34.05	5.655E-6	120613
120905A	355.96	16.99	1.8	195.59	195.59	2012-09-05 15:46:21.166	-7.17	188.42	1.957E-5	120635
120911A	357.979	63.099	0.0003	28.58	22.02	2012-09-11 07:08:33.988	-4.48	24.1	2.34E-6	120656
120913A	146.4	26.959	0.0122	41.87	40.96	2012-09-13 20:18:22.887	-3.07	38.8	0.38E-8	120667
120914A	267.94	1.82	5.35	10.24	10.24	2012-09-14 03:26:42.114	-1.28	8.96	7.350E-7	120668
120916A	205.631	36.7	0.4953	56.19	26	2012-09-16 04:07:46.689	-2	54.19	1.95E-5	120679
120910A 120923A	303.795	6.221	0.0003	29.57	20	2012-09-23 05:16:06.0	-2.93	26.64	3.2E-7	120079
120925A 120926A	318.39	58.38	1.51	4.29	4.29		-2.93	3.65	2.478E-6	120710
120920A 120927A		0.416				2012-09-26 08:02:56.573			2.478E-0 2.6E-6	120720
	136.614		0.0002	78.98	43	2012-09-27 22:40:46.0	-37.94	41.04		
121005B	149.73	25.4	5.39	141.57	141.57	2012-10-05 08:09:12.865	0	141.57	5.169E-6	120772
121011A	260.215	41.11	0.0004	90.1	31	2012-10-11 11:15:30.264	-10	80.1	1.00E-5	120797
121011B	182.809	44.113	1.4943	2.5	0.35	2012-10-11 22:32:20.083	0	2.5	2.8E-6	120798
121012A	33.42	14.58	6.78	0.45	0.45	2012-10-12 17:22:16.386	-0.13	0.32	1.15E-6	120801
121019A	43.47	62.14	7.52	14.34	14.34	2012-10-19 05:35:09.226	-2.56	11.78	5.886E-7	120837

121025A	248.382	27.672	0.0006	20	-1	2012-10-25 07:46:30.0	0	20	1.0E-5	120856
121102B	258.47	14.09	12.15	2.05	2.05	2012-11-02 01:32:47.937	-1.54	0.51	5.672E-7	120880
121104A	72.14	14.08	4.05	59.13	59.13	2012-11-04 15:02:15.495	-1.02	58.11	4.446E-6	120888
121108A	83.194	54.474	0.0003	138.13	89	2012-11-08 17:47:39.0	-0.15	137.98	9.6E-7	120000
121100A	313.17	59.82	2.06	95.49	95.49	2012-11-13 13:02:43.531	1.54	97.03	2.685E-5	120714
										-
121117A	31.611	7.42	0.0001	158.6	30	2012-11-17 08:50:56.0	0	158.6	1.4E-6	120968
121117B	279.14	44.93	4.32	331.78	331.78	2012-11-17 00:25:37.726	-270.34	61.44	1.063E-5	120959
121118A	299.379	65.654	1.1443	33.8	33.8	2012-11-18 13:48:54.256	-0.26	33.54	6.777E-6	120977
121122A	35.262	45.139	3.7097	20.106	8.19	2012-11-22 21:14:52.546	0.51	20.616	5.46E-5	121038
121122B	52.67	46.47	12.89	8.7	8.7	2012-11-22 13:31:27.521	-1.28	7.42	8.146E-7	121037
121122C	355.45	6.34	2.66	125.44	125.44	2012-11-22 20:52:49.028	0	125.44	9.070E-6	121038
121122C	87.93	49.55	14.64	0.26	0.26	2012-11-24 14:32:07.299	-0.13	0.13	5.660E-8	121050
121124A 121125A		55.313	0.0003	83.95	52.2					
	228.528					2012-11-25 08:32:27.0	-6.31	77.64	9.5E-6	121063
121125B	177.53	38.54	5.24	12.86	12.86	2012-11-25 11:14:47.49	-2.3	10.56	8.568E-7	121063
121128A	300.6	54.3	0.0003	41.69	23.3	2012-11-28 05:05:37.0	0	41.69	1.04E-5	121149
121202A	256.797	23.948	0.0002	23.02	20.1	2012-12-02 04:20:05.0	-2.18	20.84	2.0E-6	121225
121210A	202.54	17.77	8.25	12.8	12.8	2012-12-10 01:56:01.527	-1.54	11.26	2.024E-6	121288
121211A	195.533	30.149	0.0003	198.84	5.63	2012-12-11 13:47:03.59	-3.07	195.77	4.825E-7	121292
121211B	72.37	8.63	5.23	8.96	8.96	2012-12-11 16:41:02.769	-0.51	8.45	1.340E-6	121298
121212A	177.792	78.037	0.0003	10	10	2012-12-12 06:56:12.0	0	10	1.2E-7	121323
121220A	31.07	48.28	8.3	5.12	5.12	2012-12-20 07:28:13.239	-1.28	3.84	4.532E-7	121419
121220A 121221A		33.55	4.22	38.91	38.91	2012-12-20 07:28:15:259	-3.07	35.84	5.039E-6	121412
	214.26									
121223A	50.11	21.37	2.74	11.01	11.01	2012-12-23 07:11:19.812	0	11.01	7.017E-6	121436
130102A	311.423	49.818	0.0003	87.92	77.5	2013-01-02 18:10:53.0	12.51	100.43	7.2E-7	121506
130104A	174.09	25.92	2.44	26.37	26.37	2013-01-04 17:18:07.049	-1.79	24.58	5.668E-6	121511
130106A	66.67	29.74	4.99	11.26	11.26	2013-01-06 19:53:22.071	-2.56	8.7	1.586E-6	121543
130106B	28.76	63.38	1.87	70.4	70.4	2013-01-06 23:52:25.792	-1.02	69.38	1.543E-5	121545
130109A	17.45	19.24	3.72	8.96	8.96	2013-01-09 04:56:26.261	-3.58	5.38	2.535E-6	121579
130112A	236.03	52.19	4.93	35.33	35.33	2013-01-12 06:52:07.524	-29.7	5.63	2.614E-6	121627
130115A	171.09	22.62	2.78	13.57	13.57	2013-01-15 17:10:39.182	-3.84	9.73	2.718E-6	121678
130116A	38.24	15.75	29.85	66.82	66.82	2013-01-16 09:58:14.219	-4.1	62.72	9.271E-7	121680
130110A 130117A	341.24		6.17	78.85	78.85			80.64	,	121680
		2.81				2013-01-17 02:05:11.425	1.79		2.849E-6	
130118A	278.3	40.98	6.7	21.57	21.57	2013-01-18 11:33:29.36	-5.63	15.94	8.278E-7	121698
130122A	194.285	59.015	0.0003	80	64	2013-01-22 23:44:09.0	-12.6	67.4	7.4E-7	121746
130131A	171.126	48.076	0.0003	53.1	51.6	2013-01-31 13:56:22.0	-0.95	52.15	3.1E-7	121784
130131B	173.956	15.038	0.0003	4.65	4.30	2013-01-31 19:10:08.0	-0.28	4.37	3.4E-7	121784
130204A	105.64	41.92	7.07	0.19	0.19	2013-02-04 11:36:51.704	-0.13	0.06	2.809E-7	121829
130206B	269.1	49.43	2.4	11.27	11.27	2013-02-06 11:33:34.503	-4.61	6.66	7.163E-6	121835
130208A	181.6	50.93	4.67	41.47	41.47	2013-02-08 16:24:23.836	-1.02	40.45	2.255E-6	121844
130215A	43.486	13.387	0.0152	146.11	46.0	2013-02-15 01:31:25.437	-7	139.11	2.02E-5	121881
130215A 130215B	3.11	59.38	2.1	58.11	58.11	2013-02-15 01:51:25:457	6.91	65.02	2.149E-5	121884
130216A	67.901	14.67	0.0101	10.47	6.5	2013-02-16 22:15:24.0	-6.16	4.31	6.231E-6	121900
130216B	58.866	2.036	0.0152	15.29	15.29	2013-02-16 18:58:11.695	-6.27	9.02	4.8E-6	121899
130217A	96.72	6.8	8.19	14.84	14.84	2013-02-17 16:31:19.119	-11.26	3.58	1.100E-6	121903
130219A	303.73	40.83	1.21	118	96	2013-02-19 18:35:51.73	-2	116	3.18E-5	121912
130219C	211.6	12.22	16.68	1.54	1.54	2013-02-19 15:01:13.946	-1.09	0.45	2.027E-7	121912
130220A	306.2	31.74	1.14	6.4	6.4	2013-02-20 23:08:48.202	0.26	6.66	7.235E-6	121917
130224A	205.9	59.72	2.62	70.91	70.91	2013-02-24 08:53:02.377	-35.84	35.07	4.962E-6	121929
130228A	265.83	55.93	0.5	111.75	111.75	2013-02-28 02:40:02.166	-9.86	101.89	1.241E-5	121942
130304A	98.93	53.57	1.2	67.84	67.84	2013-03-04 09:49:53.099	0.83	68.67	3.701E-5	121942
130305A	116.774	52.037	0.0182	36.816	25.6	2013-03-05 11:39:11.369	1.28	38.096	5.7E-5	121996
130307A		22.998		0.38	0.38	2013-03-07 03:01:44.471	-0.06	0.32	1.43E-6	121990
	155.996		0.3643							
130307B	319.52	10.77	4.42	63.49	63.49	2013-03-07 05:42:19.325	-12.29	51.2	3.972E-6	122002
130314A	206.21	46.77	1.41	142.85	142.85	2013-03-14 03:31:16.299	1.54	144.39	1.460E-5	122046
130318A	200.74	8.12	9.94	137.99	137.99	2013-03-18 10:56:31.179	-2.82	135.17	3.407E-6	122062
130324A	255.43	0.05	6.03	37.76	37.76	2013-03-24 01:00:24.747	-6.27	31.49	1.904E-6	122101
130325B	30.44	62.06	16.14	0.64	0.64	2013-03-25 00:07:46.818	-0.06	0.58	5.656E-8	122105
130327A	92.039	55.715	0.0003	10	9.0	2013-03-27 01:47:34.0	-4.38	5.62	2.3E-7	122111
130331A	164.47	29.64	2.43	13.82	13.82	2013-03-31 13:35:44.87	-0.51	13.31	9.331E-6	122125
130404A	30.75	1.54	7.24	3.33	3.33	2013-04-04 10:15:40.052	-1.54	1.79	8.425E-7	122141
130404C	28.29	56.49	18.23	0.96	0.96	2013-04-04 21:02:11.029	-0.13	0.83	2.202E-7	122141
130404C	138.21	42.83	14.84	2.56	2.56	2013-04-06 08:29:36.58	-1.28	1.28	2.976E-7	122142
130400C 130407A					-1	2013-04-07 23:37:01.0	-1.28	25		122140
	248.1	10.51	0.0608	25					1.0E-5	
130407B	53.53	44.17	9.29	32	32.0	2013-04-07 19:12:43.057	-5.63	26.37	1.746E-6	122151
130408B	118.77	66.34	3.93	9.21	9.21	2013-04-08 15:40:22.855	-4.86	4.35	2.052E-6	122153
130409A	30.52	44.1	2.22	26.11	26.11	2013-04-09 23:01:59.658	0.26	26.37	7.871E-6	122160
130416A	99.28	24.7	14.34	3.08	3.08	2013-04-16 16:34:07.062	-2.82	0.26	2.807E-7	122183
130418A	149.037	13.667	0.0003	325.75	300	2013-04-18 19:00:53.0	-40.16	285.59	1.8E-6	122205
130419A	355.278	9.9	0.0263	129.42	75.7	2013-04-19 13:30:29.0	40.09	169.51	7.8E-7	122208
130420A	196.106	59.424	0.0003	209.6	123.5	2013-04-20 07:28:29.0	-19.7	189.9	1.4E-5	122212
130420B	183.128	54.391	0.0003	22.17	13.83	2013-04-20 12:56:32.988	-7.17	15	1.04E-7	122228
130420B 130427A	173.136	27.698	0.0005	274.55	162.83	2013-04-27 07:47:57.0	-51.05	223.5	1.975E-3	122220
130502B	66.648	71.098	0.093	37	27.392	2013-05-02 07:51:12.763	0	37	1.21E-4	122252
150502B	00.040	/1.004	0.095	51	21.372	2015-05-02 07.51.12.705	U	51	1.211-4	1222/4

⁹¹As the equatorial coordinate system is turning with the Earth's axis, a date has to be given additionally to the right ascension and declination. The commonly chosen *J2000* hereby refers to 12 p.m. on January 1st, 2000.

INITIAL EVENT SELECTION - ADDITIONAL PLOTS AND TABLES

In this chapter additional plots and tables are shown that provide details to the initial event selection.

D.1 BDT Discrimination Variable Distribution Plots

In this section, the plots for the BDT discrimination variables are shown. The GRB signal rates are shown for the Γ 600 spectrum as an example. The left plots depict the individual contributions while the sum of background simulations (sumMC) vs. experimental data is displayed on the right as well as the data/MC ratio.

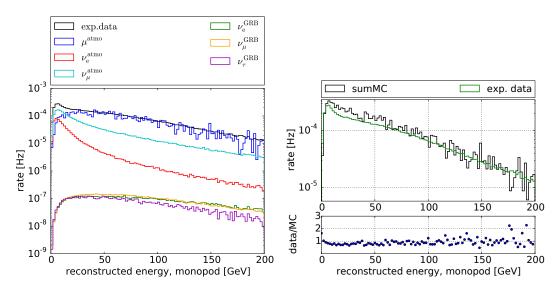


Figure D.1: Monopod reconstructed energy distribution on level5.

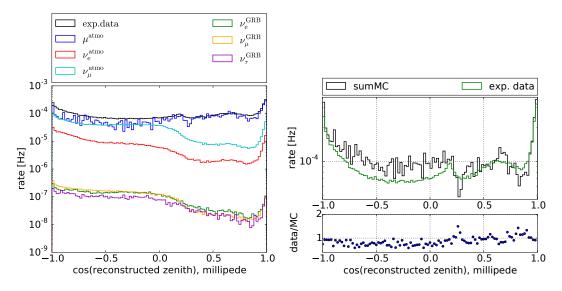


Figure D.2: Millipede reconstructed cosine(zenith) distribution on level5.

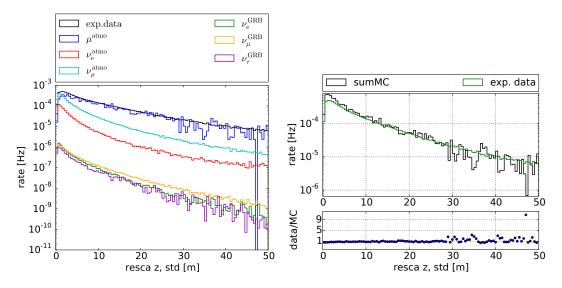


Figure D.3: Resca's z-coordinate distribution on level5.

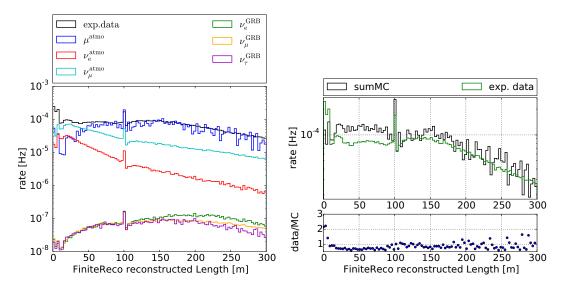


Figure D.4: FiniteReco length distribution on level5.

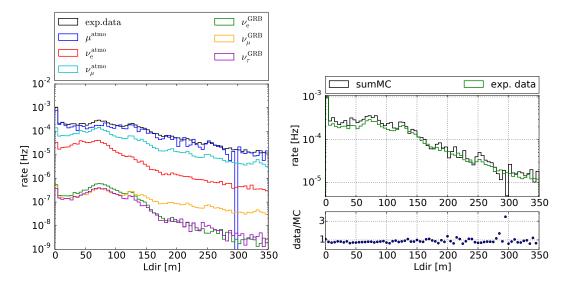


Figure D.5: Ldir distribution on level5.

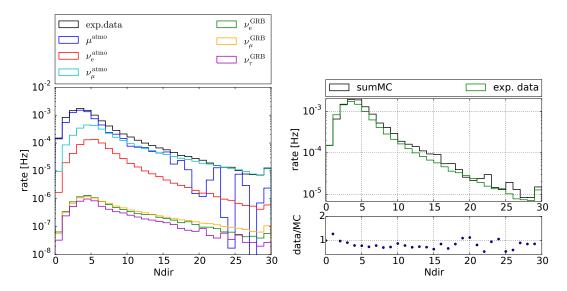


Figure D.6: Ndir distribution on level5.

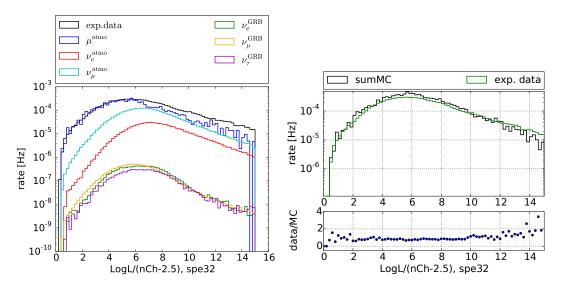


Figure D.7: rLogLSPE32 distributions on level5.

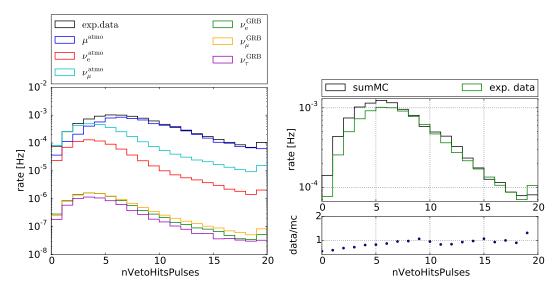
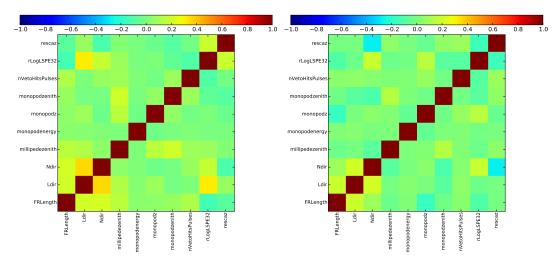


Figure D.8: nVetoHitsPulses distributions on level5.

D.2 BDT Performance Checks

In this section, the correlations, overtraining checks, efficiencies and BDT score distributions are summarized for various assumed spectra.



Correlation Plots:

Figure D.9: Correlation coefficients of the input parameters for a BDT trained for the E^{-2} spectrum. Off-time data is shown on the left plot and signal on the right. Except for the self-correlations and the correlation between Ldir and Ndir as well as a minor correlation between rLogLSPE32 and Ldir/Ndir, no unexpected correlation is observable.

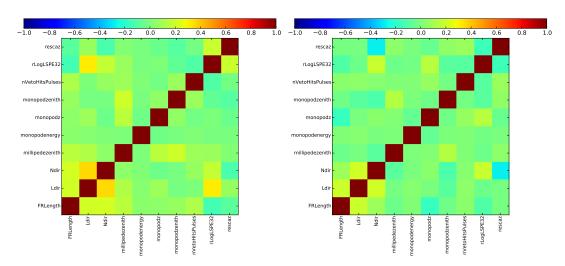


Figure D.10: Correlation coefficients of the input parameters for a BDT trained for the $\Gamma 100$ spectrum. Off-time data is shown on the left plot and signal on the right. Except for the self-correlations and the correlation between Ldir and Ndir as well as a minor correlation between rLogLSPE32 and Ldir/Ndir, no unexpected correlation is observable.

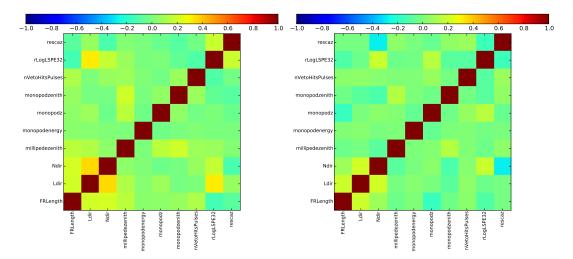


Figure D.11: Correlation coefficients of the input parameters for a BDT trained for the Γ 100npc spectrum. Off-time data is shown on the left plot and signal on the right. Except for the self-correlations and the correlation between Ldir and Ndir as well as a minor correlation between rLogLSPE32 and Ldir/Ndir, no unexpected correlation is observable.

Overtraining Check Plots:

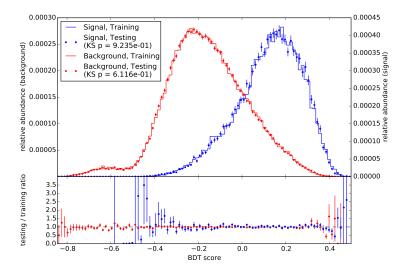


Figure D.12: Training sample overtraining check shown for the E^{-2} spectrum. As the respective KS p-values are rather large with 0.9 and 0.6, training sample overtraining can be excluded. The ratio of the signal and background testing sample to training sample, shown below, also does not exhibit unexpected behavior.

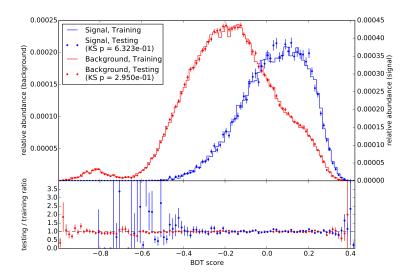


Figure D.13: Training sample overtraining check shown for the Γ 100 spectrum. As the respective KS p-values are rather large with 0.6 and 0.3, training sample overtraining can be excluded. The ratio of the signal and background testing sample to training sample, shown below, also does not exhibit unexpected behavior.

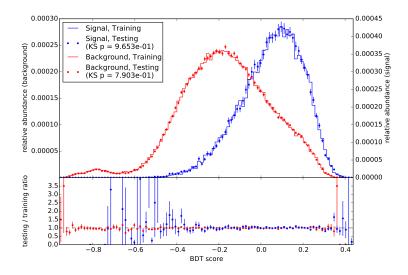


Figure D.14: Training sample overtraining check shown for the Γ 100npc spectrum. As the respective KS p-values are rather large with almost 1 and about 0.8, training sample overtraining can be excluded. The ratio of the signal and background testing sample to training sample, shown below, also does not exhibit unexpected behavior.

Efficiency Plots:

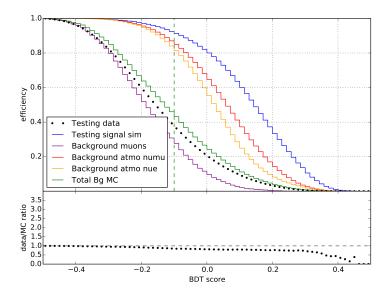


Figure D.15: BDT score cut efficiencies shown for the E^{-2} spectrum. The initially chosen BDT score cut value of -0.1 is shown by a vertical green dashed line.

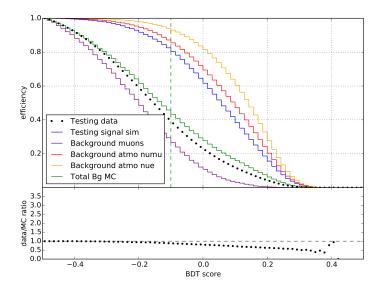


Figure D.16: BDT score cut efficiencies shown for the $\Gamma 100$ spectrum. The initially chosen BDT score cut value of -0.1 is shown by a vertical green dashed line.

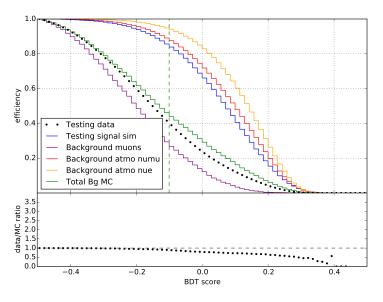


Figure D.17: BDT score cut efficiencies shown for the Γ 100npc spectrum. The initially chosen BDT score cut value of -0.1 is shown by a vertical green dashed line.

BDT Score Distributions:

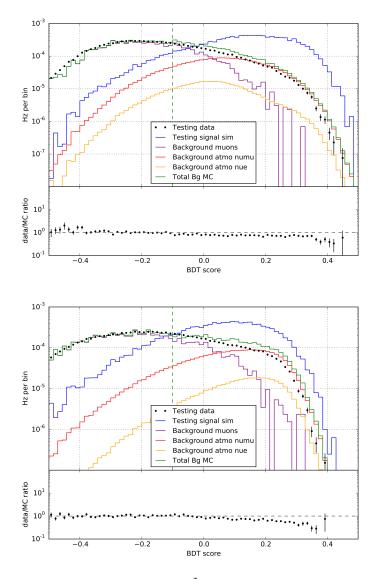


Figure D.18: BDT score distributions for the E^{-2} (top) and the Γ 100npc (bottom) spectrum. The initially chosen BDT score cut value of -0.1 is shown in vertical green dashed lines.

D.3 Event Selection Rates on Levels 3-6

This section presents the event selection rate summary tables for the E^{-2} , the Γ 100npc, the Γ 100 and the Γ 600single spectrum.

Level	sig. v _e [µHz]	sig. ν _µ [µHz]	sig. ν _τ [μHz]
L3	2081 ± 5	2977 ± 2	1735 ± 23
L4	1239 ± 5	1530 ± 2	923 ± 18
L5	616 ± 5	688 ± 2	455 ± 14
L6	568 ± 5	634 ± 2	420 ± 14
L6/L3	$(27.4 \pm 1.3)\%$	$(21.3 \pm 0.4)\%$	$(24.3 \pm 4.2)\%$

Table D.1: Event selection rates from level3 to level6 for the E^{-2} spectrum.

Table D.2: Event selection rates from level3 to level6 for the Γ 100npc spectrum.

Level	sig. v _e [µHz]	sig. ν _μ [μHz]	sig. ν _τ [μHz]
L3	2743 ± 4	3452 ± 9	1118 ± 4
L4	1509 ± 4	1690 ± 5	582 ± 1
L5	838 ± 4	925 ± 5	325 ± 1
L6	787 ± 4	847 ± 5	306 ± 1
L6/L3	$(28.6 \pm 0.5)\%$	$(24.6 \pm 0.3)\%$	$(27.4 \pm 0.5)\%$

Table D.3: Event selection rates from level3 to level6 for the Γ 100 spectrum.

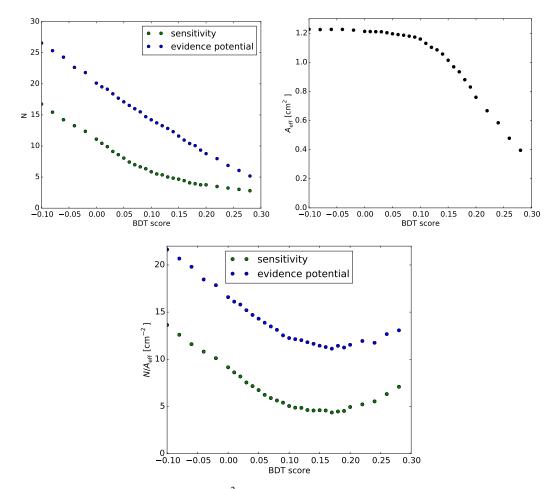
Level	sig. v _e [µHz]	sig. ν _µ [µHz]	sig. ν _τ [μHz]
L3	2759 ± 5	3467 ± 5	1094 ± 5
L4	1516 ± 2	1690 ± 2	571 ± 1
L5	849 ± 2	932 ± 2	320 ± 1
L6	785 ± 2	849 ± 2	301 ± 1
L6/L3	$(28.4 \pm 0.5)\%$	$(24.5 \pm 0.3)\%$	$(27.5 \pm 0.5)\%$

Level	sig. v _e [µHz]	sig. ν _µ [µHz]	sig. ν _τ [μHz]
L3	19608 ± 36	26763 ± 21	15140 ± 87
L4	11170 ± 27	13337 ± 15	7791 ± 62
L5	5865 ± 34	6301 ± 17	4101 ± 45
L6	5408 ± 33	5795 ± 17	3757 ± 43
L6/L3	$(27.6 \pm 1.0)\%$	$(21.6 \pm 0.4)\%$	$(24.8 \pm 0.2)\%$

Table D.4: Event selection rates from level3 to level6 for the Γ600single spectrum.

Likelihood Method - Additional Plots and Tables

This chapter holds additional plots and tables that illustrate the BDT and likelihood methods, starting with the BDT optimization plots.



E.1 BDT Optimization Plots

Figure E.1: Flux optimization for the E^{-2} stacked search. Given are both sensitivity and evidence potential (3σ potential) curves. The optimized score cut (at 0.17) was chosen to maximize the sensitivity on the number flux.

E

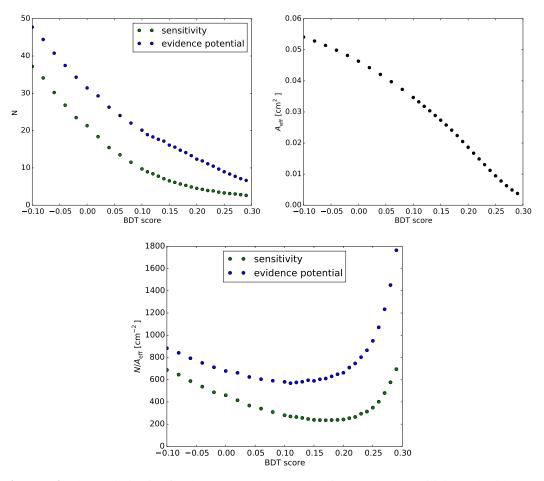


Figure E.2: Flux optimization for the Γ 100 stacked search. Given are both sensitivity and evidence potential (3σ potential) curves. The optimized score cut (at 0.17) was chosen to maximize the sensitivity on the number flux.

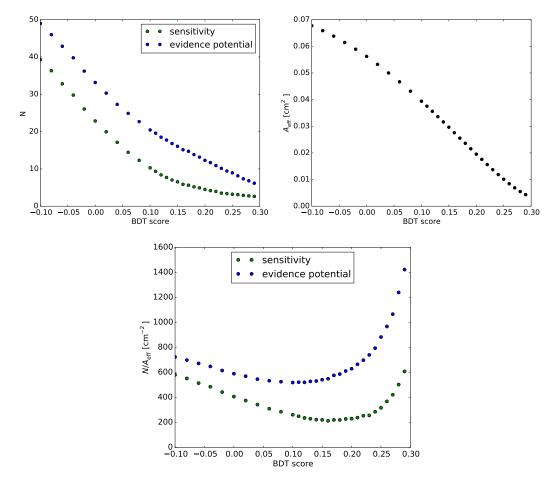


Figure E.3: Flux optimization for the Γ 100npc stacked search. Given are both sensitivity and evidence potential (3σ potential) curves. The optimized score cut (at 0.16) was chosen to maximize the sensitivity on the number flux.

LIST OF ALL ON-TIME EVENTS

The table below provides a summary of all on-time events found after unblinding. In no case, the total likelihood ratio r_{tot} exceeds 0.23; thus the likelihood of having a signal event is always smaller than that for background.

Table F.1: Table of all on-time events and the related GRBs. Shown are the IceCube run number, the GRB name, the identification number of the event as well as the GRB's T_{100} and various likelihood reconstruction parameters (see chapter 7.3). The latter includes the space angle deviation $\Delta\Omega$ between the GRB's and the event's directions as well as the time difference $\Delta t = t_{\text{GRB, start}} - t_{\text{event}}$.

Spectrum	Run	GRB	T ₁₀₀ [s]	$\Delta\Omega[^{\circ}]$	Δt [s]	E [GeV]	
		Event		r _{space}	r _{time}	r _{energy}	r _{tot}
E^{-2}	120182	120522B	28.16	127.85	-30.33	34.57	
		14679138		0.19	1.4	0.36	0.016
	120260	120605A	18.11	80.74	87.14	22.6	
		19358237		0.59	0.0018	0.28	4.6e-05
	120378	120624B	309.95	141.1	261.55	367.22	
		65075612		2.3e-09	1.4	2.1	1.1e-09
	120451	120716A	235.02	118.3	123.62	543.72	
		14978889		5.2e-10	1.5	2	2.5e-10
	120710	120923A	29.57	141.16	-87.49	147.37	
		53949651		0.23	0.032	1.3	0.0015
	120710	120923A	29.57	96.77	51.18	79.57	
		54319615		0.23	0.032	1.3	0.0015
	120726	120926A	4.29	71.17	-9.63	95.13	
		24066204		0.051	0.21	0.9	0.0014
	120914	121108A	138.13	42.3	-39.4	12.29	
		39065122		1.2	0.75	0.27	0.038

0.00011	176.07 1.5	61.22 0.0022	40.59 0.22	12.86	121125B 64989951	121063	
0.0018	238.23 1.9	-98.98 0.0076	83.66 0.82	142.85	130314A 28512304	122046	
0.0039	119.56 1.1	238.31 0.0025	19.52 9.2	129.42	130419A 17062686	122208	
0.00038	41.32 0.41	176.44 1.5	133.5 0.0041	274.55	130427A 39978326	122252	
0.017	34.57 0.63	-30.33 1.4	127.85 0.18	28.16	120522B 14679138	120182	600
4.9e-05	22.6 0.4	87.14 0.0018	80.74 0.64	18.11	120605A 19358237	120260	
3.2e-10	367.22 0.91	261.55 1.4	141.1 2.3e-09	309.95	120624B 65075612	120378	
0.12	79.57 1.3	51.18 2	96.77 0.44	29.57	120923A 54319615	120710	
0.0015	95.13 1.4	-9.63 0.21	71.17 0.049	4.29	120926A 24066204	120726	
0.024	12.29 0.23	-39.4 0.75	42.3 1.3	138.13	121108A 39065122	120914	
8e-05	176.07 1.6	61.22 0.0022	40.59 0.22	12.86	121125B 64989951	121063	
0.00087		-98.98 0.0076			130314A 28512304	122046	
0.23					130327A 22982658	122111	
1.5e-05		152.6 0.00088		32.87	120521C 2976127		100
0.019			127.85 0.16		120522B 14679138		

0.00014	22.6 1.2	87.14 0.0018	80.74 0.84	18.11	120605A 19358237	120260	
0.012			122.66 0.089	309.95	120624B 65185274	120378	
0.00017	10.61 0.99	-108.29 0.0035	94.45 0.63	47.8	120722A 14354114	120472	
0.12	7.11 0.96	-5.83 2.3	54.37 0.73	10.24	120914A 54245113	120668	
0.00019	95.13 0.3	-9.63 0.21	71.17 0.04	4.29	120926A 24066204	120726	
1.1e-10	13.51 1.1	-71.69 0.13	140.57 9.7e-09	59.13	121104A 9988796	120888	
0.074	12.29 1.1		42.3 1.2	138.13	121108A 39065122	120914	
0.14	14.1 1.1	62.52 1.6	66.73 0.99	33.8	121118A 10398811	120977	
0.0027		7.45 0.061	77.49 0.62	1.54	130219C 37066234	121912	
0.0085	43.89 0.91	36.17 2.2	156.43 0.056	63.49	130307B 18060685	122002	
0.0086	17.17 1.22	34.75 2.4	97.47 0.038	25.0	130407A 61984124	122151	
0.0011		106.13 0.013		25.0	130407A 62184401	122151	
0.00033	41.32 0.96		133.5 0.0031	274.55	130427A 39978326	122252	
1.4e-05		152.6 0.00088	95.33 0.2	32.87	120521C 2976127	120181	100npc
0.017		-30.33 1.4			120522B 14679138	120182	

0.01		303.54 1.4			120624B 65185274	120378	
0.0014					120905A 64531766	120635	
	7.11 1	-5.83 2.3	54.37 0.76	10.24	120914A 54245113	120668	
0.00028				4.29	120926A 24066204	120726	
0.061				138.13	121108A 39065122	120914	
0.13		62.52 1.6		33.8	121118A 10398811	120977	
5.9e-06			40.59 0.23	12.86	121125B 64989951	121063	
		-70.25 0.14		70.4	130106B 6595326	121545	
0.0027					130219C 37066234	121912	
		-112.38 0.0022			130305A 81456745	121996	
		36.17 2.2		63.49	130307B 18060685	122002	
	17.17 1.1	34.75 2.4	97.47 0.039	25.0	130407A 61984124	122151	
	14.46 1.1	106.13 0.013	21.93 0.99	25.0	130407A 62184401	122151	
	41.32 0.97	176.44 1.5	133.5 0.0032	274.55	130427A 39978326	122252	
0.0015	41.32 0.79	176.44 1.5	133.5 0.002	274.55	130427A 39978326	122252	600single

LIST OF FIGURES

2.1	Elementary particles and interactions in the Standard Model
2.2	Neutrino and antineutrino cross-sections
2.3	Ratio dependency on the CP parameter
2.4	Simulated rate parameter
2.5	Cosmic ray flux
2.6	Vertical flux/intensity at atmosphere and underground
2.7	Schematic of Cherenkov emission
3.1	Swift/Fermi GRB skymap 15
3.2	GRB standard paradigm vs. photospheric models
3.3	GRB observational parameters
3.4	Simulated GRB parameters for a collisionally heated jet
3.5	Neutrino flux spectra
3.6	Inelastic collision model expected event counts with IceCube
3.7	CCSNe probability densities
3.8	SNIa Neutrino luminosities
3.9	SNIa expected event counts in IceCube
3.10	Star evolution paths
3.11	· · · · · · · · · · · · · · · · · · ·
	Collapsar types
3.13	Lawrence-Livermore and Black Hole model
4.1	The IceCube detector
4.2	The DeepCore subdetector
4.3	The DOM and its main components
4.4	Schematic of the DOM's Mainboard
4.5	Schematic of the different data streams and daq systems
4.6	Trigger merging 40
4.7	Hit cleaning concepts
4.8	The DeepCore filter
4.9	SpiceLea absorption and effective scattering coefficients
	Track and Cascade event scheme
	High energy track and cascades event display 44
	Low-energy track and cascades event displays
	Dark noise rate behavior 46
	Expected PINGU supernova significance
4.15	Particle identification in PINGU

5.1	Comparison of noise simulation with detector data	51
5.2	Simulated detector responses to various SN models	52
5.3	Comparison of USSR and snsim	53
5.4	FiniteReco	56
6.1	SnDaq weekly downtime	62
6.2	SnDaq analysis windows	63
6.3	SN escalation scheme	66
6.4	Simulated significances as function of distance	67
6.5	Experimental and simulated significance distributions	68
6.6	Significance as function of SMT8 hit rate before and after muon subtraction .	68
6.7	SnDaq technical performance without and with muon subtraction	71
6.8	Gaussian tails of the significance distributions	72
6.9	Fraction of rejected events	74
6.10	Number of high-significance events	74
7.1	Analysis scheme	77
7.2	Gamma-Ray fluxes and durations	78
7.3	Experimental off-time data rates	80
7.3 7.4	Number of hit channels distribution on L3	84
7.4 7.5	Reconstructed zenith angle distribution on L3	85
7.5 7.6	Velocity ratio distribution on L4	85 86
7.7	Schematic of coincident events	86
7.8	Topological trigger distributions on L4	87
7.9	Hit veto parameter distributions on L4	87
7.10		88
	Definition of the veto region	90
	Monopod reconstructed cos(zenith) distributions on L5	91
	Monopod reconstructed cos(zemin) distributions on L5	92
	BDT correlation coefficients	92 93
	BDT overtraining checks	93 94
	BDT score distributions	95
	BDT efficiencies	95
	Event selection rates for level3 to level6	97
	Angular resolution	99
	Pull distribution	
		101
	Time PDFs	-
	Energy PDFs	
	Test statistic distribution	
	Angular dependency of the effective areas	
	Energy dependency of the effective area	
	Flux optimization for the Γ 600 stacked search	
	Flux optimization for the Γ 600 single source search \ldots	
	Test statistic distribution	
	Single source upper limit	
1.50		115

7.31	Stacked searches upper limits
D.1	Monopod reconstructed energy distribution on L5
D.2	Millipede reconstructed cosine(zenith) distribution on L5
D.3	Resca's z-coordinate distribution on L5
D.4	FiniteReco length distribution on L5
D.5	Ldir distribution on L5
D.6	Ndir distribution on L5 \ldots
D.7	rLogLSPE32 distribution on L5
D.8	nVetoHitsPulses distribution on L5
	BDT correlation coefficients for the E^{-2} spectrum
	BDT correlation coefficients for the $\Gamma 100$ spectrum $\ .$
D.11	BDT correlation coefficients for the Γ 100npc spectrum $\ldots \ldots \ldots \ldots 130$
	Overtraining check for the E^{-2} spectrum \ldots \ldots \ldots \ldots \ldots \ldots 131
D.13	Overtraining check for the $\Gamma 100$ spectrum $\hdots 100$
D.14	Overtraining check for the $\Gamma 100$ npc spectrum $\ldots \ldots \ldots$
	BDT score cut efficiency for the E^{-2} spectrum
D.16	BDT score cut efficiency for the $\Gamma 100$ spectrum $\ . \ . \ . \ . \ . \ . \ . \ . \ . \ $
	BDT score cut efficiency for the $\Gamma 100 npc$ spectrum $\hdots \hdots \h$
D.18	BDT score distributions
E.1	Flux activization for the Γ^{-2} stacked ecouple 127
2.1	Flux optimization for the E^{-2} stacked search
E.2	Flux optimization for the $\Gamma 100$ stacked search $\ldots \ldots \ldots$
E.3	Flux optimization for the $\Gamma 100 npc$ stacked search $\ldots \ldots \ldots \ldots \ldots \ldots 139$

LIST OF TABLES

3.1 3.2	Detection parameters of GRBWeb contributing missions $\dots \dots \dots \dots$ Burning stages of a $15M_{\odot}$ star $\dots \dots \dots$	22 27
4.1 4.2	Characteristics of the photomultiplier tube R7081-02 used in IceCube List of highQE DOMs in IceCube	36 36
6.1 6.2 6.3 6.4	SnDaq uptimeSnDaq Alert ActionsProcessing statistics on SPTSSignificance distribution parameters before and after muon subtraction	62 65 70 73
7.1 7.2 7.3 7.4 7.5 7.6 7.7 7.8 7.9 7.10 7.11 7.12		109 110 111 112
A.1	SnDaq Releases	
C.1	GRB catalog	123
D.1 D.2 D.3 D.4 F.1	Event selection rates from L3 to L6 for the E^{-2} spectrum	135 135 136
1.1		140

BIBLIOGRAPHY

- G. Aad, et al., Observation of a new particle in the search for the Standard Model Higgs boson with the ATLAS detector at the LHC, Physics Letters B 716, pp. 1–29 (2012).
- [2] S. Chatrchyan, et al., *Observation of a new boson at a mass of 125 GeV with the CMS experiment at the LHC*, Physics Letters B 716, pp. 30–61 (2012).
- [3] Particle content of the Standard Model, http://www.physik.uzh.ch/groups/serra/images/SM1.png, [Online; accessed July 27th 2016 14:22 CET.].
- [4] M. Agostini, et al., Results on Neutrinoless Double-β Decay of ⁷⁶Ge from Phase I of the GERDA Experiment, Phys. Rev. Lett. 111, p. 122503 (2013).
- [5] T. Griesel, *Optimierungen des Nachweises von Supernovae in IceCube*, Ph.D. thesis, Johannes Gutenberg-Universität Mainz (2010).
- [6] T. Feser, *Echtzeitsuche nach Neutrinoausbrüchen von Supernovae mit dem AMANDA-II-Detektor*, Ph.D. thesis, Johannes Gutenberg-Universität Mainz (2004).
- [7] C. Andreopoulos, et al., *The GENIE Neutrino Monte Carlo Generator*, Nucl. Instrum. Meth. A614, pp. 87–104 (2010).
- [8] The IceCube-PINGU Collaboration, *Letter of Intent: The Precision IceCube Next Generation Upgrade (PINGU)*, ArXiv e-prints:1401.2046 (2014).
- [9] A. Gazizov, et al., *Neutrino-nucleon cross sections at energies of Megaton-scale detectors*, EPJ Web of Conferences 116, p. 08003 (2016).
- [10] C. Giunti, Theory of neutrino oscillations, in Proceedings, 16th Conference on High Energy Physics (IFAE 2004), pp. 427–438 (2004).
- [11] T. K. Kuo, J. Pantaleone, *Neutrino oscillations in matter*, Rev. Mod. Phys. 61, pp. 937–979 (1989).
- [12] A. Ghosh, T. Thakore, S. Choubey, *Determining the Neutrino Mass Hierarchy with INO, T2K, NOvA and Reactor Experiments*, JHEP 04, p. 009 (2013).
- [13] D. S. Ayres, et al., NOvA: Proposal to Build a 30 Kiloton Off-Axis Detector to Study $v_{\mu} \rightarrow v_{e}$ Oscillations in the NuMI Beamline, ArXiv e-prints:hep-ex/0503053 (2004).
- [14] F. De Bernardis, et al., Determining the Neutrino Mass Hierarchy with Cosmology, Phys. Rev. D80, p. 123509 (2009).
- [15] A. Dueck, W. Rodejohann, K. Zuber, Neutrinoless Double Beta Decay, the Inverted Hierarchy and Precision Determination of theta(12), Phys. Rev. D83, p. 113010 (2011).

- [16] F. Capozzi, et al., Neutrino masses and mixings: Status of known and unknown 3 v parameters, Nuclear Physics B 908, pp. 218–234 (2016).
- [17] D. W. Scott. Multivariate Density Estimation and Visualization. in Handbook of Computational Statistics: Concepts and Methods, vol. 16. Humboldt-Universität Berlin, Center for Applied Statistics and Economics (CASE) (2004).
- [18] B. Silverman, Density Estimation for Statistics and Data Analysis, Chapman & Hall/CRC Monographs on Statistics & Applied Probability. Taylor & Francis (1986).
- [19] K. A. Olive, et al., Review of Particle Physics, Chin. Phys. C38, p. 090001 (2014).
- [20] P. B. Price, K. Woschnagg, Role of group and phase velocity in high-energy neutrino observatories, Astropart. Phys. 15, pp. 97–100 (2001).
- [21] Illustration of the Cherenkov effect, http://large.stanford.edu/courses/2014/ph241/alaeian2/images/f2big.png, [Online; accessed August 4th 2016 11:39 CET.].
- [22] R. W. Klebesadel, I. B. Strong, R. A. Olson, Observations of Gamma-Ray Bursts of Cosmic Origin, The Astrophysical Journal Letters 182, p. L85 (1973).
- [23] GRB Skymap, http://fermi.gsfc.nasa.gov/ssc/observations/types/grbs/grbs_140218_ gbm_lat_swift.jpg, [Online; accessed August 18th 2016 10:18 CET.].
- [24] E. Costa, et al., Discovery of an X-ray afterglow associated with the gamma-ray burst of 28 February 1997, Nature 387, pp. 783–785 (1997).
- [25] C. Kouveliotou, et al., *Identification of two classes of gamma-ray bursts*, The Astrophysical Journal Letters 413, pp. L101–L104 (1993).
- [26] S. E. Woosley, Gamma-ray bursts from stellar mass accretion disks around black holes, The Astrophysical Journal 405, pp. 273–277 (1993).
- [27] M. Muccino, et al., GRB 090227B: The Missing Link between the Genuine Short and Long Gamma-Ray Bursts, The Astrophysical Journal 763, p. 125 (2013).
- [28] A. I. MacFadyen, S. E. Woosley, Collapsars: Gamma-Ray Bursts and Explosions in "Failed Supernovae", The Astrophysical Journal 524, p. 262 (1999).
- [29] B. Giacomazzo, R. Perna, Formation of Stable Magnetars from Binary Neutron Star Mergers, Astrophys. J. 771, p. L26 (2013).
- [30] D. D. Ivanenko, D. F. Kurdgelaidze, *Hypothesis concerning quark stars*, Astrophysics 1, pp. 251–252 (1965).
- [31] R. Xu, E. Liang, X-ray flares of γ-ray bursts: Quakes of solid quark stars?, Science in China Series G: Physics, Mechanics and Astronomy 52, pp. 315–320 (2009).
- [32] P. Mészáros, et al., Gamma Ray Bursts in the HAWC Era, ArXiv e-prints:1506.02707 (2015).

- [33] R. Sari, *Beaming and jets in gamma-ray bursts*, AIP Conference Proceedings 526, pp. 504–513 (2000).
- [34] S. R. Kulkarni, et al., The afterglow, redshift and extreme energetics of the gamma-ray burst of 23 January 1999, Nature 398, pp. 389–394 (1999).
- [35] P. Mészáros, M. J. Rees, Optical and long wavelength afterglow from gamma-ray bursts, Astrophys. J. 476, pp. 232–237 (1997).
- [36] K. Ioka, Very High Lorentz Factor Fireballs and Gamma-Ray Burst Spectra, Prog. Theor. Phys. 124, pp. 667–710 (2010).
- [37] A. M. Beloborodov, *Regulation of the Spectral Peak in Gamma-Ray Bursts*, The Astrophysical Journal 764, p. 157 (2013).
- [38] D. Band, et al., BATSE observations of gamma-ray burst spectra. I Spectral diversity, The Astrophysical Journal 413, pp. 281–292 (1993).
- [39] L. Nava, et al., Spectral properties of 438 GRBs detected by Fermi/GBM, A&A 530, p. A21 (2011).
- [40] A. M. Beloborodov, Collisional mechanism for gamma-ray burst emission, Monthly Notices of the Royal Astronomical Society 407, pp. 1033–1047 (2010).
- [41] R. D. Preece, et al., The BATSE Gamma-Ray Burst Spectral Catalog. I. High Time Resolution Spectroscopy of Bright Bursts Using High Energy Resolution Data, The Astrophysical Journal Supplement Series 126, p. 19 (2000).
- [42] R. E. Hellauer III, An all-sky, three-flavor search for neutrinos from gamma-ray bursts with the IceCube neutrino observatory, Ph.D. thesis, University of Maryland Center for Experimental Fundamental Physics (2015).
- [43] I. Bartos, et al., Detection Prospects for GeV Neutrinos from Collisionally Heated Gamma-ray Bursts with IceCube/DeepCore, Phys. Rev. Lett. 110 (2013).
- [44] K. Murase, K. Kashiyama, P. Mészáros, Subphotospheric Neutrinos from Gamma-Ray Bursts: The Role of Neutrons, Phys. Rev. Lett. 111, p. 131102 (2013).
- [45] K. Kashiyama, K. Murase, P. Mészáros, Neutron-Proton-Converter Acceleration Mechanism at Subphotospheres of Relativistic Outflows, Phys. Rev. Lett. 111 (2013).
- [46] E. V. Derishev, et al., *Particle acceleration through multiple conversions from a charged into a neutral state and back*, Phys. Rev. D 68, p. 043003 (2003).
- [47] A. Achterberg, et al., Particle acceleration by ultrarelativistic shocks: Theory and simulations, Mon. Not. Roy. Astron. Soc. 328, p. 393 (2001).
- [48] P. L. Nolan, et al., *Fermi Large Area Telescope Second Source Catalog*, The Astrophysical Journal Supplement Series 199, p. 31 (2012).
- [49] H. A. Krimm, et al., *The Swift/BAT Hard X-ray Transient Monitor*, Astrophys. J. Suppl. 209, p. 14 (2013).

- [50] D. N. Burrows, et al., The Swift X-ray Telescope, Space Sci. Rev. 120, p. 165 (2005).
- [51] R. Aptekar, et al., Cosmic gamma-ray bursts studies with Ioffe Institute Konus experiments, in -Ray Bursts 2012 Conference (GRB 2012), p. 118 (2012).
- [52] M. Matsuoka, et al., *The MAXI Mission on the ISS: Science and Instruments for Monitoring All-Sky X-Ray Images*, Publications of the Astronomical Society of Japan 61, pp. 999–1010 (2009).
- [53] K. Yamaoka, et al., Design and In-Orbit Performance of the Suzaku Wide-Band All-Sky Monitor, Publications of the Astronomical Society of Japan 61, pp. S35–S53 (2009).
- [54] M. Feroci, et al., SuperAGILE: The hard X-ray imager for the AGILE space mission, Nuclear Instruments and Methods in Physics Research Section A: Accelerators, Spectrometers, Detectors and Associated Equipment 581, pp. 728–754 (2007).
- [55] C. Winkler, et al., The INTEGRAL mission, A&A 411, pp. L1-L6 (2003).
- [56] S. C. Solomon, et al., The MESSENGER mission to Mercury: scientific objectives and implementation, Planetary and Space Science 49, pp. 1445–1465 (2001).
- [57] K. Hurley, et al., *Mars odyssey joins the third interplanetary network*, Astrophys. J. Suppl. 164, p. 124 (2006).
- [58] K. Hurley, et al., The Interplanetary Network Supplement to the Fermi GBM Catalog of Cosmic Gamma-Ray Bursts, Astrophys. J. Suppl. 207, p. 39 (2013).
- [59] K. Hurley, et al., *The Third Interplanetary Network*, AIP Conference Proceedings 1358, pp. 385–388 (2011).
- [60] M. Richman, A search for muon neutrinos coincident with northern gamma-ray bursts using IceCube, Ph.D. thesis, University of Maryland College Park (2015).
- [61] A. Mirizzi, et al., Supernova Neutrinos: Production, Oscillations and Detection, Riv. Nuovo Cim. 39, p. 1 (2016).
- [62] G. Mills, et al., *The Proceedings of the 22nd International Conference on Neutrino Physics and Astrophysics Supernova neutrino observations: What can we learn?*, Nuclear Physics B Proceedings Supplements 221, pp. 218–229 (2011).
- [63] M. Ahlers, P. Mertsch, S. Sarkar, Cosmic ray acceleration in supernova remnants and the FERMI/PAMELA data, Phys. Rev. D 80, p. 123017 (2009).
- [64] D. Maoz, C. Badenes, *The supernova rate and delay time distribution in the Magellanic Clouds*, Mon. Not. R. Astron. Soc. 407, pp. 1314–1327 (2010).
- [65] B. Wang, Z. Han, Progenitors of type Ia supernovae, New Astronomy Reviews 56, pp. 122–141 (2012).
- [66] W. P. Wright, et al., Neutrinos from type Ia supernovae: The deflagration-to-detonation transition scenario, Phys. Rev. D94, p. 025026 (2016).

- [67] H.-T. Janka, Explosion Mechanisms of Core-Collapse Supernovae, Ann. Rev. Nucl. Part. Sci. 62, pp. 407–451 (2012).
- [68] M. S. Longair, High energy astrophysics. Cambridge Univ. Press, 3rd edn. (2011).
- [69] S. Woosley, T. Janka, *The physics of core-collapse supernovae*, Nat Phys 1, pp. 147–154 (2005).
- [70] D. Arnett, Stellar Nucleosynthesis: A Status Report 2003, vol. 4: Origin and Evolution of the Elements of Carnegie Observatories Astrophysics Series. Cambridge: Cambridge Univ. Press (2004).
- [71] H. A. Bethe, J. R. Wilson, *Revival of a stalled supernova shock by neutrino heating*, The Astrophysical Journal 295, pp. 14–23 (1985).
- [72] S. Stoica, V. P. Paun, A. G. Negoita, Nuclear effects on neutrino emissivities from nucleon-nucleon bremsstrahlung, Physical Review C 69, p. 068801 (2004).
- [73] A. Heger, et al., *How massive single stars end their life*, Astrophys. J. 591, pp. 288–300 (2003).
- [74] L. Hüdepohl, et al., Neutrino Signal of Electron-Capture Supernovae from Core Collapse to Cooling, Physical Review Letters 104, p. 251101 (2010).
- [75] P. Mészáros, Gamma-Ray Bursts, Rept. Prog. Phys. 69, pp. 2259–2322 (2006).
- [76] K. Z. Stanek, et al., Spectroscopic Discovery of the Supernova 2003dh Associated with GRB 030329, The Astrophysical Journal 591, pp. L17–L20 (2003).
- [77] M. Asplund, et al., *The Chemical Composition of the Sun*, Annual Review of Astronomy and Astrophysics 47, pp. 481–522 (2009).
- [78] K. Kotake, K. Sato, K. Takahashi, *Explosion mechanism, neutrino burst, and gravitational wave in core-collapse supernovae*, Rept. Prog. Phys. 69, pp. 971–1144 (2006).
- [79] T. Totani, et al., Future detection of supernova neutrino burst and explosion mechanism, Astrophys. J. 496, pp. 216–225 (1998).
- [80] K. Sumiyoshi, S. Yamada, H. Suzuki, Dynamics and Neutrino Signal of Black Hole Formation in Nonrotating Failed Supernovae. I. Equation of State Dependence, The Astrophysical Journal 667, p. 382 (2007).
- [81] The IceCube Media Gallery, https://gallery.icecube.wisc.edu.
- [82] T. DeYoung, Particle physics in ice with IceCube DeepCore, Nuclear Instruments and Methods in Physics Research Section A: Accelerators, Spectrometers, Detectors and Associated Equipment 692, pp. 180–183 (2012), 3rd Roma International Conference on Astroparticle Physics.

- [83] R. Abbasi, et al., *IceTop: The surface component of IceCube*, Nuclear Instruments and Methods in Physics Research Section A: Accelerators, Spectrometers, Detectors and Associated Equipment 700, pp. 188–220 (2013).
- [84] R. Abbasi, et al., *The design and performance of IceCube DeepCore*, Astroparticle Physics 35, pp. 615–624 (2012).
- [85] M. G. Aartsen, et al., *The IceCube Neutrino Observatory: Instrumentation and Online Systems*, JINST 12, p. P03012 (2017).
- [86] R. Abbasi, et al., *IceCube sensitivity for low-energy neutrinos from nearby supernovae*, A&A 535, p. A109 (2011).
- [87] R. Abbasi, et al., Calibration and Characterization of the IceCube Photomultiplier Tube, Nuclear Instruments and Methods in Physics Research Section A: Accelerators, Spectrometers, Detectors and Associated Equipment 618, pp. 139–152 (2010).
- [88] R. Abbasi, et al., The IceCube Data Acquisition System: Signal Capture, Digitization, and Timestamping, Nucl. Instrum. Meth. A601, pp. 294–316 (2009).
- [89] J. L. Kelley for the IceCube Collaboration, Event triggering in the IceCube data acquisition system, AIP Conference Proceedings 1630, pp. 154–157 (2014).
- [90] D. Heereman von Zuydtwyck, *HitSpooling: an improvement for the supernova neutrino detection system in icecube*, Ph.D. thesis, Université libre de Bruxelles (2015).
- [91] J. Kelley, private communication (2016).
- [92] M. Larson, Simulation and identification of non-Poissonian noise triggers in the *IceCube neutrino detector*, Master's thesis, University of Alabama (2013).
- [93] H. Taavola, D. J. Koskinen, D. Grant, A Revision of the DeepCore Filter to match the Extended Fiducial Volume of DeepCore, https://docushare.icecube.wisc.edu/dsweb/G et/Document-56543/DeepCore%20Filter%20revision%20propposal%202011.pdf (2011), High resolution version from https://docushare.icecube.wisc.edu/dsweb/Get/Version-87731/koskinen_ icecube-deepcore_INF011.pdf.
- [94] J. D. Daughhetee, DeepCore 2012 Filter Proposal, https: //docushare.icecube.wisc.edu/dsweb/Get/Document-59397/DeepCoreFilterProposal.pdf.
- [95] M. G. Aartsen, et al., Measurement of South Pole ice transparency with the IceCube LED calibration system, Nucl. Instrum. Meth. A711, pp. 73–89 (2013).
- [96] D. Chirkin, Evidence of optical anisotropy of the South Pole ice, in Proceedings, 33rd International Cosmic Ray Conference (ICRC2013): Rio de Janeiro, Brazil, July 2-9, 2013, p. 0580 (2013).
- [97] M. G. Aartsen, et al., Search for Astrophysical Tau Neutrinos in Three Years of IceCube Data, Phys. Rev. D93, p. 022001 (2016).

- [98] K. Schatto, *Stacked searches for high-energy neutrinos from blazars with IceCube*, Ph.D. thesis, Johannes Gutenberg-Universität Mainz (2014).
- [99] K. Wiebe, All-flavor based Searches for solar Dark Matter with the IceCube Neutrino Observatory, Ph.D. thesis, Johannes Gutenberg-Universität Mainz (2016).
- [100] J. Ahrens, et al., Muon track reconstruction and data selection techniques in AMANDA, Nucl. Instrum. Meth. A524, pp. 169–194 (2004).
- [101] M. G. Aartsen, et al., Energy Reconstruction Methods in the IceCube Neutrino Telescope, JINST 9, p. P03009 (2014).
- [102] M. G. Aartsen, et al., Observation of High-Energy Astrophysical Neutrinos in Three Years of IceCube Data, Phys. Rev. Lett. 113, p. 101101 (2014).
- [103] V. Baum for the IceCube Collaboration, *The IceCube data acquisition system for galactic core collapse supernova searches*, AIP Conference Proceedings 1630, pp. 150–153 (2014).
- [104] B. Eberhardt, *Supernovae with IceCube: Determination of their Origin and Average Neutrino Energy*, Ph.D. thesis, Johannes Gutenberg-Universität Mainz (tba).
- [105] E. Lohfink, *PMT noise and supernova direction determination in IceCube*, Bachelor's thesis, Johannes Gutenberg-Universität Mainz (2014).
- [106] H. O. Meyer, Spontaneous electron emission from a cold surface, EPL (Europhysics Letters) 89, p. 58001 (2010).
- [107] M. G. Aartsen, et al., PINGU: A Vision for Neutrino and Particle Physics at the South Pole, J. Phys. G44, p. 054006 (2017), preliminary full version https: //docushare.wipac.wisc.edu/dsweb/Get/Document-77784/PINGU_LOIv2_21June2016.pdf, tbp shortly.
- [108] D. Heck, et al., CORSIKA: a Monte Carlo code to simulate extensive air showers. Forschungszentrum Karlsruhe GmbH (1998).
- [109] T. K. Gaisser, Spectrum of cosmic-ray nucleons, kaon production, and the atmospheric muon charge ratio, Astropart. Phys. 35, pp. 801–806 (2012).
- [110] M. Honda, et al., *Calculation of atmospheric neutrino flux using the interaction model calibrated with atmospheric muon data*, Phys. Rev. D75, p. 043006 (2007).
- [111] S. Agostinelli, et al., *Geant4 a simulation toolkit*, Nuclear Instruments and Methods in Physics Research Section A: Accelerators, Spectrometers, Detectors and Associated Equipment 506, pp. 250–303 (2003).
- [112] E. O'Connor, C. D. Ott, *The Progenitor Dependence of the Pre-explosion Neutrino Emission in Core-collapse Supernovae*, The Astrophysical Journal 762, p. 126 (2013).

- [113] C. D. Ott, et al., Correlated Gravitational Wave and Neutrino Signals from General-Relativistic Rapidly Rotating Iron Core Collapse, Phys. Rev. D86, p. 024026 (2012).
- [114] N. Manger, *Analyse schnell variierender Supernovasignale in IceCube*, Bachelor's thesis, Johannes Gutenberg-Universität Mainz (2012).
- [115] V. Baum, Verbesserung der Supernova-Detektion mit dem IceCube-Neutrinoteleskop, Diploma thesis, Johannes Gutenberg-Universität Mainz (2011).
- [116] B. Riedel, *Modeling and Understanding Supernova Signals in the IceCube Neutrino Observatory*, Ph.D. thesis, University of Wisconsin-Madison (2014).
- [117] L. Köpke, private communication (2016).
- [118] M. G. Aartsen, et al., Improvement in fast particle track reconstruction with robust statistics, Nuclear Instruments and Methods in Physics Research A 736, pp. 143–149 (2014).
- [119] D. Pandel, Bestimmung von Wasser- und Detektorparametern und Rekonstruktion von Myonen bis 100 TeV mit dem Baikal-Neutrinoteleskop NT-72, Diploma thesis, Humboldt-Universität Berlin (1996).
- [120] D. Chirkin, Photon tracking with GPUs in IceCube, Nucl. Instrum. Meth. A725, pp. 141–143 (2013).
- [121] N. Whitehorn, J. van Santen, S. Lafebre, *Penalized Splines for Smooth Representation of High-dimensional Monte Carlo Datasets*, Comput. Phys. Commun. 184, pp. 2214–2220 (2013).
- [122] S. Euler, Observations of oscillations of atmospheric neutrinos with the IceCube Neutrino Observatory, Ph.D. thesis, Rheinisch-Westfälische Technische Hochschule (RWTH) Aachen (2013).
- [123] J. Casey, *Search for high energy GRB neutrinos in IceCube*, Ph.D. thesis, Georgia Institute of Technology (2015).
- [124] J. Lünemann, Suche nach Dunkler Materie in Galaxien und Galaxienhaufen mit dem Neutrinoteleskop IceCube, Ph.D. thesis, Johannes Gutenberg-Universität Mainz (2013).
- [125] H. Cramér, A contribution to the theory of statistical estimation, Scandinavian Actuarial Journal 1946, pp. 85–94 (1946).
- [126] C. R. Rao, Information and accuracy attainable in the estimation of statistical parameters, Bull Calcutta. Math. Soc. 37, pp. 81–91 (1945).
- [127] R. A. Fisher, *The Logic of Inductive Inference*, Journal of the Royal Statistical Society 98, pp. 39–82 (1935).
- [128] G. Kroll, tba, Ph.D. thesis, Johannes Gutenberg-Universität Mainz (tba).

- [129] M. Smith, et al., *The Astrophysical Multimessenger Observatory Network (AMON)*, Astroparticle Physics 45, pp. 56–70 (2013).
- [130] L. Köpke, private communication (2017).
- [131] A. Fritz, Supernova-Signaturen im IceCube-Neutrino- und aLIGO-Gravitationswellendetektor, Master's thesis, Johannes Gutenberg-Universität Mainz (2017).
- [132] A. Mirizzi, G. G. Raffelt, P. D. Serpico, *Earth matter effects in supernova neutrinos:* Optimal detector locations, JCAP 0605, p. 012 (2006).
- [133] G. Kroll, B. Riedel, V. Baum, On the detection of galactic core collapse supernovae with IceCube, in Proceedings, 33rd International Cosmic Ray Conference (ICRC2013): Rio de Janeiro, Brazil, July 2-9, 2013, p. 0446 (2013).
- [134] P. Antonioli, et al., SNEWS: the SuperNova Early Warning System, New Journal of Physics 6, p. 114 (2004).
- [135] A. Fritz, *Optimierung der Empfindlichkeit des Supernova-Frühwarnsystems*, Bachelor's thesis, Johannes Gutenberg-Universität Mainz (2015).
- [136] V. Baum, et al., *Recent improvements in the detection of supernovae with the IceCube observatory*, PoS ICRC2015, p. 1096 (2016).
- [137] C. Rott, Good Run List, IceCube internal report icecube/201109002 (2011).
- [138] SnDaq technical monitoring pages, https://live.icecube.wisc.edu/details/sndaq/.
- [139] E. Jones, et al., SciPy: Open source scientific tools for Python (2001).
- [140] G. J. Feldman, R. D. Cousins, A Unified approach to the classical statistical analysis of small signals, Phys. Rev. D57, pp. 3873–3889 (1998).
- [141] T. Kowarik, Supernova Neutrinos in AMANDA and IceCube Monte Carlo Development and Data Analysis, Ph.D. thesis, Johannes Gutenberg-Universität Mainz (2010).
- [142] A. Piégsa, Supernova-Detektion mit dem IceCube-Neutrinoteleskop, Ph.D. thesis, Johannes Gutenberg-Universität Mainz (2009).
- [143] H. Shen, et al., Relativistic equation of state of nuclear matter for supernova and neutron star, Nucl. Phys. A637, pp. 435–450 (1998).
- [144] J. M. Lattimer, F. D. Swesty, A generalized equation of state for hot, dense matter, Nuclear Physics A 535, pp. 331–376 (1991).
- [145] Demorest P. B., et al., *A two-solar-mass neutron star measured using Shapiro delay*, Nature 467, pp. 1081–1083 (2010).
- [146] M. Hempel, J. Schaffner-Bielich, *A statistical model for a complete supernova equation of state*, Nuclear Physics A 837, pp. 210–254 (2010).

- [147] M. H. van Kerkwijk, R. P. Breton, S. R. Kulkarni, Evidence for a Massive Neutron Star from a Radial-velocity Study of the Companion to the Black-widow Pulsar PSR B1957+20, The Astrophysical Journal 728, p. 95 (2011).
- [148] J. Antoniadis, et al., A Massive Pulsar in a Compact Relativistic Binary, Science 340 (2013).
- [149] D. Xu, et al., *Discovery of the broad-lined Type Ic SN 2013cq associated with the very energetic GRB 130427A*, Astrophys. J. 776, p. 98 (2013).
- [150] M. Ackermann, et al., Fermi-LAT Observations of the Gamma-Ray Burst GRB 130427A, Science 343, pp. 42–47 (2014).
- [151] A. Maselli, et al., GRB 130427A: A Nearby Ordinary Monster, Science 343, pp. 48–51 (2014).
- [152] J. M. Carpenter, et al., Recent Results from CARMA, in Submillimeter Astrophysics and Technology: A Symposium Honoring Thomas G. Phillips, vol. 417 of ASP Conference Series (2009).
- [153] R. Preece, et al., *The First Pulse of the Extremely Bright GRB 130427A: A Test Lab* for Synchrotron Shocks, Science (2013).
- [154] W. T. Vestrand, et al., The Bright Optical Flash and Afterglow from the Gamma-Ray Burst GRB 130427A, Science 343, pp. 38–41 (2014).
- [155] M. G. Bernardini, et al., A magnetar powering the ordinary monster GRB 130427A?, Mon. Not. Roy. Astron. Soc. 439, p. 80 (2014).
- [156] M. Wallraff, C. Wiebusch, Calculation of oscillation probabilities of atmospheric neutrinos using nuCraft, Computer Physics Communications 197, pp. 185–189 (2015).
- [157] A. M. Dziewonski, D. L. Anderson, *Preliminary reference Earth model*, Physics of the Earth and Planetary Interiors 25, pp. 297–356 (1981).
- [158] J. D. Daughhetee, Search for neutrino transients using IceCube and DeepCore, Ph.D. thesis, Georgia Institute of Technology (2015).
- [159] K. M. Górski, et al., HEALPix: A Framework for High-Resolution Discretization and Fast Analysis of Data Distributed on the Sphere, The Astrophysical Journal 622, pp. 759–771 (2005).
- [160] D. Chirkin, *Neutrino search with IceCube*, IceCube internal report icecube/200807006 (2008).
- [161] R. Mike, IceCube internal PyBDT documentation, http://software.icecube.wisc.edu/documentation/projects/pybdt/index.html.
- [162] A. Hocker, et al., TMVA Toolkit for Multivariate Data Analysis, PoS ACAT, p. 040 (2007).

- [163] Y. Freund, R. E. Schapire, A Decision-Theoretic Generalization of On-Line Learning and an Application to Boosting, Journal of Computer and System Sciences 55, pp. 119–139 (1997).
- [164] S. Odrowski, *High-Energy Neutrino Scan of the Galactic Plane*, Ph.D. thesis, Ruperto-Carola-University of Heidelberg (2012).
- [165] IceCube internal documentation for rLogL and pLogL, https://wiki.icecube.wisc.edu/index.php/Plogl.
- [166] A. Goldstein, et al., The Fermi GBM Gamma-Ray Burst Spectral Catalog: The First Two Years, Astrophysical Journal Supplements 199, p. 19 (2012).
- [167] M. C. R. Zoll, A search for solar dark matter with the IceCube neutrino detector: Advances in data treatment and analysis technique, Ph.D. thesis, Stockholm University, Department of Physics (2016).
- [168] M. G. Aartsen, et al., *Extending the search for muon neutrinos coincident with gamma-ray bursts in IceCube data*, ArXiv e-prints:1702.06868 (2017).
- [169] K. Murase, private communication (2016).
- [170] J. D. Scargle, et al., Studies in Astronomical Time Series Analysis. VI. Bayesian Block Representations, The Astrophysical Journal 764, p. 167 (2013).